Neurobiology of Disease

Nacc1 Mutation in Mice Models Rare Neurodevelopmental Disorder with Underlying Synaptic Dysfunction

Mark A. Deehan,[1] Josine M. Kothuis,[1] Ellen Sapp,[1] Kathryn Chase,[2] Yuting Ke,[1,3] Connor Seeley,[1] Maria Iuliano,[1] Emily Kim,[1] Lori Kennington,[2] Rachael Miller,[2] Adel Boudi,[1] Kai Shing,[1] Xueyi Li,[1] Edith Pfister,[2,4] Christelle Anaclet,[5] Michael Brodsky,[6] Kimberly Kegel-Gleason,[1] Neil Aronin,[2] and Marian DiFiglia[1]

[1]Department of Neurology, Massachusetts General Hospital, Charlestown, Massachusetts 02129, [2]Department of Medicine, UMass Chan Medical School, Worcester, Massachusetts 01655, [3]Department of Biological Engineering, Massachusetts Institute of Technology, Cambridge, Massachusetts 02139, [4]Program in Bioinformatics and Integrative Biology, UMass Chan Medical School, Worcester, Massachusetts 01655, [5]Department of Neurological Surgery, University of California Davis School of Medicine, Davis, California 95817, and [6]Department of Molecular, Cell and Cancer Biology, UMass Chan Medical School, Worcester, Massachusetts 01655

A missense mutation in the transcription repressor Nucleus accumbens-associated 1 (*NACC1*) gene at c.892C>T (p.Arg298Trp) on chromosome 19 causes severe neurodevelopmental delay (Schoch et al., 2017). To model this disorder, we engineered the first mouse model with the homologous mutation (*Nacc1*$^{+/R284W}$) and examined mice from E17.5 to 8 months. Both genders had delayed weight gain, epileptiform discharges and altered power spectral distribution in cortical electroencephalogram, behavioral seizures, and marked hindlimb clasping; females displayed thigmotaxis in an open field. In the cortex, NACC1 long isoform, which harbors the mutation, increased from 3 to 6 months, whereas the short isoform, which is not present in humans and lacks aaR284 in mice, rose steadily from postnatal day (P) 7. Nuclear NACC1 immunoreactivity increased in cortical pyramidal neurons and parvalbumin containing interneurons but not in nuclei of astrocytes or oligodendroglia. Glial fibrillary acidic protein staining in astrocytic processes was diminished. RNA-seq of P14 mutant mice cortex revealed over 1,000 differentially expressed genes (DEGs). Glial transcripts were downregulated and synaptic genes upregulated. Top gene ontology terms from upregulated DEGs relate to postsynapse and ion channel function, while downregulated DEGs enriched for terms relating to metabolic function, mitochondria, and ribosomes. Levels of synaptic proteins were changed, but number and length of synaptic contacts were unaltered at 3 months. Homozygosity worsened some phenotypes including postnatal survival, weight gain delay, and increase in nuclear NACC1. This mouse model simulates a rare form of autism and will be indispensable for assessing pathophysiology and targets for therapeutic intervention.

Key words: autism; EEG; NACC1; seizure; synapse; transcriptomics

Significance Statement

A missense mutation causing an arginine to tryptophan (R>W) mutation at amino acid 298 in the nucleus accumbens-associated protein 1 (NACC1) causes profound neurodevelopmental arrest in humans. NACC1 is a transcription repressor but how the R298W mutation causes disease in the brain is unclear. We engineered the first mouse model with this mutation and found delayed weight gain, open field deficits signaling anxiety, motor dysfunction, and cortical EEG disturbance akin to absence seizures. Females displayed more deficits than males. NACC1 protein increased in neurons in multiple brain regions including cortex and RNA sequencing and protein studies in postnatal mice revealed dysregulated synaptic pathways. This mouse model recapitulates patient symptoms and provides robust cellular and molecular benchmarks for therapeutic testing.

Received Aug. 24, 2023; revised Jan. 5, 2024; accepted Feb. 3, 2024.

Author contributions: M.A.D., X.L., E.P., C.A., M.B., K.K.-G., N.A., and M.D. designed research; M.A.D., J.M.K., E.S., K.C., Y.K., C.S., M.I., E.K., L.K., R.M., A.B., K.S., E.P., and C.A. performed research; M.A.D., J.K., E.S., K.C., Y.K., C.S., M.I., E.K., L.K., R.M., A.B., K.S., E.P., C.A., M.B., K.K.-G., and M.D. analyzed data; M.A.D. and M.D. wrote the paper.

We are very grateful to the members of the NACC1 family group for their advice and encouragement throughout the course of this investigation. This work was supported by donations to the MGB NACC1 Research Fund to M.D. and the Higgins Family of Worchester Fund at UMass Chan to N.A.

K.K.-G. spouse owns <0.1% stock in the following companies: Advanced Microdevices, Aveo Pharmaceuticals, Boston Scientific, Bristol-Myers Squibb, Cisco Systems, Fate Therapeutics, GE Healthcare Life Sciences, Generex Biotechnology, Idera Pharmaceuticals, Nante Health, Neurometrics, NuGenerex, Repligen, Sesen Bio, T2 Biosystems, and Vericel. The other authors declare no competing financial interests.

Correspondence should be addressed to Marian DiFiglia at difiglia@helix.mgh.harvard.edu.

https://doi.org/10.1523/JNEUROSCI.1610-23.2024

Introduction

Advances in whole genome and whole exome sequencing (WES) have rapidly advanced knowledge of the causative mutations for ultrarare human neurodevelopmental disorders (Rexach et al., 2019). Recently, WES identified a de novo heterozygous mutation in the nucleus accumbens-associated 1 (*NACC1*) gene at c.892C>T on chromosome 19 causing a change from arginine to tryptophan (p.Arg298Trp herein referred to as R298W). This mutation was first identified in seven young individuals with profound developmental delay, failure to thrive, epilepsy, bilateral cataracts, delayed brain myelination, involuntary movements, no speech, and gastrointestinal (GI) distress (Schoch et al., 2017). There has been a case report describing another patient with the mutation (Lyu et al., 2021) and a survey documenting episodes of extreme irritability that patients suffer (Schoch et al., 2023). Two of the original seven reported and four of 33 affected individuals identified since then have died (communication from the NACC1 family group). This disorder has the highest-ranking score of 1 for an autism spectrum disorder in the SFARI gene database.

Nacc1 was first described as an mRNA that increased in the nucleus accumbens (NAc) in response to a chronic cocaine treatment and thus was given the name nucleus accumbens-associated gene 1 (*Nacc1* or *Nac1*, aliases include BEND8, BTBD14B, BTBD30, and NECFM; Cha et al., 1997; Kalivas et al., 1999; Mackler et al., 2000). Mouse *Nacc1* mRNA expression is most abundant in the brain, liver, and kidney (Mackler et al., 2003). NACC1 is a member of the BTB/POZ family of transcription factors, contains a DNA-binding BEN domain (Nakayama et al., 2020; Zheng et al., 2022), interacts with the RNA-binding protein TDP-43 (Scofield et al., 2012), transcriptionally regulates proteasome mediated degradation, and functions in stem cell pluripotency, cancer, and synaptic plasticity (Korutla et al., 2005, 2009; Shen et al., 2007; Yap et al., 2012; Ruan et al., 2017). In neuronal cells, transcriptional repression via NACC1 can be mediated by recruitment of histone deacetylases (Korutla et al., 2005). NACC1 has been implicated in synaptic plasticity by translocating the proteasome to dendritic spines (Shen et al., 2007), and in vitro studies in mouse hippocampal neurons suggest that the mutation alters glutamatergic transmission in hippocampal neurons (Daniel et al., 2023). Identified roles for NACC1 as a transcription factor affecting genes involved in stem cell renewal, neuronal and glial differentiation, and synaptic function could account for the early impact of the mutation on human development. However, how the profound deficits caused by the R298W mutation in humans affect the brain to cause dysfunction is unknown.

A mouse model of this disorder would facilitate the study of disease pathogenesis and discovery of therapeutic approaches. Here we report findings in mice engineered with the corresponding mutation *Nacc1*$^{+/R284W}$. Compared with wild-type mice (*Nacc1*$^{+/+}$), *Nacc1*$^{+/R284W}$ mice gain less weight, display abnormal cortical electroencephalogram (EEG) activity akin to absence seizures in humans, have behavioral seizures, develop hindlimb clasping and other motor and behavioral dysfunctions, and have elevated levels of NACC1 protein evident by Western blot and immunofluorescence labeling in neuronal nuclei in the cortex, nucleus accumbens, caudate–putamen, hippocampus, and other brain regions. Genes that were differentially expressed in *Nacc1*$^{+/R284W}$ mice compared with those in *Nacc1*$^{+/+}$ mice encode proteins involved in neurodevelopment and synaptic functions. Levels of some synaptic proteins in the cortex were changed, but synapse number was unaltered. Altogether, these results show that features of *Nacc1*$^{+/R284W}$ mice mimic those of the human disorder, begin to dissect the diverse molecular underpinnings of disease etiology, and provide opportunities to identify targets for therapeutic intervention.

Materials and Methods

Generation of the Nacc1$^{+/R284W}$ *mouse model*

The mutant mice were generated by the Harvard University Mouse Genome Core through a collaboration of senior investigators M.D. of Massachusetts General Hospital (MGH) and M.B. and N.A. at the University of Massachusetts Chan Medical School (UMass Chan). Utilizing CRISPR/Cas9, homologous nucleotide substitutions were introduced into the *Nacc1* gene (human: rs1060505041, cDNA 892C>T, p.298R>W; mouse: cDNA 850C>T and 852T>G, p284R>W; Fig. 1). In brief, a DNA oligonucleotide donor encoding the base pair mutations analogous to the human gene along with a single guide RNA and SpCas9 protein were injected into C57BL/6 single-cell mouse embryos (performed at Harvard University Genome Modification Facility). One founder (F17) was selected for breeding in the same C57BL/6 strain. Germline transmission through F10 generation was confirmed by sequencing, and data were collected in F1–F6 progeny. Since chimeras were not generated, traditional backcrossing up to 10 generations is not required prior to data collection (Miano et al., 2016; Liu et al., 2017). Mice were genotyped by DNA sequencing of PCR products from tail or ear DNA. In some experiments, post necropsy tissues were used for genotyping. Primer sequences are provided in Table 1.

Mouse breeding and genotyping

Mice were bred against the C57BL/6 strain at MassGeneral Hospital Institute of Neurodegeneration (MIND) and at University of Massachusetts Chan Medical School (UMass Chan). Each institution has an approved IACUC protocol for studies in these mice (protocol numbers: MGH: 2020N000173; UMass Chan: PROTO202100018). Tail snips taken on or before 21 d (~3 weeks) were used to extract DNA for genotyping. A second genotyping was performed in the mice by PCR using brain, tail, or ear snips taken at autopsy as the source of DNA. DNA was extracted with the Lambda DNA extraction kit (D300) per the manufacturers protocol. For DNA digestion performed at UMass Chan, earpieces from weaning were incubated in 90 µl 50 mM NaOH for 20 min at 95°C. Once cooled to room temperature, 10 µl of Tris HCL (pH 8.0) buffer was added to balance pH. Concentrations of DNA in the samples were measured with the ThermoFisher NanoDrop 2000 spectrophotometer if necessary. Prepared DNA samples were stored at −20°C. The Kapa Probe Fast qPCR master mix was used to amplify DNA (Roche 07959320001). The cycling protocol was 95°C for 10 min followed by 40 cycles of 92°C for 15 s and an extension at 60°C for 1 min. *Nacc1* amplification primers (see Table 1 for sequence) generated a product length of 93 base pairs. Probes were ordered from Integrated DNA Technologies and used to determine wild-type and mutant alleles (see Table 1 for primer sequences).

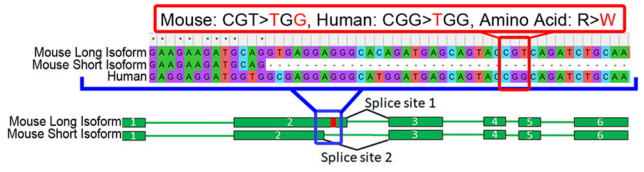

Figure 1. NACC1 mutant mouse model generation. Shown is an alignment of nucleotides in exon 2 of *Nacc1* in mouse and human. Highlighted in the red square are the nucleotides encoding the arginine (R) that is mutated to a tryptophan (W) in the NACC1 disorder for each species. Below are exons of the mouse *Nacc1* long and short isoforms depicted as green bars with their respective exon number and introns as thin green lines. The blue box pinpoints the region of mouse exon 2 in the long *Nacc1* isoform where the mutation was made (small red square).

Table 1. Sequences for guide RNA, donor DNA, genotyping probes, and primers

Reagent	Nucleotide sequence (5′-3′)		
Crispr Guide RNA	UAUACAUAUUGCAGAUCUGA		
Crispr Donor Sequence	TACCACAATGAAGAGGACGAAGAAGAAGATGCAGGTGAGGAGGGCACAGATGAGCAGTACTGGCAAATCTGCAATATGTATACAATGTACAGTATGTTG AACGTTGGCCAGACAGGTGAGTGC		
NACC1 WT genotyping Probe	AGCAGTACCGTCAGATCTGCAA		
NACC1 Mutant genotyping Probe	AGCAGTACTGGCAAATCTGCAA		
Gene	Forward Primer (5′-3′)	Reverse Primer (5′-3′)	Number of base pairs
Nacc1 (for genotyping)	AAGAAGATGCAGGTGAGGAGGG	CTGTCTGGCCAACGTTCAACAT	93
NACC1 long isoform	TGGCCAGACAGCTGAGA	GGAGAGATGCCAGGTCTTG	95
NACC1 short isoform	GTACCTCCAGTGCTTACACC	CTCTACCTTCTCAGCTGCAT	85
Total NACC1	GGCCGCTAGTAGCTCTTAC	AATGTGAGGATCTGCTGGAA	108
ActB	CATTGCTGACAGGATGCAGAAGG	TGCTGGAAGGTGGACAGTGAGG	138
GFAP	CGGAGACGCATCACCTCTG	AGGGAGTGGAGGAGTCATTCG	126
Kcne1l	AGATCCGCTGTCCTCCTCATT	GGGTTCTGACCTCTCATCATCTT	113
Hsd11b1	CAGAAATGCTCCAGGGAAAGAA	GCAGTCAATACCACATGGGC	109
Cort	GAGCGGCCTTCTGACTTTCC	GGGCTTTTTATCCAGGTGTGG	148

Analysis of motor and behavioral functions and weight

A series of tests and measurements were performed in three cohorts of mice of F4–F5 progeny between ages 2.5 and 6 months, and data were combined for all tests (Figs. 2*g*, 3*b–f*,*h*,*i*,*k–t*, 4*a–j*). Mice were group-housed by sex, with 2–5 mice per cage and were maintained on a 12 h light/dark cycle with the light cycle between 06:00 and 18:00. The order of the testing was open field, novel object recognition, Y-maze, clasping, grip strength, weight, gait analysis, and nest building (Ke et al., 2020). Mice were habituated to human handling 1 week prior to the start of behavioral tests by handling for 2 min every day for 7 consecutive days by the experimenter. The experimenters were blind to the genotypes in all experiments. Video tracking equipment (EthoVision XT8, Noldus) was used to track the mouse head, body, and tail in the open field test, novel object recognition test, and Y-maze experiments. The open field test, novel object recognition test, and Y-maze were performed consecutively from 19:00 to 23:00 during the mouse dark cycle. Indirect light was used to create a dimly lit environment to enable accurate video tracking of the mouse. The testing room is inside the barrier of the MGH animal facility which allowed mice to be returned to their housing rooms after testing. Clasping, grip strength, weight, and gait analysis were performed between 14:00 and 17:00. The nestlet test was performed starting at 18:00 and nestlets were scored and weighed at 08:00 the following day. Seventy percent ethanol was used to sterilize all environments before and after each mouse trial in all experiments.

Open field test. This test was performed as previously described (Seibenhener and Wooten, 2015) to assess motor deficits and anxiety-like behavior in 3-month-old mice. Mice were gently placed in the center of an open field box (40 cm × 40 cm, 1,600 cm^2) and allowed to explore for 10 min. The center of the open field was 32.8% of the total area (525 cm^2). Center point tracking was used to determine total distance traveled, average velocity, and total time spent in center or border regions.

Novel object recognition (NOR). To evaluate long-term memory, mice were exposed to two identical objects and then to one familiar and one novel object 24 h later (Taglialatela et al., 2009). The familiar object was a standing T-75 Flask filled with shredded white paper to eliminate transparency, and the novel object was three large Lego blocks of different colors (Fig. 4*a*). Day 1 of this test was habituation to the environment (10 min), which was performed during the open field test. During day 2, the mouse was reintroduced into the center of the open field for 5 min with two familiar objects placed in the open field, one object in the opposite quadrant as the other. During day 3, one of the familiar objects was replaced with the novel object, the mouse was introduced into the center of the environment and tracked for 5 min. Two-centimeter areas extending from an object were designated as boundary zones, and nose-point detection within the zone was used to determine mouse exploration of an object. Manual frame-by-frame correction was performed on samples where EthoVision video software flipped detection of nose–tail tracking points during recording. The discrimination index (DI) was determined by the following equation (Lueptow, 2017): DI = [(time exploring familiar object) − (time exploring novel object)] / total time exploring both objects.

Y-maze. To assess short-term spatial memory, Y-maze spontaneous alternations were assessed in control and mutant mice as previously described (Kraeuter et al., 2019). Mice were gently placed in arm A of the Y-maze and allowed to explore for 5 min. Mice were manually scored as entering an arm when the base of the tail entered the arm boundary zone. An alternation was considered when a mouse entered three different arms in a row without re-entering the previous arm. In rare occasions, mice climbed out of the apparatus. In these instances, they were placed back into the arm which they climbed out, and arm entries were reset for determining alternations. Alternation percent was determined by the following formula: Alternation % = total number of alternations / the total number of arm entries − 2.

Grip strength. Grip strength tests were performed between 14:00 and 16:00 using Columbus Instruments Grip Strength Meter (Model: 1027CSM) with the Chatillon Digital Force Gauge DFIS-2. Mice were removed from cages and held midway down their tail, slowly lowered to the grip strength bar, and allowed to grab onto the bar with both paws facing downward. Upon proper grip, mice were lowered until horizontal with the tabletop and gently pulled away from the bar until they released their grip to quantify strength. Improper gripping or pulling into the bar were registered as false readings and removed. Mice were subsequently retested. Grip strength was measured in pounds (lbs) and the apparatus zeroed and cleaned with 70% ethanol between mice. Mice were subjected to three successive trials, and the average of all three and the maximum grip strength reading were used in analysis. Mice were weighed directly before the trials to normalize grip strength data.

Gait analysis. Testing occurred at 4 months of age, between 14:00 and 16:00. The method was adapted from previous studies (Fernagut et al., 2002; Girirajan et al., 2008; Wertman et al., 2019). Walls were propped up to generate an approximate 2-inch-wide by 20-inch-long track to facilitate walking in a straight line with two pieces of 8.5 × 11 inch paper used to track steps. Mice paws were painted with nontoxic paint (forepaws, red; hindpaws, green). Mice were placed at the end of the track with a piece of food at the opposite end to influence travel. As mice traversed the track, the experimenter noted areas where the mouse had markedly run or stopped to remove these strides from analysis. At least two strides were needed to quantify stride parameters. In the rare case, a single pass through the track did not provide sufficient strides, paint was reapplied, and a second trial was administered. Stride length, stride width, and diagonal stride width were all measured in millimeters for both forepaws and hindpaws.

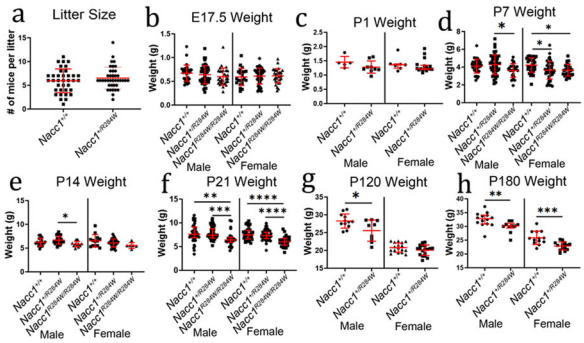

Figure 2. NACC1 mutant mouse model fertility and weight gain. ***a***, Litter size is not different between female *Nacc1*$^{+/+}$ and *Nacc1*$^{+/R284W}$ mice bred to *Nacc1*$^{+/R284W}$ males [red line depicts median with interquartile range (IQR), *Nacc1*$^{+/+}$ litters = 36 and *Nacc1*$^{+/R284W}$ litters = 39; Mann–Whitney test; $p = 0.4655$; $U = 633.5$]. ***b–h***, Body weight from E17 to P180. ***b***, There are no changes in body weight at E17.5 for *Nacc1*$^{+/+}$, *Nacc1*$^{+/R284W}$, and *Nacc1*$^{R284W/R284W}$ male or female mice [graphed red line depicts mean ± standard deviation (SD); male: *Nacc1*$^{+/+}$ $n = 32$, *Nacc1*$^{+/R284W}$ $n = 38$ and *Nacc1*$^{R284W/R284W}$ $n = 30$, one-way ANOVA with Tukey's multiple comparison, $p = 0.2914$, $F = 1.248$; female: *Nacc1*$^{+/+}$ $n = 22$, *Nacc1*$^{+/R284W}$ $n = 50$ and *Nacc1*$^{R284W/R284W}$ $n = 29$; one-way ANOVA with Tukey's multiple comparison, $p = 0.8743$, $F = 0.1345$]. ***c***, There are no changes in body weight at P1 for *Nacc1*$^{+/+}$ and *Nacc1*$^{+/R284W}$ male or female mice (male: graphed red line depicts mean ± SD, *Nacc1*$^{+/+}$ $n = 5$ and *Nacc1*$^{+/R284W}$ $n = 9$, unpaired Student's t test, $p = 0.1642$, $t = 1.482$, df = 12; female: graphed red line depicts median ± IQR, *Nacc1*$^{+/+}$ $n = 7$ and *Nacc1*$^{+/R284W}$ $n = 17$, Mann–Whitney test, $p = 0.1821$, $U = 38$). ***d***, P7 *Nacc1*$^{R284W/R284W}$ males show reduced bodyweight compared with *Nacc1*$^{+/R284W}$ males [graphed red lines depict mean ± SD, *Nacc1*$^{+/+}$ $n = 34$, *Nacc1*$^{+/R284W}$ $n = 47$, *Nacc1*$^{R284W/R284W}$ $n = 25$, Brown–Forsythe and Welch ANOVA ($p = 0.0118$, $F = 4.643$) with Dunnett's T3 multiple-comparisons test (*Nacc1*$^{+/R284W}$ vs *Nacc1*$^{R284W/R284W}$, $p = 0.0133$, $t = 2.947$, df = 64.92)]. Female *Nacc1*$^{+/R284W}$ and *Nacc1*$^{R284W/R284W}$ mice show reduced weight compared with *Nacc1*$^{+/+}$ females [graphed red lines depict mean ± SD, *Nacc1*$^{+/+}$ $n = 31$, *Nacc1*$^{+/R284W}$ $n = 45$, *Nacc1*$^{R284W/R284W}$ $n = 27$, one-way ANOVA ($p = 0.0093$, $F = 4.902$) with Tukey's multiple comparison (*Nacc1*$^{+/+}$ vs *Nacc1*$^{+/R284W}$, $p = 0.0125$, df = 100, *Nacc1*$^{+/+}$ vs *Nacc1*$^{R284W/R284W}$, $p = 0.0351$, df = 100)]. ***e***, At P14, *Nacc1*$^{R284W/R284W}$ males again show reduced bodyweight compared with *Nacc1*$^{+/R284W}$ males [graphed red lines depict mean ± SD, *Nacc1*$^{+/+}$ $n = 20$, *Nacc1*$^{+/R284W}$ $n = 24$ *Nacc1*$^{R284W/R284W}$ $n = 11$, one-way ANOVA ($p = 0.0135$, $F = 4.683$) with Tukey's multiple comparison (*Nacc1*$^{+/R284W}$ vs *Nacc1*$^{R284W/R284W}$, $p = 0.0132$, df = 52)]. There is no change in female weight (graphed red line depicts mean ± SD, *Nacc1*$^{+/+}$ $n = 13$, *Nacc1*$^{+/R284W}$ $n = 31$, *Nacc1*$^{R284W/R284W}$ $n = 6$, one-way ANOVA, $p = 0.1096$, $F = 2.318$). ***f***, At P21, *Nacc1*$^{R284W/R284W}$ males show reduced bodyweight compared with *Nacc1*$^{+/+}$ and *Nacc1*$^{+/R284W}$ males [graphed red lines depict median ± IQR, *Nacc1*$^{+/+}$ $n = 45$, *Nacc1*$^{+/R284W}$ $n = 53$, *Nacc1*$^{R284W/R284W}$ $n = 26$, Kruskal–Wallis test ($p = 0.0004$) with a Dunn's multiple-comparisons test (*Nacc1*$^{+/+}$vs *Nacc1*$^{R284W/R284W}$, $p = 0.0011$. *Nacc1*$^{+/R284W}$ vs *Nacc1*$^{R284W/R284W}$, $p = 0.0009$)]. *Nacc1*$^{R284W/R284W}$ females show reduced bodyweight compared with *Nacc1*$^{+/+}$ and *Nacc1*$^{+/R284W}$ females [graphed red lines depict mean ± SD, *Nacc1*$^{+/+}$ $n = 36$, *Nacc1*$^{+/R284W}$ $n = 46$, *Nacc1*$^{R284W/R284W}$ $n = 25$, one-way ANOVA ($p < 0.0001$, $F = 15.98$), Tukey's multiple-comparisons test (*Nacc1*$^{+/+}$vs *Nacc1*$^{R284W/R284W}$, $p < 0.0001$, df = 104, *Nacc1*$^{+/R284W}$ vs *Nacc1*$^{R284W/R284W}$, $p < 0.0001$, df = 104)]. ***g***, At P120, *Nacc1*$^{+/R284W}$ males show a reduced body weight compared with *Nacc1*$^{+/+}$ males (graphed red lines depict mean ± SD, *Nacc1*$^{+/+}$ $n = 12$, *Nacc1*$^{+/R284W}$ $n = 9$, unpaired t test, $p = 0.0229$, $t = 2.475$, df = 19). There was no change in female body weight at this time (graphed red lines depict mean ± SD, *Nacc1*$^{+/+}$ $n = 17$, *Nacc1*$^{+/R284W}$ $n = 18$, unpaired t test, $p = 0.1390$, $t = 1.516$, df = 3). ***h***, At P180, *Nacc1*$^{+/R284W}$ males showed reduced bodyweight compared with *Nacc1*$^{+/+}$ males (graphed red line depicts median ± IQR, *Nacc1*$^{+/+}$ $n = 14$, *Nacc1*$^{+/R284W}$ $n = 10$, Mann–Whitney test, $p = 0.0025$, $U = 20.5$) and female *Nacc1*$^{+/R284W}$ mice show reduced body weights compared with *Nacc1*$^{+/+}$ females (graphed red line depicts median ± IQR, *Nacc1*$^{+/+}$ $n = 13$, *Nacc1*$^{+/R284W}$ $n = 15$, Unpaired t test, $p = 0.0005$, $t = 4.0$, df = 26). For all panels, p value asterisks are determined by the following cutoffs: *$p < 0.05$, **$p < 0.01$, ***$p < 0.001$, ****$p < 0.0001$.

The base of the middle two phalanges was used as a point of reference for measurements for both fore and hindpaws. Stride length is defined as the distance a single paw travels from one step to another. Stride width is measured as the perpendicular distance between the left and right forepaws and hindpaws. Diagonal stride width is defined as the diagonal distance between the same paw on the left and right side of the mouse.

Nest building. Mice were 4 months old when tested. The nestlet test was performed as previously described (Dorninger et al., 2020). Mice were allowed to build nests for 14 h with the test starting at 18:00 and ending at 08:00. Mice were removed from their home cage and individually placed in a new cage with a preweighed unused nestlet. The following morning, mice were removed from their cage carefully so as not to disturb nestlet pieces or nests and returned to their home cage. Images were taken of the cage and nests for scoring. If any unshredded nestlet pieces remained, they were weighed (multiple unshredded pieces were combined if observed). Nests were scored on a 5-point scale with half point deductions if not all requirements were reached for a whole point score. Percent nestlet used was determined by subtracting the remaining nestlet from the prenestlet weight and dividing this value by the prenestlet weight and multiplying by 100. Scoring was modeled after Dorninger et al. (2020). Scores ranged from 1 to 5: 1, 10% or less of the nestlet was used; 2, 10–50% of the nestlet was used; 3, most or all of the neslet was used but was spread around the cage with no discernable nest identified; 4, an incomplete or flat nest was built; and 5, a near complete nest was built with 50% or more of the nest having raised walls forming a crater-like nest.

Hindlimb clasping (hindlimb retraction and paw curling). Hindlimb clasping was evaluated between 14:00 and 16:00 in three separate behavioral cohorts. Cohort 1 was measured at postnatal day (P) 14 at MGH, cohort 2 was measured at 4 months of age at MGH and cohort 3 at 6 months at UMass Chan. Mice were gently removed from their home cage and suspended by their tail 9–12 inches from the tabletop, and a video recording was made for 10 s to score. Care was made to ensure no bedding was grabbed by the mouse during removal which may induce curling. Mice were gently placed back down. Scoring was based on a scale of 0–3. A 0 is no retraction of a hindlimb to the body, a 1 is a single limb retraction to the body, a 2 is both limbs retracted to a body, and a 3 is when hindlimbs clasp together. Videos were evaluated by an observer with no knowledge of the genotypes. The amount of time spent and the extent of hindlimb clasping and paw curling were assessed in each video during the 10 s in which the mouse was held by the tail.

Weight measures. Mice in the behavior testing cohort at MGH were weighed at 4 months during the grip strength test. Mice were placed in a clean tray on top of a digital scale. Another cohort of mice bred at UMass Chan (F3 progeny) were weighed at 6 months.

EEG analysis

Mice were bred and tested at UMass Chan Medical School, Worcester, Massachusetts. Adult (3–6-month-old) *Nacc1*$^{+/R284W}$ mice ($n = 9$, 5 males and 4 females) and *Nacc1*$^{+/+}$ littermates ($n = 11$, 6 males and 5 females) from F5–F6 generation were used in this study. Naive mice were anesthetized with ketamine/xylazine (100 and 10 mg/kg, respectively, i.p.) and then placed in a stereotaxic apparatus. Mice were implanted with four EEG screw electrodes [two frontal (1 mm frontal, 1 mm lateral from bregma) and two parietal (mid-distance between bregma and lambda and 1 mm lateral from the midline)] electrodes; Pinnacle Technologies, catalog #8403) and two flexible electromyogram (EMG) wire electrodes (in the neck muscles; Plastics One, catalog #E363/76/SPC), previously soldered to a 6-pin connector (Heilind Electronics, catalog #853-43-006-10-001000), and the assembly was secured to the skull with dental cement. After completing the surgery, mice were kept in a warm environment until resuming normal activity as previously described (Anaclet et al., 2014).

Following surgery, the mice were housed individually in transparent barrels in an insulated sound-proofed recording chamber maintained at an ambient temperature of 22 ± 1°C and on a 12 h light/dark cycle (lights on at 07:00; Zeitgeber time, ZT0) with food and water available *ad libitum*. Following a minimum of 10 d for postsurgical recovery, mice were connected to flexible recording cables and habituated to the recording conditions for 5 d before starting polygraphic recordings. One cortical EEG (bipolar, frontoparietal, ipsilateral) and the EMG signals were amplified (A-M Systems 3500) and digitalized with a resolution of 256 Hz using VitalRecorder. Mice were recorded for a 48 h period.

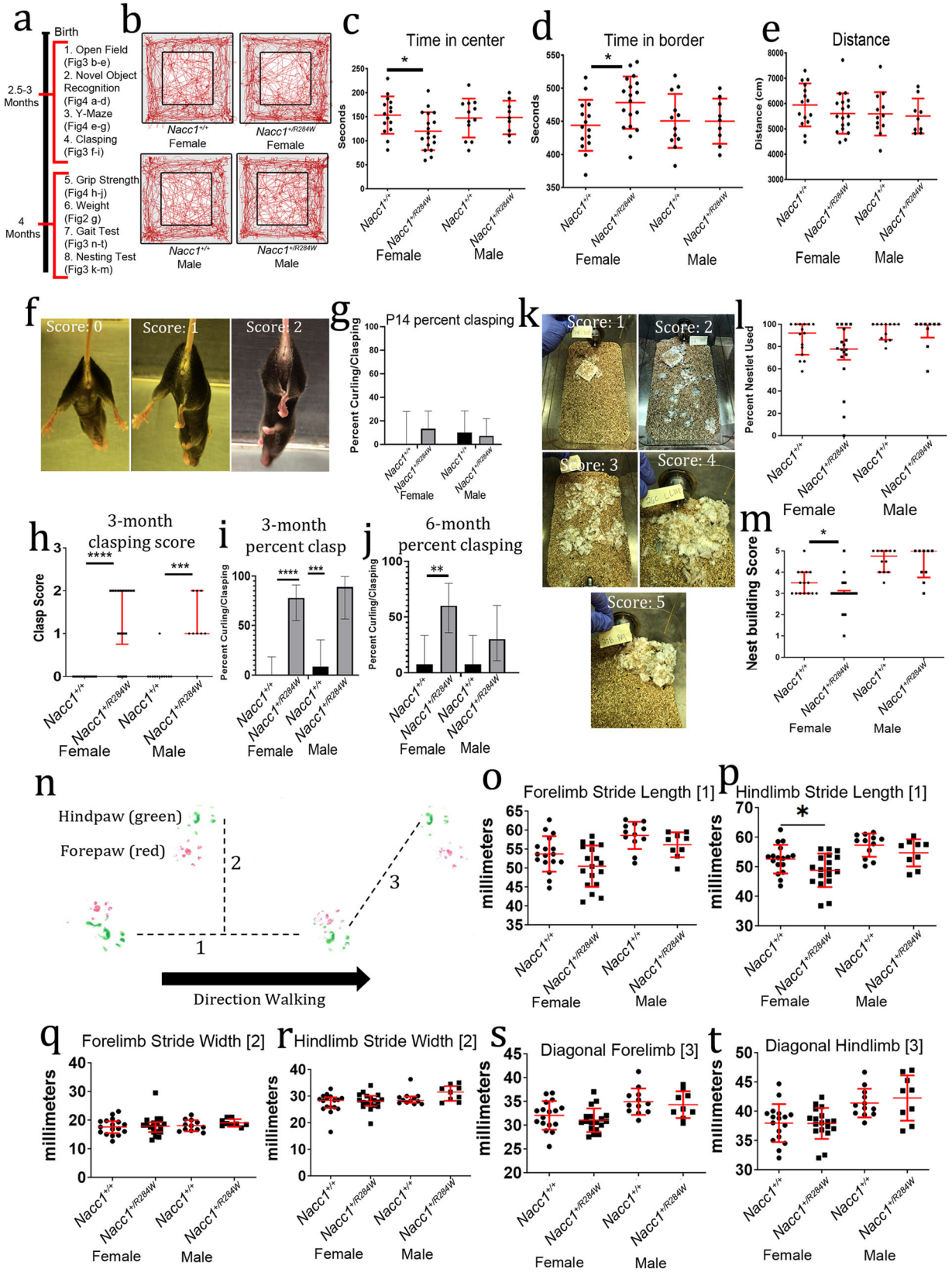

Figure 3. *Nacc1*$^{+/R284W}$ mice display behavioral and motor deficits. ***a***, Timeline of the behavioral and motor assessments reported in this figure (all panels except for ***g*** and ***j*** which were separate cohorts of mice) and Figure 4 (panels ***a–j***). The tests were performed in three cohorts of mice (F4–5 progeny between ages 2.5–6 months) and data were combined for all tests. ***b***, Representative example of results from video tracking of movements in red in the open field for *Nacc1*$^{+/+}$ and *Nacc1*$^{+/R284W}$ male and female mice. The interior square outlined in black is the center, which was 32.8% of the total arena. ***c***, Female *Nacc1*$^{+/R284W}$ mice spent less time in the center of the open field compared with *Nacc1*$^{+/+}$ littermate controls [graphed red lines depict mean ± SD, *Nacc1*$^{+/+}$ $n = 15$, *Nacc1*$^{+/R284W}$ $n = 18$, unpaired t test ($p = 0.0209$, $t = 2$, df = 31)]. There was no change between male *Nacc1*$^{+/+}$ and *Nacc1*$^{+/R284W}$ mice [graphed red lines depict mean ± SD, *Nacc1*$^{+/+}$ $n = 12$, *Nacc1*$^{+/R284W}$ $n = 9$, unpaired t test ($p = 0.9440$, $t = 0.07$, df = 19)]. ***d***, Female *Nacc1*$^{+/R284W}$ mice spent more time in the border of the open field compared with *Nacc1*$^{+/+}$ littermate controls [graphed red lines depict mean ± SD, unpaired t test ($p = 0.0176$, $t = 2.507$, df = 31)]. There was no change between male *Nacc1*$^{+/+}$ and *Nacc1*$^{+/R284W}$

Using SleepSign for Animals assisted by spectral analysis using fast Fourier transform (FFT), polygraphic records were visually scored in 10 s epochs for wakefulness, slow wave sleep (SWS), and rapid eye movement (REM) sleep. Wakefulness is characterized by low-amplitude fast-frequency EEG associated with EMG activity. SWS is characterized by high-amplitude, low-frequency EEG, and low EMG activity. REM sleep is characterized by an EEG dominated by hippocampal theta rhythm and no EMG activity (Anaclet et al., 2015). The percentage of time spent in wakefulness, SWS, and REM sleep were summarized for each group and each condition.

Recordings were scored again in 4 s epochs to allow for performance of the cortical EEG power spectral analysis. Based on visual and spectral analysis, epochs containing artifacts occurring during active wakefulness (with large movements) or containing two vigilance states were visually identified and omitted from the spectral analysis. Rescoring with a shorter epoch length allowed us to minimize the number of the recording epochs omitted from the analysis. Recordings containing artifacts during >20% of the recorded time were removed from the spectral analysis. Cortical EEG power spectra were computed for consecutive 4 s epochs within the frequency range of 0.5–60 Hz using an FFT routine. The data were collapsed into 0.5 Hz bins and standardized by expressing each frequency bin as a percentage relative to the total power of the same epochs [e.g., (bin power * 100) / 0.5 − 60 Hz total power]. To analyze the EEG frequency bands, we summed standardized power bins in delta (δ, 0.5–4.5 Hz), theta (θ, 4.5–10 Hz), sigma (σ, 10–15 Hz), beta (β, 15–30 Hz), and gamma (γ, 30–60 Hz) bands. Wakefulness, SWS, and REM sleep cortical EEG power analysis was performed on epochs free from epileptiform discharges, during two time periods, 10:00–13:00 or ZT3–6, when the mice are sleeping the most, and 19:00–22:00 or ZT12–15, when the mice are highly awake. Wakefulness and REM sleep episodes containing epileptiform discharges were analyzed separately. Overnight wakefulness and REM sleep episodes containing epileptiform discharges were included in the power spectral analysis. Epileptiform discharges occurring during the 48 h recording period were included in the quantification of the mean number and the ratio of single epileptiform discharges/repetitive epileptiform discharges. Epileptiform discharges occurring during a 24 h recording period were included in the quantification of the mean duration. When two epileptiform discharges occurred within <5 s, they were labeled repetitive epileptiform discharges. Upon completion of the recordings, mice were killed, and brains were frozen or perfused with PBS and saved for other analyses.

Primary and secondary antibodies

All primary and secondary antibodies are listed in Table 2.

Preparation of subcellular fractions

Crude homogenates. The motor cortex was dissected from frozen *Nacc1*$^{+/+}$, *Nacc1*$^{+/R284W}$, and *Nacc1*$^{R284W/R284W}$ mouse brains and homogenized in 10 mM HEPES, pH 7.2, 250 mM sucrose, 1 mM EDTA + protease inhibitor tablet (Roche) + phosphatase inhibitors 1 mM NaF and 1 mM Na_3VO_4 and sonicated for 10 s.

Nuclear and cytoplasmic fractions. Nuclear fractions were prepared using a method modified from Kegel et al. (2002). Dissected brains were homogenized in 1 ml of lysis buffer (0.1% Triton X-100, 20 nM Tricine, 250 mM sucrose, 25 mM KCl, 5 mM MgCl2, pH 7.8) supplemented with cOmplete EDTA free protease inhibitor with 12 passes in a 2 ml Dounce homogenizer using pestle A. Homogenate was transferred to an Eppendorf tube, spun at 400 × *g* for 2 min to remove large matter particulate, and the supernatant (containing nuclei and cytoplasmic components) was transferred to a new tube. The large matter particulate was resuspended in 200 µl of lysis buffer, sonicated for 10 s, and considered the crude homogenate. The lysate was spun at 2,000 × *g* for 10 min at 4°C. The supernatant was removed, sonicated for 10 s, and labeled the cytoplasmic fraction. The pellet was resuspended in 1 ml of lysis buffer and spun at 2,000 × *g* for 10 min at 4°C twice (two washes). After the second wash, the supernatant was discarded, and the pellet was resuspended in 75 µl of GAL4-IP buffer (50 mM Tris, 1% Nonidet P-40, 250 mM NaCl, 5 mM EDTA, pH 7.4) and labeled the nuclear fraction. No sonication was performed for the nuclear fraction.

Synaptosome fractions. The synaptosomes from 3-month-old *Nacc1*$^{+/+}$, *Nacc1*$^{+/R284W}$, and *Nacc1*$^{R284W/R284W}$ mice were prepared as previously described (Valencia et al., 2013; Sapp et al., 2020). Briefly, small pieces of the somatosensory/visual cortex were homogenized in 7 ml 0.32 M sucrose and centrifuged at 1,000 × *g*, and the postnuclear supernatant was layered on an equal volume of 1.2 M sucrose. This

←

mice [graphed red lines depict mean ± SD, unpaired *t* test ($p = 0.9815$, $t = 0.0235$, df = 19)]. ***e***, There were no changes in the total distance traveled between *Nacc1*$^{+/+}$ and *Nacc1*$^{+/R284W}$ females and males [graphed red lines depict mean ± SD, unpaired *t* test (female: $p = 0.2457$, $t = 1.183$, df = 31; male: $p = 0.8077$, $t = 0.2468$, df = 19)]. ***f***, Examples of mice suspended by the tail and exhibiting hindlimbs splayed (Score 0), one hindlimb retracted (Score 1), and both hindlimbs retracted (Score 2). ***g***, There is no change in the percent of mice clasping at P14 (bars represent the mean percent clasping with error bars representing the upper and lower confidence interval limits; female: *Nacc1*$^{+/+}$ $n = 9$, *Nacc1*$^{+/R284W}$ $n = 24$, chi-squared test: $p = 0.2788$, $X^2 = 2.555$, df = 2; male: *Nacc1*$^{+/+}$ $n = 16$, *Nacc1*$^{+/R284W}$ $n = 22$, chi-squared test: $p = 0.9355$, $X^2 = 1.377$, df = 2). ***h***, *Nacc1*$^{+/R284W}$ females and males scored significantly higher in the hindlimb clasping test in the 3 month cohort [red line depicts median and IQR, Mann–Whitney test (female: *Nacc1*$^{+/+}$ $n = 17$, *Nacc1*$^{+/R284W}$ $n = 18$, $p < 0.0001$, $U = 34$; male: *Nacc1*$^{+/+}$ $n = 12$, *Nacc1*$^{+/R284W}$ $n = 9$, $p = 0.0002$, $U = 9$)]. ***i***, A greater percentage of *Nacc1*$^{+/R284W}$ females and males displayed hindlimb clasping at 3 months (bars represent the mean percent clasping with error bars representing the upper and lower confidence interval limits; female: *Nacc1*$^{+/+}$ $n = 17$, *Nacc1*$^{+/R284W}$ $n = 18$, Fisher's exact test: $p < 0.0001$; male: *Nacc1*$^{+/+}$ $n = 12$, *Nacc1*$^{+/R284W}$ $n = 9$, Fisher's exact test: $p = 0.0002$). ***j***, *Nacc1*$^{+/R284W}$ females displayed hindlimb clasping at 6 months while males showed a trend to displaying more hindlimb clasping but did not reach significance [bars represent the mean percent clasping with error bars representing the upper and lower confidence interval limits (female: *Nacc1*$^{+/+}$ $n = 13$, *Nacc1*$^{+/R284W}$ $n = 15$, Fisher's exact test: $p < 0.0060$; male: *Nacc1*$^{+/+}$ $n = 13$, *Nacc1*$^{+/R284W}$ $n = 10$, Fisher's exact test: $p = 0.2806$)]. Study was performed at UMass Chan. ***k***, Representative images of nest building and assigned scores: A score of 1 was given if <10% of the nestlet was shredded, a score of 2 was given if 10–50% of the nestlet was shredded, a score of 3 was given when >50% of the nestlet was shredded but not gathered into a nest. A score of 4 was assigned when there was an identifiable but flat nest with >90% of the nestlet shredded and gathered into a quarter of the cage. A score of 5 was given when a fully formed nest consisted of walls larger than the mouse for >50% circumference and over 90% of the nestlet shredded. ***l***, There was no change in the percentage of nestlet used between *Nacc1*$^{+/+}$ and *Nacc1*$^{+/R284W}$ females or males [red lines indicate median ± IQR (females: *Nacc1*$^{+/+}$ $n = 15$, *Nacc1*$^{+/R284W}$ $n = 18$, Mann–Whitney test: $p = 0.1748$, $U = 97.50$; males: *Nacc1*$^{+/+}$ $n = 12$, *Nacc1*$^{+/R284W}$ $n = 9$, Mann–Whitney test: $p = 0.8389$, $U = 51.0$)]. ***m***, Nestlet scores are reduced in female *Nacc1*$^{+/R284W}$ compared with those in *Nacc1*$^{+/+}$ but not in males [red lines indicate median ± IQR (females: Mann–Whitney test: $p = 0.0374$, $U = 82.00$; males: Mann–Whitney test: $p = 0.8164$, $U = 50.50$)]. ***n***, Representative paw prints from gait analysis. Forepaws are labeled red and hindpaws are green. Stride length is the distance traveled of a single limb from one stride to the next (#1). Stride width is the perpendicular distance from a forepaw or hindpaw print to the stride length measured in the opposite side of the body (#2). Diagonal stride width is the distance from the left paw to the respective right paw between strides (#3). ***o–t***, Gait measurements. ***o***, Forepaw stride length was not changed in males or females (unpaired Student's *t* test; female: $p = 0.677$, $t = 1.889$, df = 33; male: $p = 0.1231$, $t = 1.614$, df = 19). ***p***, Hindlimb stride length was reduced for female *Nacc1*$^{+/R284W}$ mice but not males (unpaired *t* test; females: $p = 0.0406$, $t = 2.131$, df = 33; males: $p = 0.1810$, $t = 1.389$, df = 19). ***q***, Forelimb stride width was not changed in male or female *Nacc1*$^{+/R284W}$ mice (female: Mann–Whitney test, $p = 9935$, $U = 152.5$; male: unpaired Student's *t* test, $p = 0.2122$, $t = 1.294$, df = 19). ***r***, Hindlimb stride width was not changed in *Nacc1*$^{+/R284W}$ females or males (Mann–Whitney test; female: $p = 0.6420$, $U = 138.5$; males: $p = 0.1066$, $U = 31$). ***s***, Diagonal forepaw stride width was not changed in *Nacc1*$^{+/R284W}$ males or females (unpaired Student's *t* test; female: $p = 0.2786$, $t = 1.102$, df = 33; male: $p = 0.6129$, $t = 0.5144$, df = 19). ***t***, Diagonal hindpaw stride width was not changed in *Nacc1*$^{+/R284W}$ males or females (unpaired Student's *t* test; female: $p = 0.9525$, $t = 0.06003$, df = 33; male: $p = 0.5354$, $t = 0.6312$, df = 19). For all tests female *Nacc1*$^{+/+}$ $n = 17$, *Nacc1*$^{+/R284W}$ $n = 18$ and male *Nacc1*$^{+/+}$ $n = 12$, *Nacc1*$^{+/R284W}$ $n = 9$. Red lines indicate mean ± SD in panels ***o***, ***p***, ***q*** (male), ***s*** and ***t***. Median ± IQR is graphed in panels ***q*** (female) and ***r***. For all panels, horizontal black bars are comparisons between groups and number of asterisks indicate *p* values with the following cutoffs: *$p < 0.05$, **$p < 0.01$, ***$p < 0.001$, ****$p < 0.0001$.

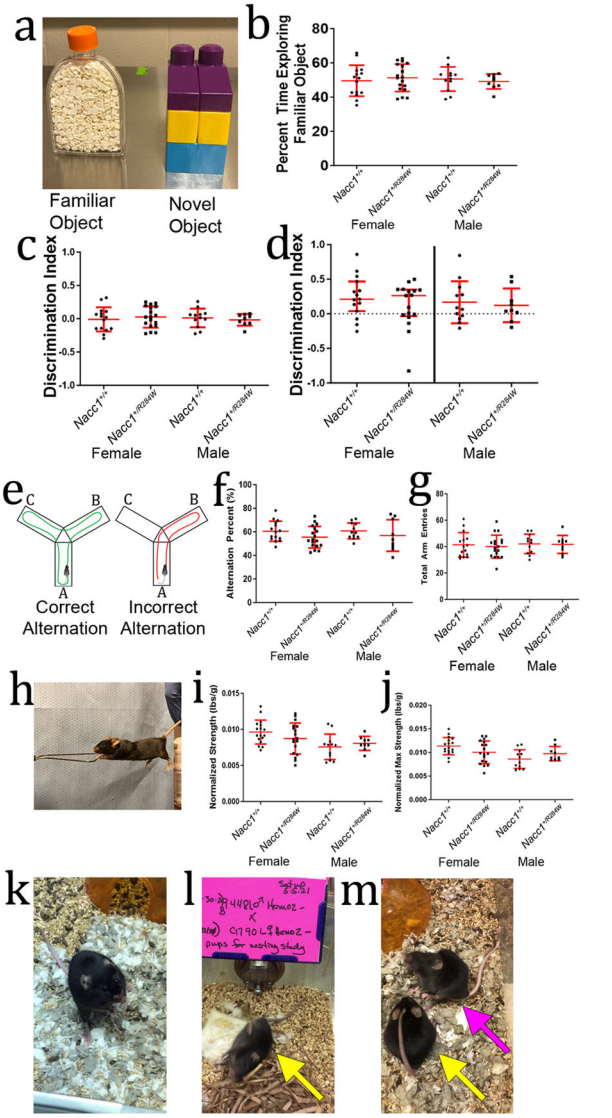

Figure 4. *Nacc1*$^{+/R284W}$ mice do not display memory deficits in the novel object test and Y-maze and do not have reduced normalized grip strength but do exhibit behavioral seizures after 7 months of age. ***a***, Images of the novel objects used in the study. On the left is a T75 flask filled with square paper pieces compared with a square multicolor mega block structure. ***b***, *Nacc1*$^{+/+}$ and *Nacc1*$^{+/R284W}$ female or male mice showed no changes in percent time exploring either familiar object 1 (which will remain the familiar object in day 2 experimentation) or familiar object 2 (which will be replaced with the novel object). Graphed lines depict mean ± SD for percent time exploring familiar object 2 (unpaired Student's *t* tests; female: $p = 0.5672$, $t = 0.5783$, df = 31; male: $p = 0.5933$, $t = 0.5432$, df = 19). ***c***, Positive DI values indicate a preference for familiar object 2 (or the day 2 novel object) and negative values show preference for familiar object 1. Quantification of the DI reveals no observed differences between *Nacc1*$^{+/+}$ and *Nacc1*$^{+/R284W}$ female or male mice (graphed red lines depict mean ± SD; unpaired Student's *t* test were performed; females: $p = 0.5672$, $t = 0.5783$, df = 31; males: $p = 0.5933$, $t = 0.5432$, df = 19). Of note, object placement was not randomized, and these data support the lack of preference for a specific object placement. ***d***, Day 2 novel object preference. Quantification of the DI reveals no observed differences between *Nacc1*$^{+/+}$ and *Nacc1*$^{+/R284W}$ female or male mice [graphed red lines depict median ± IQR for females and mean ± SD for males (females: *Nacc1*$^{+/+}$ $n = 15$, *Nacc1*$^{+/R284W}$ $n = 17$, Mann–Whitney test: $p = 0.5209$, $U = 110.0$; males: *Nacc1*$^{+/+}$ $n = 12$, *Nacc1*$^{+/R284W}$ $n = 9$, unpaired *t* test, $p = 0.7241$, $t = 0.3582$, df = 19)]. One female was removed from *Nacc1*$^{+/R284W}$ analysis as an outlier due to exploring both objects for <5 s combined. ***e***, Schematic of the Y-maze used to measure spontaneous alternation. A positive alternation is highlighted with a green track, where a mouse visits each arm consecutively without re-entering a previous arm. If a mouse re-enters an arm it just came from, then it would be considered an incorrect alternation highlighted by the red track. ***f***, Percentage of successful alternations was not different between *Nacc1*$^{+/+}$ and *Nacc1*$^{+/R284W}$ mice [graphed red lines depict mean ± SD (female: *Nacc1*$^{+/+}$ $n = 15$, *Nacc1*$^{+/R284W}$ $n = 18$, unpaired Student's *t* test: $p = 0.4406$, $t = 0.80$, df = 11.05; males: *Nacc1*$^{+/+}$ $n = 12$, *Nacc1*$^{+/R284W}$ $n = 9$, unpaired *t* test, $p = 0.1138$, $t = 1.627$, df = 31)]. ***g***, Total arm entries were not different between *Nacc1*$^{+/+}$ and *Nacc1*$^{+/R284W}$ mice [graphed red lines depict mean ± SD (female: unpaired Student's *t* test, $p = 0.6738$, $t = 0.4249$, df = 31.0; males: unpaired *t* test, $p = 0.8958$, $t = 0.1327$, df = 19)]. ***h***, Representative image of a mouse undergoing grip strength testing. ***i***, Average grip strength normalized to weight was not different between *Nacc1*$^{+/+}$ and *Nacc1*$^{+/R284W}$ female or male mice [graphed red lines depict mean ± SD (female: unpaired Student's *t* test, $p = 0.1786$, $t = 1.374$, df = 33.0; males: unpaired *t* test, $p = 0.4613$, $t = 0.7519$, df = 19)]. ***j***, Maximum grip strength normalized to weight was not different between *Nacc1*$^{+/+}$ and *Nacc1*$^{+/R284W}$ mice [graphed red lines depict mean ± SD (female: unpaired Student's *t* test, $p = 0.0781$, $t = 1.818$, df = 33.0; males: unpaired *t* test, $p = 0.1666$, $t = 1.438$, df = 19)]. ***k***, Representative still image from Movie 1 with a female *Nacc1*$^{+/R284W}$ mouse frozen in a rearing position displaying a behavioral seizure. ***l***, Representative still image from Movie 2 with a male *Nacc1*$^{R284W/R284W}$ mouse displaying erratic flipping during a behavioral seizure (yellow arrow). ***m***, Representative still image from Movie 3 with two female *Nacc1*$^{R284W/R284W}$ mice displaying seizures. One mouse (purple arrow) displayed repetitive head bobbing and twitching, rearing, and collapsing while the second mouse (yellow arrow) displayed head bobbing and tail stiffening and raising. For all panels, number of asterisks indicate *p* values with the following cutoffs: *$p < 0.05$, **$p < 0.01$, ***$p < 0.001$, ****$p < 0.0001$.

was further centrifuged at 160,000 × *g* in a SW41 swinging bucket rotor, and the synaptosomes were collected at the interface between the two sucrose layers.

Western blot assays and quantification

Protein concentrations for crude homogenates, nuclear fractions, and synaptosomes were determined using the Bradford method (Bio-Rad). Proteins (10 µg for crude homogenates, 4 µg per for nuclear and cytoplasmic fractions, and 5 µg for synaptosomes) were separated by SDS-PAGE using 4–12% Bis-Tris gels (Invitrogen or Bio-Rad) and transferred to nitrocellulose using Trans-Blot Turbo (Bio-Rad). Blots were then cut horizontally to maximize the number of antibodies that could be analyzed by Western blot. Blots were blocked in 5% milk/TBS + 0.1% Tween 20 (TBST) and primary antibodies were diluted in blocking buffer and incubated with blots overnight at 4°C with agitation. After washing in TBST, blots were incubated in secondary antibodies diluted 1:5,000 in blocking buffer for 1 h at room temperature. Blots were washed in TBST, and bands were visualized using SuperSignal West Pico PLUS Chemiluminescent Substrate (Thermo Fisher Scientific), and images were captured with a CCD camera (Alpha Innotech) or exposed to Hyperfilm ECL (GE Healthcare). The blots were stripped with Restore Stripping buffer (Thermo Fisher Scientific) and reprobed up to four times with different antibodies.

Digital images were used for quantification unless signal was very low and bands could only be detected using film. Each band was manually circled using ImageJ software (NIH), and total signal intensity was determined by multiplying area by average intensity. Proteins that served as loading controls were GAPDH, actin, and histone H3. Graphs presented in results depict signal intensity for each band normalized to the loading control. NACC1 antibody from Abcam (#29047) was used for all Western blots unless otherwise noted.

Immunofluorescence and histochemistry

Tissue harvest. Four pairs of 2-month-old (P60) mice and three pairs of 3-month-old mice were anesthetized with tribromoethanol 284 mg/kg, and 3-month-old mice were anesthetized with 110 mg/ml ketamine and 20 mg/ml xylazine. Mice received a transcardial perfusion with 50 ml of ice-cold PBS followed by 50 ml of 4% (w/v) paraformaldehyde (PFA, Sigma-Aldrich) in PBS, pH 7.4. Brains were postfixed overnight in 4% PFA, washed, and stored in PBS + 0.02% sodium azide. Three-month-old brains were cut in half at the sagittal midline, and half of the brain was used for immunofluorescence and the other for cresyl violet and Luxol fast blue stains.

Immunofluorescence. Fixed brains were cut into series of 30-µm-thick coronal sections on a vibratome (Leica VT1000S). Immunolabeling was performed with free-floating brain sections from

Table 2. Primary and secondary antibodies used for Western blot and immunofluorescence

Primary antibodies					
Antigen	Species raised	Vendor	Catalog number	Concentration used for immunofluorescence	Concentration used for Western blot
Actin	Mouse	Sigma	A4700		1:500
Aldh1l1	Rabbit	Abcam	ab190298		1:5,000
FoxG1	Rabbit	Abcam	ab18259		1:1,000
GAPDH	Mouse	EMD Millipore	MAB374		1:10,000
GFAP	Mouse	Sigma	G3893	1:400	
HDAC3	Rabbit	Abcam	ab32369-7	1:500	
Histone H3	Rabbit	EMD Millipore	06-755		1:750
Homer1	Rabbit	EMD Millipore	ABN37		1:8,000
IBA-1	Goat	Abcam	ab5076	1:500	
NACC1	Rabbit	Abcam	29047	1:3,000	1:1,000
NACC1	Rabbit	ThermoFisher	41656		1:2,000
NeuN	Mouse	EMD Millipore	MAB377	1:100	
Olig2	Mouse	EMD Millipore	MABN50	1:50	
Parvalbumin	Mouse	Sigma	P3088	1:500	
Prosapip1	Rabbit	Proteintech	24936-1-AP		1:500
PSD95	Rabbit	Cell Signaling	2507		1:500
s100b	Mouse	Sigma	s2657	1:250	
SNAP-25	Mouse	BD Transduction Laboratories	610366		1:5,000
Synaptophysin	Mouse	Boehringer Mannheim Biochemical	902314		1:5,000
VAMP2	Rabbit	Abcam	ab18014	1:1,000	
20 s Proteasome	Rabbit	ICN Biomedicals	N/A		1:5,000

Secondary antibodies					
Antigen	Vendor	Catalog number	Peroxidase or fluorophore conjugation	Concentration used for Immunofluorescence	Concentration used for Western blot
Rabbit IgG	Jackson ImmunoResearch	711-035-152	Peroxidase	1:500	1:2,500
Mouse IgG	Jackson ImmunoResearch	715-035-150	Peroxidase	1:500	1:5,000
Mouse IgG	Jackson ImmunoResearch	115-545-166	AlexaFluor 488	1:500	
Rabbit IgG	Jackson ImmunoResearch	111-295-144	Rhomadine red	1:500	
Rabbit IgG	Jackson ImmunoResearch	715-295-150	Rhomadine red	1:200	
Goat IgG	Jackson ImmunoResearch	705-545-003	AlexaFluor 488	1:400	
Mouse IgG	Molecular Probes	B2752	BODIPY	1:500	

three consecutive sections. Blocking and permeabilization were performed together by incubating in 5% NDS or NGS in PBS with 0.2% Triton X-100 for 1 h. After three quick washes in PBS with 0.05% Triton X-100, the tissue slices were incubated in primary antibodies for 72 h followed by secondary antibodies conjugated to different fluorochromes for 2 h. Nuclei were identified by Hoechst 34580 staining. Brain sections were mounted onto glass slides, allowed to dry for ∼1 h, covered with ProLong Gold (Invitrogen, 36930) followed by a coverslip, and then examined using an Olympus FV3000 confocal microscope with 10×, 40×, and 60× objectives.

Image acquisition and measurements. In sections of 3-month-old mice, images were captured from three consecutive coronal sections of each mouse ($n = 2$ mice per genotype) with an Olympus confocal microscope Fv3000 with a 10× objective that was equipped with a motorized stage and software capable of producing "stitched" images. Images were analyzed using NIH ImageJ after converting to 8 bit black and white images, with background signals removed from the corresponding images.

For measurement of intensity of NACC1 immunoreactivity in neuronal nuclei, four pairs of $Nacc1^{+/+}$, $Nacc1^{+/R284W}$, and $Nacc1^{R284/R284W}$ mice aged to P60 were used. For each mouse, 3 consecutive coronal slices were stained. Within each coronal slice, two images were captured in the center of the tissue slice at 40× in layers 2/3, 5, and 6 of the motor cortex. A total of 30 nuclei were counted per mouse for each cortical layer. Sections were double labeled with the neuronal nuclear marker NeuN and NACC1. Measurement of relative NACC1 staining intensity in neuronal nuclei was determined using ImageJ/Fiji. Each nucleus was outlined using the freehand selection tool, and the cross-sectional average signal intensity was obtained using the measure function for both NACC1 and NeuN. Background intensities were determined by manually drawing three areas in regions where no nuclei or cell bodies were found. Fold change in NACC1 intensity for each nucleus was determined by the following formula: ([NACC1 Intensity − average background NACC1 intensity] / [NeuN Intensity − average background NeuN intensity]) for each nucleus quantified. To normalize fold change intensities across pairs (plotted as the final graphed values), we then further divided all values for $Nacc1^{+/+}$, $Nacc1^{+/R284W}$, and $Nacc1^{R284W/R284W}$ by the average $Nacc1^{+/+}$ value from their respective mouse pair. Statistical analysis was performed between genotypes for all motor cortex layers using a Kruskal–Wallis test followed by Dunn's multiple-comparisons post hoc analysis.

Cresyl violet and Luxol fast blue stains. Half brains were placed in 30% sucrose overnight at 4°C for cryopreservation. Brains were immersed into OCT and sagittal slices cut at 30 µm with a Microm HM 550 cryostat. Slices were directly mounted onto gelatin-coated slides and let dry onto the slide. Cresyl violet stain: Tissue was rehydrated with a 1 min immersion of slides in a decreasing ethanol rehydration series: 100%, 90%, 70% (+1% glacial acetic acid), 50% followed by a 2 min incubation in ddH_2O to remove OCT and a second wash in clean ddH_2O for 1 min. Slides were stained in 1% cresyl violet (1 g cresyl violet, 250 µl glacial acetic acid and made up to 100 ml in ddH_2O) for 15 min. Sections were then rinsed for 1 min in ddH_2O and dehydrated in a series of increasing ethanol percentages: 50%, 70% with glacial acetic acid, 95% and 100% for 2 min each. Two xylene washes were performed for 5 min each and slides were coverslipped with Cytoseal. Luxol fast blue stain: Dehydrated slides were incubated in Luxol fast blue stain (0.25 g Luxol fast blue MBS into 250 ml 95% ethanol and filtered) at 60°C for 30 min and allowed to cool. Slides were placed in the following series of ethanol rehydration solutions for 5 min per solution: 95%, 80%, 70%, 50% ethanol. Slides were then washed with ddH_2O for 5 min and dehydrated in the same series of solutions used for the cresyl violet stain and sealed with Cytoseal.

Electron microscopy

Brains from 3-month-old mice (2 $Nacc1^{+/+}$ females and 2 $Nacc1^{+/R284W}$ females) were perfused with 2% PFA and 2% glutaraldehyde and stored in PBS at 4°C. Fifty-micrometer sections were cut on a Leica VT1000S Vibratome, and every fourth section throughout the brain was incubated in 1% osmium tetroxide/PBS and then 1% uranyl acetate/70% ethanol and dehydrated in increasing grades of alcohol before embedding in EPON-Araldite on coated glass slides. The motor cortex was dissected from equivalent sections from all brains, and pieces were mounted on Epon blocks where ultrathin sections were cut from two blocks from each mouse using a Reichert-Jung Ultracut and mounted on copper grids. Sections were examined using a JEM-1011 (JEOL) electron microscope, and images of neuropil were taken at 20,000× magnification using AMTv601 software (Advanced Microscopy Techniques imaging). Quantitative analysis was performed by someone with no knowledge of the genotypes using ImageJ/Fiji. Synapses between profiles were identified based on the presence of opposing membranes, the presence of presynaptic vesicles, and postsynaptic densities. The number and length of synaptic contacts were recorded in each image.

RNA extractions, sequencing, and bioinformatics

For the RNA-sequencing analysis, 18 total mice were used. Three males and three females were used from each genotype ($Nacc1^{+/+}$, $Nacc1^{+/R284W}$, and $Nacc1^{R284W/R284W}$). P14 mice (F5/F6 progeny) used for RNA sequencing were anesthetized using CO_2. Brains were extracted, hemispheres cut in half, and placed in RNAlater (AM7021) per the manufacturers protocol for storage at −80°C. To dissect the motor cortex, we placed the brains into a brain matrix (Zivic Instruments, BSMAS001-1) and made coronal slices. Slices were transferred to a Petri dish with RNAlater, and 1.5 mm punches were made (Integra Miltex, #69031-02) approximately between bregma 1.77 and 0.85 mm. Punches were stored at −80°C. RNA was extracted using the Qiagen RNeasy mini kit (#74104) per the manufacturer's protocol and subject to the additional on column DNase digestion (Qiagen, 79254). Purified RNA was stored at −80°C.

Sequencing and bioinformatic analysis were performed by Novogene. Purified RNA was shipped to Novogene where it was assessed for abundance and quality using a spectrophotometer (260/280 > 1.8, 260/230 > 1.8), and RNA integrity was determined using the Agilent Bioanalyzer 2100. RIN values ranged from 7.6 to 9.4 for P14 cortex samples. One-hundred fifty base pair end sequencing were performed. Reads were mapped to the mm10 mouse reference genome. The DESeq2 package was used to identify differentially expressed genes (DEGs) and nominal p values were adjusted using the Benjamini–Hochberg approach. DEGs based on nominal and/or adjusted p value <0.05 are indicated in the Results. Pathway-level analysis included use of gene ontology (GO), KEGG, and Reactome databases based on DEGs with a nominal p value cutoff of 0.05. For sex-specific results, DEGs which were common to both females and males were subtracted from female- and male-specific DEG lists. The remaining DEGs were then compared between females and males for $Nacc1^{+/R284W}$ and $Nacc1^{R284W/R284W}$ mice. The unique number of DEGs and top DEGs specific to each sex were reported in the Results.

cDNA preparation and quantitative PCR (qPCR) for gene expression analysis

cDNA preparation for 6 months and P14 cortical samples. To generate cDNA, we performed reverse transcription using the SuperScript III First-Strand Synthesis kit (ThermoFisher 18080400) according to manufacturer's protocol. In total, 500 ng reactions using the oligo-dT_{20} primer pair were used to generate a 16.6 ng/µl final reaction concentration.

Primers. Four total primer pairs were used to detect *Nacc1* mRNA: *Nacc1* long isoform, *Nacc1* short isoform, exon 2 (present in both isoforms), and a primer for the ActB gene which was used as a control (Korutla et al., 2002). Primer sequences for these transcripts are in Table 1. RNA extracted from the motor cortex of P14 and 6-month-old $Nacc1^{+/+}$ mice was used as a template to generate cDNAs and to check that the four primer sets generated products that migrated to their expected sizes. In addition, primers were generated for DEGs to verify by qPCR the results from RNA sequencing (Table 1).

qPCR parameters and quantification. For qPCR, PowerUp Sybr Green Master Mix (ThermoFisher #25742) was used. In total, 10 µl reactions were made with final concentrations of forward and reverse primers at 200 nM. Reactions were run on the BioRadCFX96 system. For *Nacc1* isoform expression levels, 16.6 ng were used per reaction. For all other gene expression experiments 4 ng of cDNA was used per reaction. Cycling parameters were as follows: UDG activation at 50°C for 2 min, Dual-Lock DNA Polymerase at 95°C for 2 min, 40 cycles of denaturation at 95°C for 15 s followed by annealing and extension at 60°C for 1 min. For qPCR quantification, the $2^{-\Delta\Delta Cq}$ method was used to quantify relative transcript abundance (Livak and Schmittgen, 2001). ActB was used as a housekeeping gene in qRT-PCR analysis. Cq values were determined by manually applying a threshold in the logarithmic phase of amplification.

Experimental design and statistical analysis

Continuous quantitative data were first subject to Shapiro–Wilk's test to determine if the data was normally distributed. An unpaired two-tailed Student's t test was performed for normally distributed data with equal variance. A two-tailed Student's t test with Welch's correction was performed for normally distributed data with unequal variance. A one-way ANOVA with a post hoc Tukey's multiple comparison was performed to compare three independent normally distributed groups with equal variance. If variance was unequal for three normally distributed groups, then a Brown–Forsythe ANOVA with Dunnett's T3 correction was used. For EEG analysis, two-way ANOVAs were performed followed by a post hoc Bonferroni's test to compare the effect of the genotype or to compare the power spectral bands between episodes free of epileptiform discharges versus episodes containing epileptiform discharges. If data were not normally distributed, then nonparametric tests were performed. The Mann–Whitney U test was used to compare two non-normally distributed data. The Kruskal–Wallis test with a post hoc Dunn's multiple-comparisons test was used to compare three non-normally distributed independent groups. For categorical outcomes, a Fisher's exact test was performed for 2 × 2 comparisons, and a chi-squared test was performed for comparisons greater than 2 × 2. Due to weights being measured at different ages or from separate cohorts of mice, different statistical tests were used for different aged mice or between each sex.

Results

Generation of $Nacc1^{+/R284W}$ mice

The *Nacc1* genes in human and mouse are ∼87% homologous and the site encoding the arginine to tryptophan (R>W) in human is conserved in mouse. The human gene encodes one transcript, and the mouse has two, designated as long and short

which were identified first in rodent brain (Cha et al., 1997; Korutla et al., 2002; Mackler et al., 2003). Only the long isoform in mouse contains sequence corresponding to R>W in human (Fig. 1). Utilizing CRISPR-Cas9, we generated the first knock-in mouse model of the disorder through introducing the homologous nucleotide substitutions in the *Nacc1* gene (human: rs1060505041, cDNA 892C>T, p.298R>W; mouse: cDNA 850C>T and 852T>G, p284R>W; Fig. 1). In brief, a DNA oligonucleotide donor encoding the base pair mutation analogous to the human gene along with a single guide RNA and SpCas9 protein were injected into C57BL/6 single-cell mouse embryos. One founder (F17) was selected for breeding and backcrossing in the C57BL/6 strain. Germline transmission through F9 generation was confirmed by sequencing, and most data reported here were collected in F3–F6 progeny. Mice were genotyped by DNA sequencing of PCR products from tail or ear DNA. In some experiments, post necropsy tissues were used for genotyping. Guide RNA, the donor DNA sequence, and primer sequences are reported in Table 1.

Postnatal litter size, survival at different ages, and weight gain

The size of litters from $Nacc1^{+/+}$ and $Nacc1^{+/R284W}$ females mated to $Nacc1^{+/R284W}$ males were not different suggesting the mutation did not affect fertility (Fig. 2*a*). To determine if genotype distribution differed from the expected 1:2:1 Mendelian outcome, litters from $Nacc1^{+/R284W} \times Nacc1^{+/R284W}$ mating pairs were scored for genotype at different ages [embryonic day (E) 17.5, P7, and P21]. At E17.5 and P7, there was no change in the distribution of $Nacc1^{+/+}$, $Nacc1^{+/R284W}$, and $Nacc1^{R284W/R284W}$ genotypes (Table 3). Mice genotyped at P21 (their weaning period) showed reduced percentages of the $Nacc1^{R284W/R284W}$ genotype for both males and females (Table 3). These data suggested that between P7 and P21, mice with two mutant alleles may undergo premature death. Longer survival periods were not examined systematically, however, two other groups from F5 generation (11 heterozygotes) and F6 generation (4 homozygotes) were aged past 8 months with no premature deaths, and 24 $Nacc1^{+/R284W}$ mice from the F1 generation that were aged to 13 months and 20 from F4 and F5 aged to between 11 and 17 months at UMass Chan had no premature deaths. Overall, these results indicate that $Nacc1^{+/+}$ and $Nacc1^{+/R284W}$ mice have normal fertility and survival but $Nacc1^{R284W/R284W}$ mice could be at increased risk of neonatal death closer to weaning.

Weights were measured across several different cohorts of mice between E17.5 to 6 months in age at the two test sites (MGH and UMass Chan; Fig. 2*b–h*). There were no changes in weight at E17.5 between $Nacc1^{+/+}$, $Nacc1^{+/R284W}$, and $Nacc1^{R284W/R284W}$ mice (Fig. 2*b*, UMass Chan site) and at P1 between $Nacc1^{+/+}$ and $Nacc1^{+/R284W}$ mice (Fig. 2*c*, MGH site). P7 male $Nacc1^{R284W/R284W}$ showed reduced weight compared with $Nacc1^{+/R284W}$ males while $Nacc1^{+/R284W}$ and $Nacc1^{R284W/R284W}$ females showed reduced weight compared with $Nacc1^{+/+}$ females (Fig. 2*d*, UMass Chan site). At P14, $Nacc1^{R284W/R284W}$ males also showed a reduced weight compared with $Nacc1^{+/R284W}$ males and while the trend remained for female $Nacc1^{R284W/R284W}$, there was no change in female weight observed (Fig. 2*e*, MGH site). At P21, $Nacc1^{R284W/R284W}$ males and females showed reduced weight compared with $Nacc1^{+/R284W}$ and $Nacc1^{+/+}$ mice (Fig. 2*f*, UMass Chan site). Both P120 and P180 $Nacc1^{+/R284W}$ males showed reduced weight compared with $Nacc1^{+/+}$ males (Fig. 2*g*, MGH, and 2*h*, UMass Chan, respectively) while only P180 $Nacc1^{+/R284W}$ females showed a reduced weight compared with $Nacc1^{+/+}$ females (Fig. 2*h*, UMass Chan). Altogether this analysis suggested that mice with the Nacc1 R284W mutation from P7 to 6 months had delayed weight gain with $Nacc1^{R284W/R284W}$ displaying more consistent reduced weight gain for both males and females while $Nacc1^{+/R284W}$ mice showed sex-dependent changes as some ages. The delayed weight gain for $Nacc1^{R284W/R284W}$ mimics an early symptom of delayed weight gain seen in patients that contributes to a failure to thrive (Schoch et al., 2017).

Absence of cataracts in *Nacc1* mutant mice

Bilateral cataracts identified between birth and 10 years of age were found in five of seven of the individuals first identified with the *NACC1* R298W mutation (Schoch et al., 2017). No cataracts were evident in nine $Nacc1^{+/R284W}$ and four $Nacc1^{R284W/R284W}$ mice aged 1.5–5months using the method of observation described by He et al. (2019). This indicates that formation of cataracts, at least at early ages, is not a phenotype in mice with the *Nacc1* R284W mutation. Cataracts were not reported in two mouse models with deletion of the *Nacc1* gene (Yap et al., 2013; da Silva-Buttkus et al., 2023).

$Nacc1^{+/R284W}$ mice have behavioral and motor deficits

A timeline shows the order of a panel of tests performed in the same group of mice from 2.5 to 4 months of age (Fig. 3*a*). Thigmotaxis in normal mice is the tendency to stay along the periphery of an open field (Simon et al., 1994). $Nacc1^{+/R284W}$ males were the same as $Nacc1^{+/+}$ males in time spent in the center and periphery of the field, whereas $Nacc1^{+/R284W}$ females spent less time in the center and more time in the border than $Nacc1^{+/+}$ littermates (Fig. 3*b–d*), a possible sign of greater anxiety (Seibenhener and Wooten, 2015). However, $Nacc1^{+/R284W}$ mice were not different from $Nacc1^{+/+}$ in total distance traveled (Fig. 3*e*).

Mice were evaluated at 3 months for hindlimb clasping and paw curling (Fig. 3*f–j*). Male and female $Nacc1^{+/R284W}$ mice had significantly higher clasping scores and mean percentage of clasping than $Nacc1^{+/+}$ mice (Fig. 3*h*,*i*, respectively). To explore the onset age of this phenotype, we tested additional groups of younger (P14, F4–F5) and older (6-month-old, F2) mice from different cohorts. Male and female $Nacc1^{+/R284W}$ mice examined at P14 displayed no changes from $Nacc1^{+/+}$ in

Table 3. Mendelian offspring ratios from $Nacc1^{+/R284W} \times Nacc1^{+/R284W}$ breeding

	E17.5		P7		>P21	
	Male	Female	Male	Female	Male****	Female****
$Nacc1^{+/+}$	30 (27.5%)	23 (21.7%)	34 (31.8%)	33 (30.6%)	148 (32.2%)	151 (33.9%)
$Nacc1^{+/R284W}$	47 (43.1%)	53 (50%)	48 (44.9%)	47 (43.5%)	229 (49.9%)	213 (47.8%)
$Nacc1^{R284W/R284W}$	32 (29.4%)	30 (28.3%)	25 (23.4%)	28 (25.9%)	82 (17.9%)	82 (18.4%)
Total mice	109	106	107	108	459	446

p values are represented as follows: $*p < 0.05$, $**p < 0.01$, $***p < 0.001$, $****p < 0.0001$.

percent clasping (Fig. 3*g*), whereas *Nacc1*$^{+/R284W}$ females tested at age 6 months had a higher percent of clasping compared with age-matched *Nacc1*$^{+/+}$ females (Fig. 3*j*). Finally, homozygote mice bred beyond F6 generation exhibited hindlimb clasping. This included five of six F8 homozygotes at 3.2 months and 19/20 F10 homozygotes at 2.8–3 months old. Collectively, these data suggest that hindlimb clasping is a robust indicator of abnormality that develops after age P14. This phenotype has been reported in mouse models of other neurodevelopmental (Rett syndrome, Angelman's syndrome) and neurodegenerative disorders (Huntington's disease) and its presence signals dysfunction in multiple regions including the cortex, cerebellum, and caudate–putamen and the involvement of cerebello-cortical-reticular and cortico-striato-pallido-reticular pathways (Lalonde and Strazielle, 2011; Mandel-Brehm et al., 2015; Cruz et al., 2021).

Mice in the behavior cohort were next tested at 4 months for their ability to build nests. Scoring included both the percentage of nestlet used and a composite score for the nest built (Fig. 3*k–m*). The total amount of shredded nestlet used for building a nest was not different between *Nacc1*$^{+/R284W}$ and *Nacc1*$^{+/+}$ male and female mice (Fig. 3*l*). Both sexes of *Nacc1*$^{+/R284W}$ mice were able to build nests but *Nacc1*$^{+/R284W}$ females scored poorly compared with *Nacc1*$^{+/+}$ females (Fig. 3*k*,*m*), which is based on how much of the nestlet provided to them is used for building a nest and the quality of the built nest. These results indicated that the innate ability to build nests was impaired in females with the mutation.

Gait assessed at 4 months revealed a significantly shorter hindlimb stride length in female *Nacc1*$^{+/R284W}$ mice compared with that in *Nacc1*$^{+/+}$ mice (Fig. 3*n*,*p*). No difference between *Nacc1*$^{+/+}$ and *Nacc1*$^{+/R284W}$ mice was uncovered in forelimb stride length (Fig. 3*o*) or in stride width and diagonal stride width (Fig. 3*q–t*).

Altogether, results from the behavioral analysis showed that *Nacc1*$^{+/R284W}$ mice exhibited motor and behavioral impairments between 3 and 6 months of age. Females had more functional deficits than males in an open field measure of anxiety, in the incidence of clasping, in building nests, and in hindlimb stride length.

Performance on three other tests did not differ between genotypes (Fig. 4). The 2 d novel object recognition test, where two identical objects were presented on day 1 and then one was replaced by a novel object on day 2 (Fig. 4*a–d*), tests long-term memory recall in mice (≥24 h between tests 1 and 2; Taglialatela et al., 2009). *Nacc1*$^{+/+}$ and *Nacc1*$^{+/R284W}$ mice showed no preference for object placement during the training phase on day 1 (Fig. 4*b*,*c*). *Nacc1*$^{+/+}$ and *Nacc1*$^{+/R284W}$ mice also showed no change in their preference for the novel object on day 2 (Fig. 4*d*). The Y-maze assesses short-term spatial working memory (Kraeuter et al., 2019) through measuring correct and incorrect alternations (Fig. 4*e–g*). Performance in the Y-maze assessed as mean percent alteration between the three arms of the maze did not differ between genotypes (Fig. 4*f*) nor did the total number of arm entries (Fig. 4*g*). Finally, in tests of grip strength (Fig. 4*h–j*), female and male *Nacc1*$^{+/R284W}$ mice displayed no changes in normalized average (Fig. 4*i*) or normalized maximum grip strength (Fig. 4*j*) compared with their respective *Nacc1*$^{+/+}$ mice. These results suggest that memory impairment and grip strength in *Nacc1*$^{+/R284W}$ mice are not detected through these testing metrics.

Seizure-like behaviors appear in *Nacc1*$^{+/R284W}$ and *Nacc1*$^{R284W/R284W}$ mice at 7 months of age

Patients with *NACC1* 892C>T (pR298W) mutation have seizures and manifest abnormal EEG activity associated with myoclonic movements [Schoch et al. (2017), their supplementary patient report data]. Behavioral seizures, similar to those identified in the Racine seizure scale [Van Erum et al. (2019), their Fig. 1], were seen in some *Nacc1*$^{+/R284W}$ mice starting from age 7 months in the home cage either spontaneously or in response to handling, a sudden noise or light stimulus. The seizure-like behaviors included momentary or sustained freezing (Fig. 4*k*,*m*; Movies 1, 3, respectively), whisker twitching and head bobbing (Fig. 4*k*,*m*; Movies 1, 3, respectively), and wild jumping (Fig. 4*l*, Movie 2) and were seen in *Nacc1*$^{+/R284W}$ and *Nacc1*$^{R284W/R284W}$ mice and not in *Nacc1*$^{+/+}$ mice of similar ages. Seizures were seen in the home cages in later generations of mice. A homozygote mouse at F9 was noted to have a mild seizure in the cage at 4.5 months and a severe seizure at 5.5 months at which time the mouse was killed.

Nacc1$^{+/R284W}$ mice display cortical EEG epileptiform discharges during wakefulness and REM sleep and changes in spectral power distribution

We recorded cortical EEG and EMG activity in *Nacc1*$^{+/+}$ and *Nacc1*$^{+/R284W}$ mice at 3.5–4 months of age (Fig. 5*a*). *Nacc1*$^{+/+}$ littermates ($n = 11$, 6 males and 5 females) showed normal EEG activity (Fig. 5*b*,*g*). However, male and female *Nacc1*$^{+/R284W}$ mice ($n = 9$, 5 males and 4 females) displayed single or repetitive high-amplitude epileptiform discharges in the EEG during wakefulness and REM sleep (Fig. 5*c*,*h*). During wakefulness, epileptiform discharges coincided with low EMG activity and behavioral arrest (Fig. 5, Table 4, Movie 4). Characteristics of epileptiform discharges that occurred during wakefulness and REM sleep including mean number and duration of bursts measured in 48-, 24- and 1 h periods did not differ significantly between females and males (Table 4).

The spectral power distribution differed between periods of epileptiform discharges and those of normal wakefulness (Fig. 5*d–f*) and REM sleep (Fig. 5*i–k*) with percentage of total

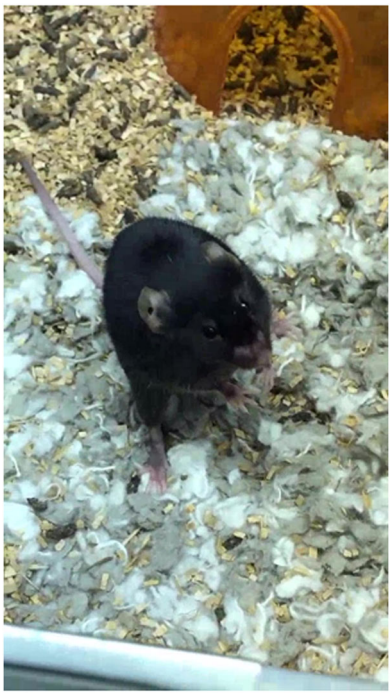

Movie 1. A 7-month-old female *Nacc1*$^{+/R284W}$ mouse is freezing in place on its hindlimbs for an extended period. [View online]

Movie 2. A 9-month-old female *Nacc1*$^{R284W/R284W}$ mouse displays erratic flipping and twitching for a short period of time. [View online]

Movie 3. A 9-month-old female *Nacc1*$^{R284W/R284W}$ mouse displays a seizure including limb and body twitching accompanied by repeated head twitching and tail stiffening. The second mouse in the cage can be seen having a milder seizure marked by tail stiffening. [View online]

power significantly reduced in the δ band (1–3 Hz) and increased in the β band (13–30 Hz) in males and females (Fig. 5*f*,*k*). Other significant changes in power spectra of the bursting periods occurred in males during wakefulness (γ, 55–60 Hz) and REM sleep (θ, 4.5–10 Hz, and σ, 1–3 Hz; Fig. 5*e*,*j*). Power spectra analysis of epileptiform discharges during wakefulness also showed rhythmic activity in the θ frequency range (4.5–10 Hz) in both genders and was associated with harmonics (at 16 and 24 Hz), characteristic of EEG hypersynchrony, a feature also described in middle-aged APP/PS1 mice (Jin et al., 2018). These data indicate that *Nacc1*$^{+/R284W}$ mice have frequent epileptiform discharges during wakefulness and REM sleep which are accompanied by changes in the spectral power distribution.

Analysis of the 24 h circadian period revealed that *Nacc1*$^{+/R284W}$ mice displayed an hourly percentage of wakefulness, SWS, and REM sleep similar to *Nacc1*$^{+/+}$ mice except female *Nacc1*$^{+/R284W}$ mice who spent a greater percent of time in SWS (Fig. 6*a*–*c*). With some exceptions described below, the spectral power distributions of the EEG during wake–sleep cycles were similar in female and male *Nacc1*$^{+/R284W}$ mice and *Nacc1*$^{+/+}$ mice (Fig. 6). During REM sleep, female *Nacc1*$^{+/R284W}$ mice ($n = 4$) had a deficit in the percentage of total power associated with θ band as compared with female *Nacc1*$^{+/+}$ mice ($n = 5$; Fig. 6*i*). This occurred during the period when mice are highly awake (19:00–22:00), indicating a deficit in hippocampal synchronization (Buzsaki, 2002). During SWS, male *Nacc1*$^{+/R284W}$ mice ($n = 5$) had significantly higher δ power as compared with male *Nacc1*$^{+/+}$ mice. This happened during the light period (10:00–13:00), when mice are mostly asleep, indicating a deeper SWS and more sleep pressure ($n = 5$; Fig. 6*n*). Altogether, these results indicated that *Nacc1*$^{+/R284W}$ mice had some changes in their sleep–wake cycles and associated spectral power distribution that differed in females and males.

δ waves contribute to the restorative aspects of SWS and to consolidate memories from synaptic maturation (Malkani and Zee, 2022). Enhanced (or increased) δ power occurs in human neurodevelopmental disorders including Rett syndrome (Ammanuel et al., 2015; Roche et al., 2019) and in a mouse model of Angelman's syndrome using the 129 mouse strain differing from the C57BL/6 strain (Sidorov et al., 2017) used in our study. δ power buildup was speculated to result from delayed synaptic maturation (Ammanuel et al., 2015) and may signal an imbalance in cortical inhibitory and excitatory activity. This imbalance could in turn affect cognitive function, prompting the idea for its potential as a biomarker to track disease progression and assess therapeutic interventions (Ostrowski et al., 2021).

The *Nacc1* R284W mutation elevates NACC1 protein levels and alters expression of its two isoforms in the brain

Western blot assays detecting NACC1 protein were performed with the polyclonal antibody from Abcam (#29047) which detects both long and short NACC1 isoforms and with polyclonal antibody from ThermoFisher (41656) which recognizes primarily the long isoform. It is worth noting again that only the long isoform encodes the R284W mutation (Fig. 1). NACC1 in lysates made from crude homogenates of mouse motor cortex of P7, P14, and 3- and 6-month-old mice expressed short and long isoforms that migrated to ∼57 and 67 kD, respectively, in *Nacc1*$^{+/+}$, *Nacc1*$^{+/R284W}$, and *Nacc1*$^{R284W/R284W}$ mice (Fig. 7*a*–*d*). There was a slightly faster migration of both isoforms in mice with the mutation (best seen in Fig. 7*b*,*c*). A significant rise in short NACC1 protein levels occurred in P7 and P14 *Nacc1*$^{+/R284W}$ and *Nacc1*$^{R284W/R284W}$ mice, and in short and long NACC1 protein levels in *Nacc1*$^{+/R284W}$ mice at 3 and 6 months compared with that in *Nacc1*$^{+/+}$ mice (Fig. 7*a*–*d*). These changes resulted in a net increase in total levels of

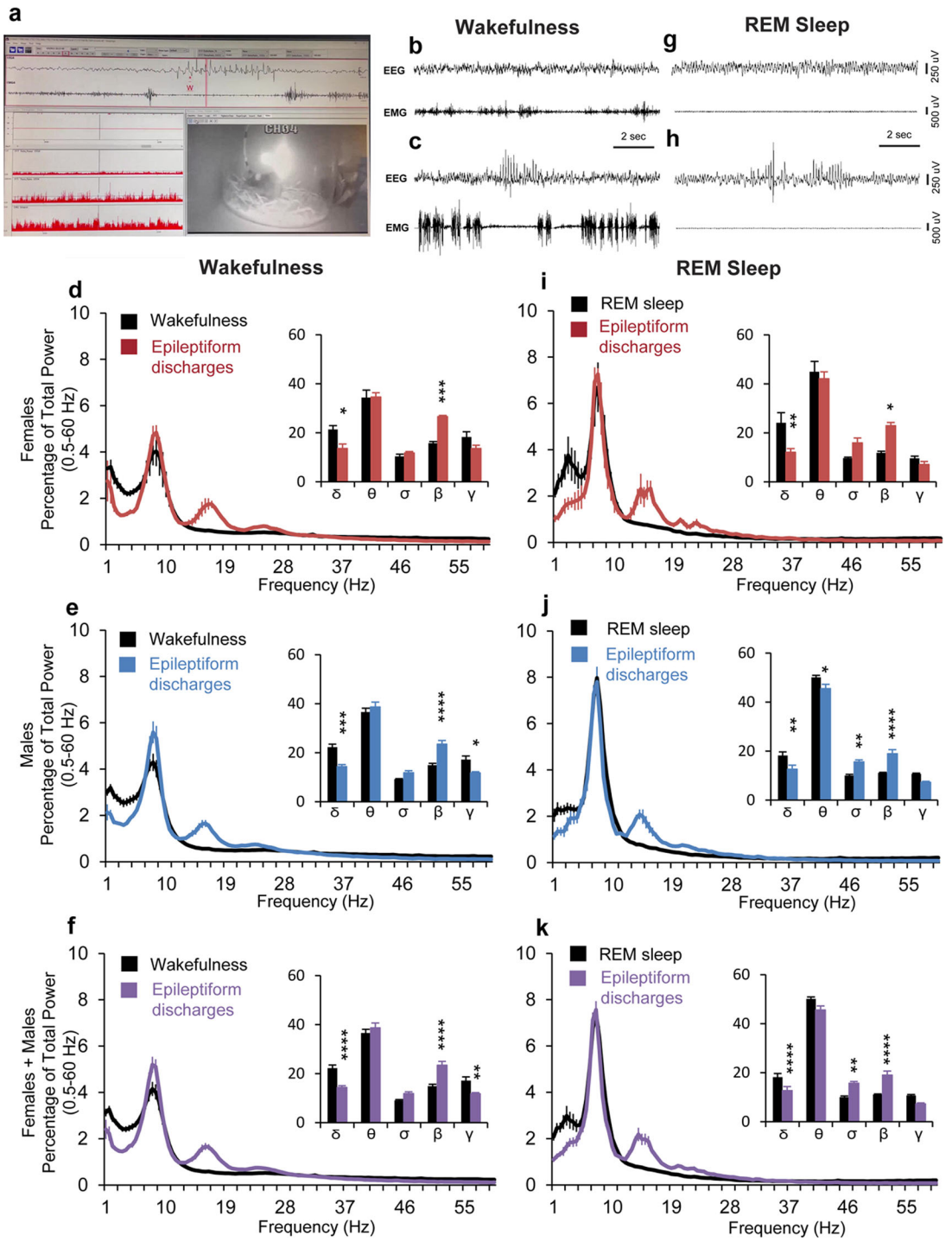

Figure 5. Epileptiform discharges in *Nacc1*$^{+/R284W}$ mice. ***a***, Still image (bottom right) from a video showing mouse in chamber tethered to a recording cable and traces of epileptiform discharges that coincided with low EMG activity and behavioral arrest. See Movie 4. ***b***, ***g***, Examples of normal EEG and EMG during wakefulness (***b***) and REM sleep (***g***) in the same *Nacc1*$^{+/+}$ mouse. Sample traces show epileptiform discharges during wakefulness (***c***) and during REM sleep (***h***) in the same *Nacc1*$^{+/R284W}$ mouse. Note the absence of muscle movement recorded by EMG that coincides with the EEG epileptiform discharges during wakefulness. ***d–f***, ***i–k***, Plots show the cortical EEG power spectral distribution expressed as a percent of total power for each frequency (0.5–60 Hz) during wakefulness (***d–f***) and during REM sleep (***i–k***) and for females (***d***,***i***), males (***e***,***j***), and combined females and males (***f***,***k***) respectively. The inserted bar graphs show cortical EEG power bands (δ, 0.5–4.5 Hz; θ, 4.5–10 Hz; σ, 10–15 Hz; β, 15–30 Hz; γ, 30–60 Hz). Episodes containing epileptiform discharges were analyzed over a 24 h period and compared with wakefulness cortical EEG power distribution during a circadian time of high waking drive (19:00–22:00; ***d–f***) or with REM sleep cortical EEG power distribution during a circadian time of high sleeping drive (10:00–13:00; ***i–k***), respectively. ***d–f***, ***i–k***, In female and male *Nacc1*$^{+/R284W}$ mice, the cortical EEG power distribution of the epileptiform discharges was significantly different from normal wakefulness or REM sleep. A two-way ANOVA followed by a post hoc Bonferroni's test, $n = 4$ male *Nacc1*$^{+/R284W}$ mice (red), $n = 5$ female *Nacc1*$^{+/R284W}$ mice (blue), $n = 9$ female + male *Nacc1*$^{+/R284W}$ mice (purple). For all panels, asterisks indicate p values with the following cutoffs: *$p < 0.05$, **$p < 0.01$, ***$p < 0.001$, ****$p < 0.0001$.

NACC1 in mutant mice. The increase in NACC1 in 3-month-old *Nacc1*$^{+/R284W}$ mice contrasted with a decline in FoxG1 (BF1), a protein present in adult pyramidal neurons (Fig. 7*c*).

To determine the subcellular compartment where the increase in NACC1 isoforms occurred, we examined nuclear and cytoplasmic fractions prepared from cortex of crude homogenates of

3-month-old mice. There were higher levels of long and short NACC1 in nuclear fractions and in short NACC1 in cytoplasmic fractions in *Nacc1*$^{+/R284W}$ mice compared with those in *Nacc1*$^{+/+}$ mice but no difference between genotypes in the relative distribution of nuclear and cytoplasmic NACC1 or its known interactors 20S proteasome and HDAC3 (Fig. 7*e–g*; Korutla et al., 2005; Shen et al., 2007). These results suggested that the mutation did not affect the nuclear cytoplasmic transport of NACC1 and some of its interactors. Where both sexes were examined at the same age (P7, 3 months, and 6 months; Fig. 7*a*,*c–f*), the increase in NACC1 in mutant mice favored a significant increase in females compared with that in males. In P7 and 3-month-old mice, the short isoform was increased in crude homogenates in both males and females (Fig. 7*a*,*c*), and in the nuclear–cytoplasmic fractionation, the short isoform was increased only in the cytoplasmic fraction of females (Fig. 7*f*). In 3-month-old mice, levels of NACC1 in cytoplasmic fractions were significantly elevated only in *Nacc1*$^{+/R284W}$ females (Fig. 7*f*). The long isoform was significantly increased in both males and females of 3-month-old mice (Fig. 7*c*). Finally, synaptosome fractions prepared from the cortex of 3-month-old mice also expressed the short and long isoforms, in all genotypes (Fig. 7*h*,*i*), lending support to the idea that WT and mutant NACC1 are positioned to directly influence synaptic function.

Altogether, these findings showed that the two NACC1 isoforms increased in an age-dependent manner with the short isoform rising earlier than the long isoform which harbors the mutation. The R284W mutation did not affect the relative nuclear cytoplasmic distribution of NACC1 or its localization within the synaptic compartment.

Next, we addressed if the increases in NACC1 protein levels in mutant mice involved changes in the levels of RNA encoding each NACC1 isoform. qPCR assays were performed with RNA prepared from the cortex of P14 and 6-month-old mice. Total *Nacc1* RNA levels, measured with a primer pair that detected both isoforms, did not differ between genotypes (Fig. 7*j*,*k*). The long isoform was diminished in the cortex of P14 *Nacc1*$^{R284W/R284W}$ compared with that of *Nacc1*$^{+/+}$ mice, whereas RNA specific to the short isoform increased at P14 in *Nacc1*$^{R284W/R284W}$ and at P14 and 6 months in *Nacc1*$^{+/R284W}$ mice (Fig. 7*k*). The net effect was approximately a fourfold decrease in the ratio of long/short isoform RNA levels in *Nacc1*$^{+/R284W}$ mice compared with that in *Nacc1*$^{+/+}$ mice at both ages without a change in total *Nacc1* RNA expression between genotypes. Potential contributors to augmented levels of NACC1 isoforms in *Nacc1*$^{+/R284W}$ mice with no net change in RNA levels include altered RNA stability, reduced clearance of the mutant protein, or enhanced sensitivity of anti-NACC1 antibodies to secondary structure or post-translational modification of mutant protein. For example, a putative site for

Table 4. *Nacc1*$^{+/R284W}$ mice: characteristics of epileptiform discharges and percent of wakefulness and REM sleep

EEG feature	Females ($n = 4$)	Males ($n = 5$)	Total ($n = 9$)
Epileptiform discharges			
Mean number in 48 h period.	396.0 ± 86.9	241.7 ± 56.2	365.8 ± 47.2
Mean number during wakefulness in 48 h period.	341.1 ± 87.4	267.3 ± 36.6	300.1 ± 42.6
Mean number during REM sleep in 48 h period.	54.9 ± 16.7	74.4 ± 28.9	65.7 ± 17.0
Number/hour of wakefulness	23.8 ± 5.5	21.1 ± 3.1	22.3 ± 2.8
Number/hour of REM sleep	62.8 ± 12.5	78.0 ± 26.0	71.2 ± 14.8
Ratio of single epileptiform discharges/repetitive epileptiform discharges (<5 s between spikes)			
During wakefulness	11.19 ± 5.40	9.68 ± 2.69	9.68 ± 2.69
During REM sleep	7.60 ± 1.12	6.98 ± 1.54	7.93 ± 0.77
Mean duration (in sec) during wakefulness in a 24 h period	1.45 ± 0.16	1.27 ± 0.05	1.41 ± 0.08
Mean duration (sec) during REM sleep in a 24 h period	2.27 ± 0.20	1.80 ± 0.23	2.06 ± 0.19
Wakefulness and REM sleep			
% wakefulness in a 24 h period	58.6 ± 1.8	52.5 ± 1.3	55.2 ± 1.5
% REM sleep in a 24 h period	3.4 ± 0.4	4.3 ± 0.3	3.9 ± 0.3

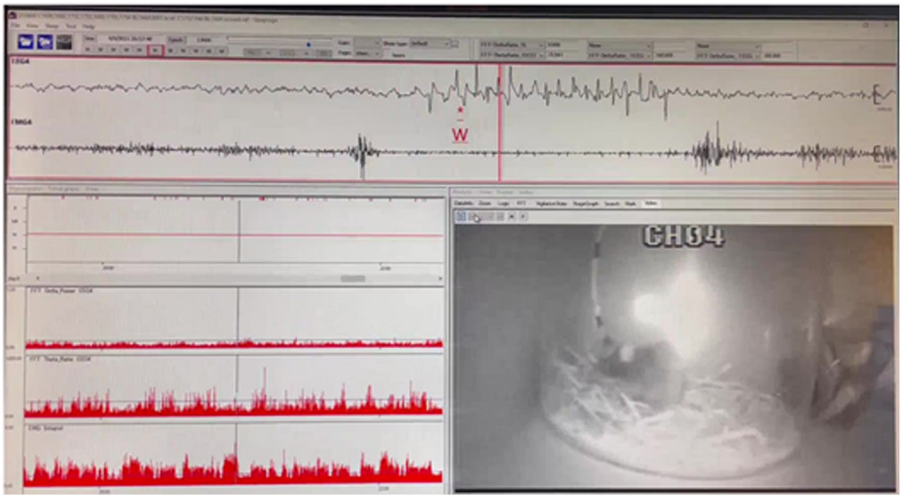

Movie 4. Representative recording of epileptiform discharge recorded in a *Nacc1*$^{+/R284W}$ mouse. Top trace shows a 10 s period of EEG activity with single trace of epileptiform discharge lasting about 3 s. The discharge coincides with reduced EMG activity seen in the trace below. Bursts in EMG are normal movements or spasms. The *Nacc1*$^{+/R284W}$ mouse being recorded is present in a transparent cylinder at lower right. The lower left box is a 3 h recording segment during wakefulness. The first window is the hypnogram, and the red line indicates wakefulness and vertical tick marks are spiking events. The second, third, and fourth panels monitor cortical EEG delta, theta, and the integrated EMG (marker for wakefulness), respectively, which are used for automatic scoring by the software. W and red traces are wakefulness. During the epileptiform discharge EMG activity is suspended and the mouse momentarily stops moving. [View online]

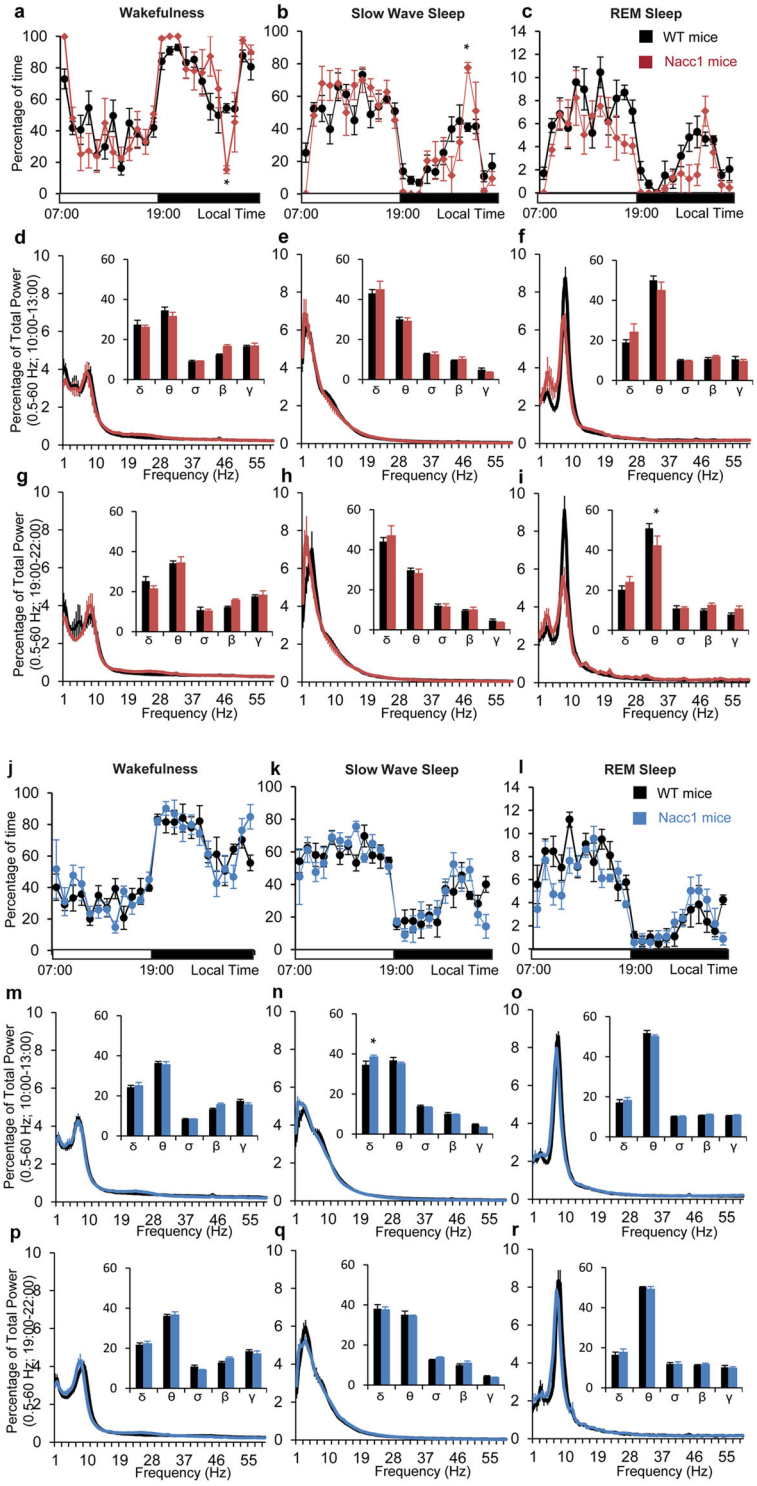

Figure 6. Sleep–wake phenotypes in female and male *Nacc1*$^{+/R284W}$ mice. ***a–c***, Wakefulness (***a***), SWS (***b***), and REM sleep (***c***) hourly percentage in female mice. ***d–i***, Cortical EEG power spectral distribution and bands (inserted histogram), expressed in percentage of total (0.5–60 Hz) power of wakefulness (***d***,***g***), SWS (***e***,***h***), and REM sleep (***f***,***i***), during a circadian time of high sleeping drive (10:00–13:00; ***d–f***) and during a circadian time of high waking drive (19:00–22:00; ***g–i***). δ, 0.5–4.5 Hz; θ, 4.5–10 Hz; σ, 10–15 Hz; β, 15–30 Hz; γ, 30–60 Hz. In ***i***, θ power is reduced in female *Nacc1*$^{+/R284W}$ mice (red, $n = 4$) compared with that in female littermate control (*Nacc1*$^{+/+}$, black, $n = 5$) mice. $^*p < 0.05$, two-way ANOVA followed by a post hoc Bonferroni's test. ***j–l***, Wakefulness (***j***), SWS (***k***), and REM sleep (***l***) hourly percentage in male mice. ***m–r***, Cortical EEG power spectral distribution and bands (inserted histogram), expressed in percentage of total (0.5–60 Hz) power of wakefulness (***m***,***p***), SWS (***n***,***q***), and REM sleep (***o***,***r***) during a circadian time of high sleeping drive (10:00–13:00; ***m–o***) and during a circadian time of high waking drive (19:00–22:00; ***p–r***). δ, 0.5–4.5 Hz; θ, 4.5–10 Hz; σ, 10–15 Hz; β, 15–30 Hz; γ, 30–60 Hz. Male *Nacc1*$^{+/R284W}$ mice (blue, $n = 5$) and male littermate wild-type (*Nacc1*$^{+/+}$, black, $n = 6$) mice. In *n*, ,δ power is increased in male *Nacc1*$^{+/R284W}$ mice $^*p < 0.05$, two-way ANOVA followed by a post hoc Bonferroni's test.

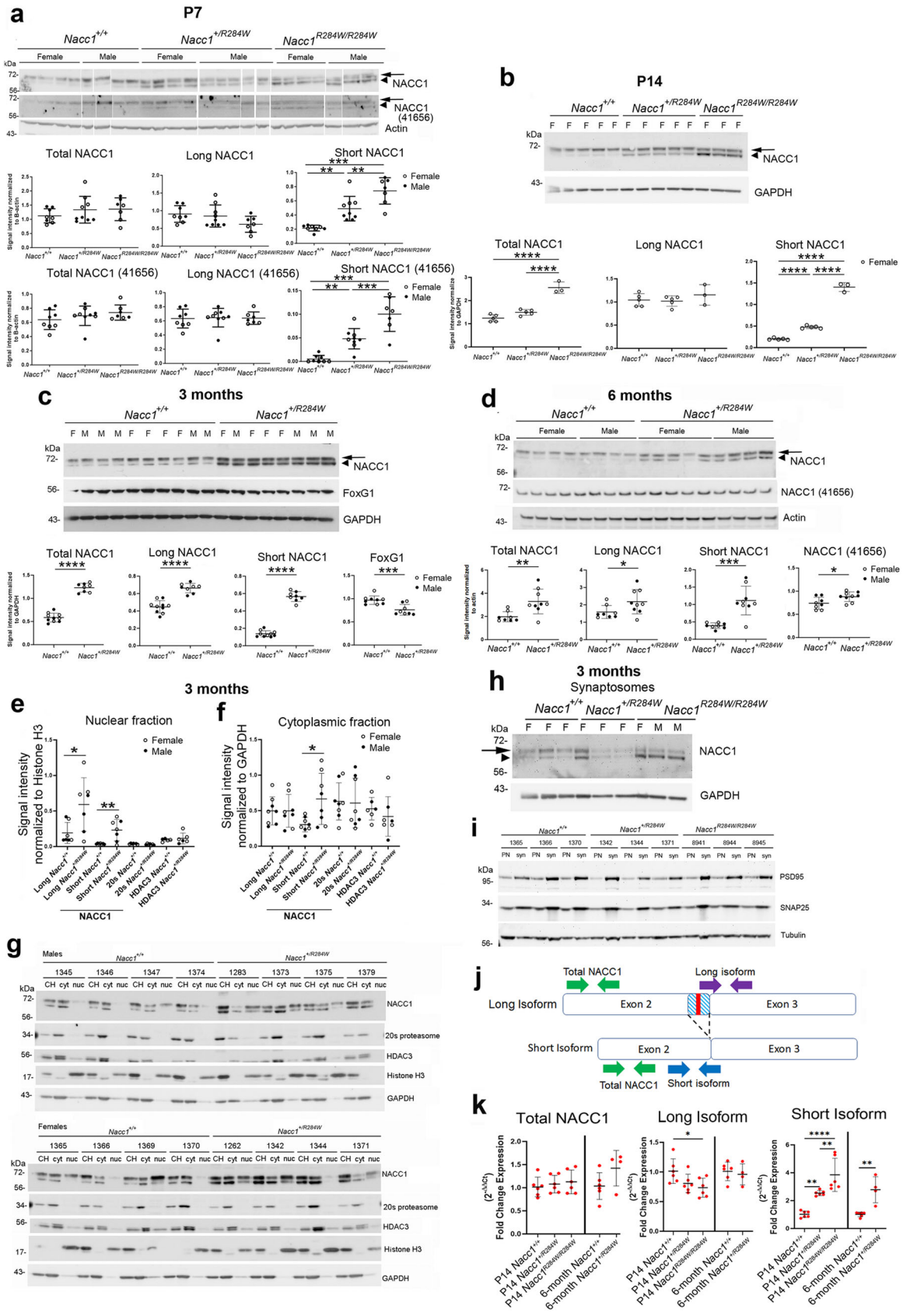

Figure 7. Increased NACC1 protein in the cortex of *Nacc1*$^{+/R284W}$ and *NACC1*$^{R284W/R284W}$ mice correlates with changes in RNA isoforms. ***a–d***, Shown are Western blots (WBs) of crude homogenates and quantitative analysis for P7 (***a***), P14 (***b***), 3-month-old (***c***), and 6-month-old (***d***) mice. Long (arrow) and short (arrowhead) NACC1 were detected in all age groups. Numbers on the left of WBs show migration of molecular mass markers in kDa. F and M indicate samples are from females or males, respectively. Graphs show mean protein levels ± SD relative to loading controls: GAPDH was used for P14 and 3 month data and actin for P7 and 6 month data. Females are represented as open circles and males closed circles. In the P7 mice [***a***, $n = 8$ *Nacc1*$^{+/+}$(4 female, 4 male), $n = 8$ *Nacc1*$^{+/R284W}$ (4 female, 4 male), $n = 8$ *Nacc1*$^{R284W/R284W}$ (4 female, 4 male)], there was a significant increase in the short isoform of NACC1 in *Nacc1*$^{+/R284W}$ and

SUMOylation in NACC1 at lysine residue K167 of human protein along with SUMO-interacting motifs mediates post-translational modification that may be important for NACC1 function in transcription and localization to nuclear bodies (Tatemichi et al., 2015). Also, Daniel et al. (2023) showed that levels of exogenously expressed WT mouse NACC1 (using sequence for the long isoform) was increased when coexpressed with SUMO.

NACC1 immunoreactivity is increased in neurons of *Nacc1*$^{+/R284W}$ mice

The results above showed that *Nacc1*$^{+/R284W}$ mice displayed behavioral and motor deficits, seizures, cortical EEG abnormalities, and increased levels of NACC1 isoforms in the cortex. To assess overall brain architecture, we stained sections from brains of *Nacc1*$^{+/+}$ and *Nacc1*$^{+/R284W}$ mice with cresyl violet and Luxol fast blue and cross-sectional areas of major gray and white matter regions were delineated (Fig. 8*a–f*). No regional differences were obtained between genotypes for gray and white matter except for the caudate–putamen which was slightly but significantly smaller in *Nacc1*$^{+/R284W}$ mice compared with *Nacc1*$^{+/+}$ mice (Fig. 8*e*). It is possible that the caudate–putamen in mutant mice has fewer projections from the motor cortex and other cortical areas resulting in its diminished size.

Next, we examined immunofluorescence labeling of NACC1 in the cortex using the same polyclonal antibody that detected long and short NACC1 isoforms (Abcam #29047) by Western blot shown in Figure 7. NACC1 localization was widespread in the brain and more intense in the neocortex of *Nacc1*$^{+/R284W}$ mice than that of *Nacc1*$^{+/+}$ mice (Fig. 9*a–d*). NACC1 colocalized with the nuclear-enriched neuronal protein NeuN (Rbfox3) in all cortical layers. There was a patchy distribution of nuclear NACC1 (Fig. 9*b*, inset) that was previously shown in neurons in vitro to correspond to nuclear speckles (aka SC35 domains; Hall et al., 2006; Shen et al., 2007). Quantification of NACC1 immunoreactivity in

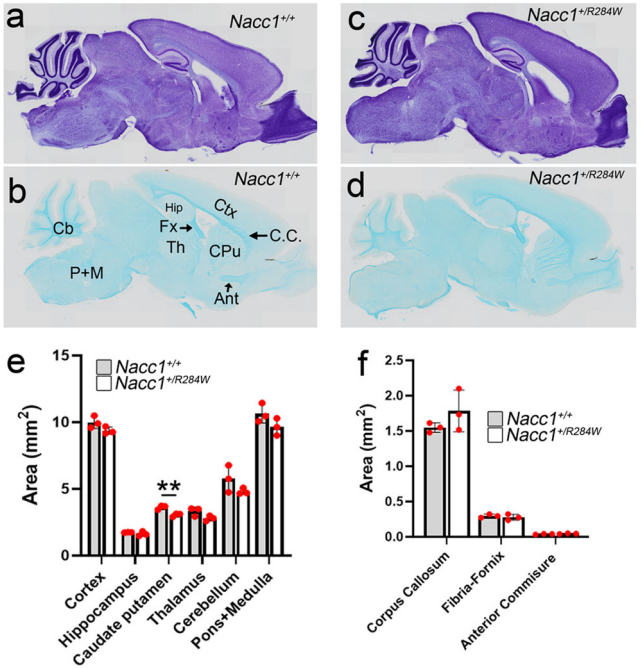

Figure 8. No gross morphological changes in *Nacc1*$^{+/R284W}$ mice. ***a–f***, Mouse brain sagittal sections stained with cresyl violet for gray matter and Luxol fast blue for white matter. ***a***, ***c***, Representative cresyl violet-stained sagittal sections of a *Nacc1*$^{+/+}$ mouse (***a***) and *Nacc1*$^{+/R284W}$ mouse (***c***). ***b***, ***d***, Representative Luxol fast blue-stained sagittal section of a *Nacc1*$^{+/+}$mouse (***b***) and a *Nacc1*$^{+/R284W}$ mouse (***d***). Brain regions quantified for differences in area are identified in ***b***. Acronyms (arrows point to white matter tracts quantified): Ctx, cortex; CPu, caudate–putamen; Hip, hippocampus; Th, thalamus; Cb, cerebellum; P+M, pons and medulla; C.C., corpus callosum; Fx, fornix; Ant, anterior commissure. ***e–f***, Quantification of area for gray and white matter using Luxol fast blue matched *Nacc1*$^{+/+}$ and *Nacc1*$^{+/R284W}$ images. ***e***, Area quantification of gray matter regions. Caudate–putamen showed a significantly reduced area in *Nacc1*$^{+/R284W}$ mice compared with *Nacc1*$^{+/+}$ mice (unpaired Student's *t* test, $p = 0.0072$, $t = 5.052$, df = 4). ***f***, Area quantification of white matter regions. No changes for matched images were identified.

←

Nacc1$^{R284W/R284W}$ mice compared with *Nacc1*$^{+/+}$ mice with NACC1 antibodies from Abcam (one-way ANOVA, $F = 23.62$, $p < 0.0001$, Tukey's multiple-comparisons test, $^{**}p < 0.01$, $^{****}p < 0.0001$, df = 21; males: one-way ANOVA, $F = 125.6$, $p < 0.0001$; females: one-way ANOVA, $F = 11.15$, $p = 0.0037$) and ThermoFisher 41656 (one-way ANOVA, $F = 28.95$, $p < 0.0001$, Tukey's multiple-comparisons test, $^{**}p < 0.01$, $^{****}p < 0.0001$, df = 21; males: one-way ANOVA, $F = 6.786$, $p = 0.0160$; females: one-way ANOVA, $F = 28.33$, $p = 0.0001$). P7 samples were run on the same gel before genotyping was complete and white line indicate movement of lanes to group genotypes together. In the P14 mice (***b***, $n = 5$ *Nacc1*$^{+/+}$, $n = 5$ *Nacc1*$^{+/R284W}$, $n = 3$ *Nacc1*$^{R284W/R284W}$), there was a significant increase in total NACC1 (one-way ANOVA, $F = 62.89$, $p < 0.0001$, Tukey's multiple-comparisons test, $p < 0.0001$, df = 10) and the short isoform of NACC1 (one-way ANOVA, $F = 534.1$, $p < 0.0001$, Tukey's multiple-comparisons test, $p < 0.0001$, df = 10) in the *Nacc1*$^{+/R284W}$ and *Nacc1*$^{R284W/R284W}$ mice compared with that in *Nacc1*$^{+/+}$ mice. In the 3-month-old mice [***c***, *Nacc1*$^{+/+}$ ($n = 10$, 5 female, 5 male) and *Nacc1*$^{+/R284W}$ ($n = 8$, 4 female, 4 male)], there was a significant increase in total NACC1 (unpaired *t* test, $p < 0.0001$, $t = 14.32$, df = 16; males: $p < 0.0001$, $t = 8.515$, df = 7; females: $p < 0.0001$, $t = 11.66$, df = 7), the long isoform of NACC1 (unpaired *t* test, $p < 0.0001$, $t = 7.106$, df = 16; males: $p < 0.0001$, $t = 14.87$, df = 7; females: $p < 0.0001$, $t = 11.83$, df = 7), and the short isoform of NACC1 (unpaired *t* test, $p < 0.0001$, $t = 19.66$, df = 16; males: $p = 0.0054$, $t = 3.967$, df = 7; females: $p = 0.0003$, $t = 6.558$, df = 7) and a decrease in FoxG1 (unpaired *t* test, $p = 0.0009$, $t = 4.108$, df = 15; males: $p = 0.0149$, $t = 3.206$, df = 7; females: $p = 0.0374$, $t = 2.662$, df = 6). In the 6-month-old mice [***d***, *Nacc1*$^{+/+}$ ($n = 8$, 4 female, 4 male) and *Nacc1*$^{+/R284W}$ ($n = 9$, 5 female, 4 male)], there was a significant increase in total NACC1 (unpaired *t* test, $p = 0.0053$, $t = 3.254$, df = 15; males: $p = 0.025$, $t = 2.968$, df = 6; females: $p = 0.1612$, $t = 1.567$, df = 7), the long isoform of NACC1 (unpaired *t* test, $p = 0.0479$, $t = 2.154$, df = 15; males: $p = 0.0866$, $t = 2.047$, df = 6; females: $p = 0.3907$, $t = 0.9149$, df = 7), and the short isoform of NACC1 (unpaired *t* test, $p = 0.0002$, $t = 4.860$, df = 15; males: $p = 0.0035$, $t = 4.659$, df = 6; females: $p = 0.041$, $t = 2.500$, df = 7) and an increase in NACC1 Thermo (unpaired *t* test, $p = 0.0253$, $t = 2.485$, df = 15; males: $p = 0.02393$, $t = 1.306$, df = 6, females: $p = 0.0267$, $t = 2.794$, df = 7). ***e***, ***f***, NACC1 distribution in subcellular fractions. Nuclear and cytoplasmic fractions were prepared from the cortex of 3-month-old mice. Graph in ***e*** shows signal intensities of the nuclear fraction [mean ± SD, *Nacc1*$^{+/+}$ ($n = 7$, 3 female, 4 male) and *Nacc1*$^{+/R284W}$ ($n = 7$, 4 female, 3 male)] normalized to GAPDH for levels of long (unpaired *t* test, $p = 0.0227$, $t = 2.613$, df = 12; males: $p = 0.1268$, $t = 1.830$, df = 5; females: $p = 0.1525$, $t = 1.687$, df = 5) and short (unpaired *t* test, $p = 0.0056$, $t = 3.368$, df = 12; males: $p = 0.0699$, $t = 2.298$, df = 5; females: $p = 0.0884$, $t = 2.112$, df = 5). Histone deacetylase 3 (HDAC3) and 20S proteasome levels were unchanged between groups. Graph in ***f*** shows signal intensity of the cytoplasmic fraction [mean ± SD, *Nacc1*$^{+/+}$ ($n = 8$, 4 female, 4 male) and *Nacc1*$^{+/R284W}$ ($n = 8$, 4 female, 4 male)] normalized to histone H3 with a significant increase in short NACC1 (unpaired *t* test, $p = 0.0161$, $t = 2.737$, df = 14; males: $p = 0.1273$, $t = 1.769$, df = 6; females: $p = 0.0481$, $t = 2.475$, df = 6) in the *Nacc1*$^{+/R284W}$ mice. ***g***, Western blot images from which data were obtained for graphs shown in ***e*** and ***f***. ***h***, NACC1 in synaptosome fractions. WB shows long and short NACC1 (at arrow and arrowhead, respectively) in synaptosomes of 3-month-old *Nacc1*$^{+/+}$, *Nacc1*$^{+/R284W}$, and *Nacc1*$^{R284W/R284W}$ mice. ***i***, Enrichment of pre- and postsynaptic markers, SNAP25 and PSD95, respectively, was confirmed in the synaptosome fractions. The numbers at the top of the blot in ***g*** and ***i*** identify each mouse. ***j***, ***k***, qRT-PCR analysis reveals altered expression of *Nacc1* isoforms in *Nacc1*$^{+/R284W}$ and *Nacc1*$^{R284W/R284W}$ mice. ***j***, Schematic shows the regions in *Nacc1* that generate the long and short isoforms and the position of the spliced isoform. The red line indicates where the mutation is found. The striped area in the long isoform highlights the region not found in the short isoform. The position of the primers used to generate total *Nacc1* are highlighted in green, the long isoform-specific primer in purple, and the short isoform-specific primer position in blue. ActB was the loading control in all qPCR analysis. ***k***, Bar graphs show fold change in expression of total, long, and short isoform *Nacc1* expression in P14 and 6-month-old mice. Statistics: A one-way ANOVA with Tukey's post hoc analysis in P14 samples, an unpaired Student's *t* test for long isoform, and a Mann–Whitney test for total NACC1 and short isoform. For all panels, $^{*}p < 0.05$, $^{**}p < 0.01$, $^{***}p < 0.001$, $^{****}p < 0.0001$.

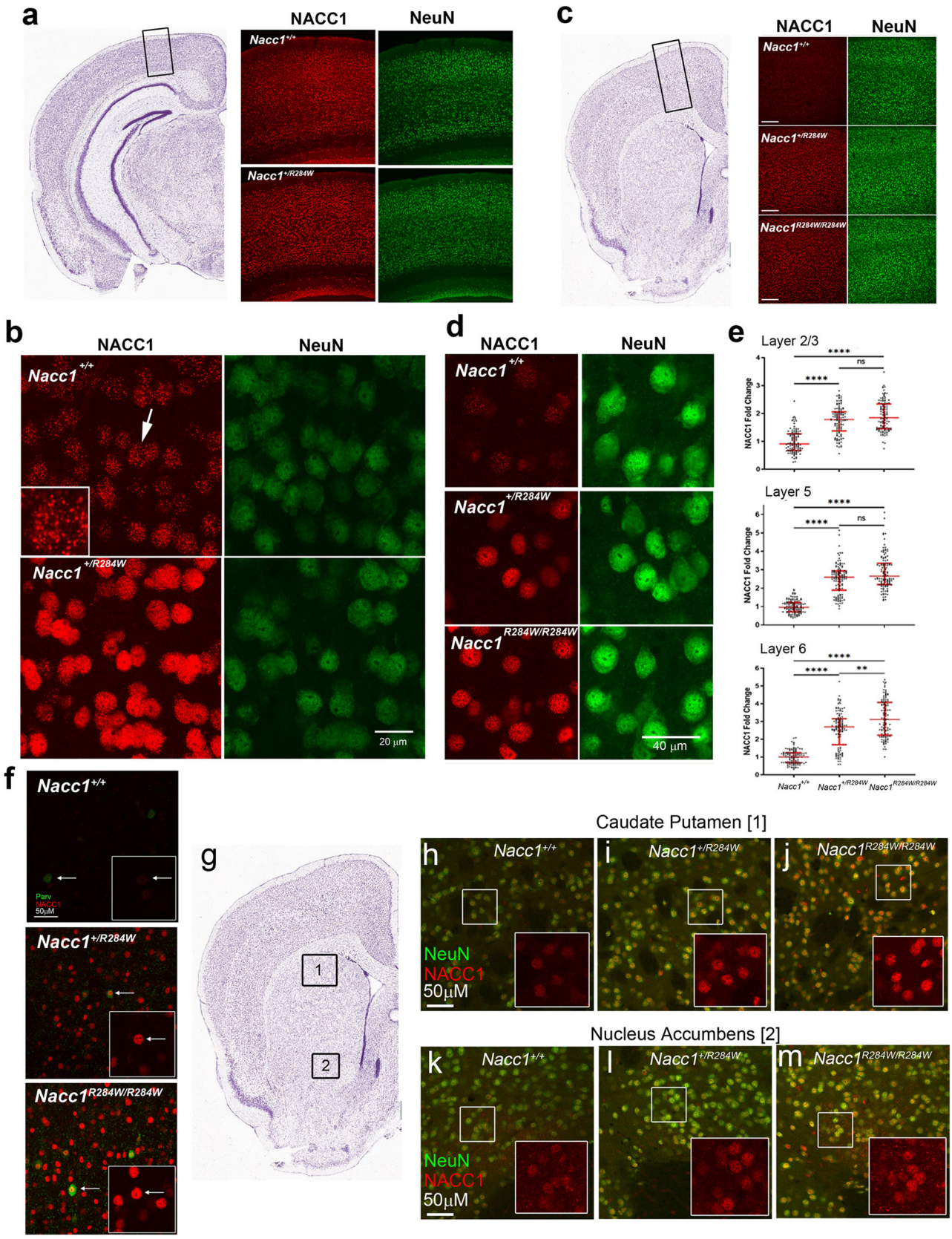

Figure 9. NACC1 immunofluorescence is increased in neuronal nuclei of *Nacc1*$^{+/R284W}$ and *Nacc1*$^{R284W/R284W}$ mice. Cresyl violet-stained images in ***a*** and ***c*** are mouse brain sections seen in the coronal plane adapted from the Allen Mouse Brain Atlas (http://mouse.brain-map.org). ***a***, The boxed area of the visual cortex indicates the brain region corresponding to the 10× image to the right. For the 10× immunofluorescence image, NACC1 was labeled with rhodamine red (red) and NeuN with AlexaFluor888 (green). NACC1 colabeling with NeuN appears uniform throughout all layers of the cortex and more intense in *Nacc1*$^{+/R284W}$ mice. ***b***, High magnification *z*-plane maximum projections from 30 μm sections imaged from panel ***a***. NACC1 can be seen as nuclear speckles (inset) in *Nacc1*$^{+/+}$ mice. In *Nacc1*$^{+/R284W}$ mice, the staining is much more intense. ***c***, The boxed area of the motor cortex indicates the brain region corresponding to the 10× image to the right. For the 10× immunofluorescence image, NACC1 was labeled with rhodamine red (red) and NeuN with AlexaFluor488 (green). NACC1 colabeling with NeuN appears uniform

the motor cortex revealed more intense staining in all cortical cell layers of $Nacc1^{+/R284W}$ compared with that of $Nacc1^{+/+}$ mice and more in layer VI of $Nacc1^{R284W/R284W}$ than that of $Nacc1^{+/R284W}$ mice (Fig. 9*d*,*e*). In addition to pyramidal cells, neocortical neurons positive for parvalbumin, a calcium ion binding protein that is a marker for fast spiking GABA inhibitory interneurons, also had elevated NACC1 immunoreactivity in $Nacc1^{+/R284W}$ and $Nacc1^{R284W/R284W}$ mice (Fig. 9*f*). Increased nuclear NACC1 also appeared in neurons in caudate–putamen (Fig. 9*h–j*) and nucleus accumbens (Fig. 9*k–m*) and CA1 region of the hippocampus (Fig. 10*c*) of $Nacc1^{+/R284W}$ and $Nacc1^{R284W/R284W}$ mice. Altogether, these data showed widespread neuronal nuclear localization of NACC1 in the brain of $Nacc1^{+/+}$ mice that was amplified by the NACC1 mutation in mutant mice and included cortical and hippocampal pyramidal neurons, which are glutamatergic excitatory cells, and parvalbumin-containing neurons which are GABAergic inhibitory neurons. The increased NACC1 immunoreactivity in the brain of mutant mice is consistent with results by Western blot using the same antibody from Abcam (Fig. 7) except that the two isoforms cannot be distinguished by immunohistochemical labeling as they are by Western blot.

In contrast to neurons, astrocytes in the corpus callosum and hippocampus identified by the presence of immunoreactive glial fibrillary acidic protein (GFAP) had similar levels of nuclear NACC1 labeling in $Nacc1^{+/+}$ and $Nacc1^{+/R284W}$ mice (Fig. 10*c*, arrowhead). However, a surprising finding was that NACC1 also colocalized with GFAP-positive glial processes and GFAP staining intensity in these processes was reduced in $Nacc1^{+/R284W}$ mice compared with that in $Nacc1^{+/+}$ mice (Fig. 10*c*, arrows). It was unclear if the processes were present in these glial cells or had been diminished by the mutation. Most astrocytes in the cortex that were identified with the specific marker calcium binding protein B (S100B) and oligodendroglia marked by oligodendrocyte transcription factor 2 (Olig2) had similarly low levels of nuclear NACC1 immunoreactivity in $Nacc1^{+/+}$ and $Nacc1^{+/R284W}$ mice (Fig. 10*d*), although a few cells in $Nacc1^{R284W/R284W}$ had more intense staining (Fig. 10*d*, yellow arrow). Microglia immunoreactive for ionized calcium binding adaptor molecule 1 (Iba1) did not show colocalized NACC1 in either the cell body or nucleus (Fig. 10*e*). In summary, NACC1 was detected at similarly low levels in most nuclei of astrocytes and oligodendroglia of $Nacc1^{+/+}$ and mutant mice and was absent in microglia.

RNA-seq and pathway analysis in the cortex of $Nacc1^{+/R284W}$ and $Nacc1^{R284W/R284W}$ mice reveal pervasive molecular changes at the transcriptome level

Due to the role of NACC1 as a transcriptional repressor and its prevalence in the nucleus of cortical neurons described above, we used RNA-seq to determine the impact of the *Nacc1R284W* mutation on gene regulation. RNA extraction and sequencing from samples of the motor cortex of P14 $Nacc1^{+/+}$, $Nacc1^{+/R284W}$, and $Nacc1^{R284W/R284W}$ mice were performed ($n = 3$ per genotype and sex) as detailed in Materials and Methods. This age was selected for the analysis due to the peak in synapse formation (Farhy-Tselnicker and Allen, 2018). *Nacc1* was not found to be differentially expressed by RNA sequencing in $Nacc1^{+/R284W}$ or $Nacc1^{R284W/R284W}$ mice. Consistent with changes in levels of *Nacc1* isoforms seen by qPCR (Fig. 7*j*,*k*), RNA sequencing showed the percentage of reads were reduced for long *Nacc1* isoform and increased for short *Nacc1* isoforms (Fig. 11*a–c*).

Volcano plots (Fig. 12*a*,*b*) display the number and distribution of DEGs with a nominal p value cutoff of <0.05 (complete list of DEGs can be found in Extended Data Fig. 12-1). These genes were used for pathway and GO analysis (discussed below; a complete list of GO, KEGG, and Reactome datasets can be found in Extended Data Figs. 12-2, 12-3, 12-4, respectively). More DEGs were identified in P14 $Nacc1^{R284W/R284W}$ mice (3,822 DEGs of 27,968 total transcripts) than those in $Nacc1^{+/R284W}$ (3,268 DEGs of 28,188 transcripts) mice and after applying the Bonferroni p-adjusted cutoff of $p < 0.05$ (1,355 for $Nacc1^{R284W/R284W}$ and 1,109 for $Nacc1^{+/R284W}$). Of these DEGs, 41 were significantly changed across the three genotypes supporting a mutant gene dose effect, and 38 of the 41 were downregulated (Tables 5, 6).

The top 10 upregulated and downregulated DEGs of $Nacc1^{+/R284W}$ and $Nacc1^{R284W/R284W}$ mice each compared with those of $Nacc1^{+/+}$ mice are depicted in Figure 12*a*,*b*. Common top 10 upregulated and downregulated genes between $Nacc1^{+/R284W}$ and $Nacc1^{R284W/R284W}$ are shown in Figure 12*c*,*d*, respectively. Common upregulated genes between $Nacc1^{+/R284W}$ and $Nacc1^{R284W/R284W}$ include *Kirrel2*, *Scel*, *Egfl6*, *Ephx1*, and *Pdzph1*. Among these Kirrel2 which encodes Kirrel-like nephrin family adhesion molecule 2 is important in cell adhesion and axon targeting (Vaddadi et al., 2019). Common downregulated genes between $Nacc1^{+/R284W}$ and $Nacc1^{R284W/R284W}$ include *Mfge8*, *Cbs*, *Lfng*, *Lcat*, *Cst3*, and *Entpd2*, all of which except *Lcat* were affected in a mutant gene dose-dependent manner. Two of these transcripts, *Mfge8*, which encodes lactadherin, and *Lcat* which encoded lecithin–cholesterol acetyltransferase, are important in glial function (Boddaert et al., 2007; Hirsch-Reinshagen et al., 2009).

Sex-specific DEG changes were compared for $Nacc1^{+/R284W}$ and $Nacc1^{R284W/R284W}$ mice ($n = 3$ mice per sex for each genotype). The number of DEGs unique to $Nacc1^{+/R284W}$ and $Nacc1^{R284W/R284W}$ females was greater than that in corresponding

←

throughout all layers of the cortex and more intense in $Nacc1^{+/R284W}$ and $Nacc1^{R284W/R284W}$ mice. ***d***, Representative images of NACC1 and NeuN staining used for quantification in ***e***. Images are single confocal *z*-planes of layer V of the motor cortex of 2-month-old mice used for quantitative data. NACC1 is labeled in rhodamine red (red) and NeuN with AlexaFluor488 (green). ***e***, Graphs show increased fold change of NACC1 intensity in motor cortex layers 2/3, 5, and 6 of P60 mice (each dot represents a nucleus; red lines depict median ± IQR, $n = 120$ cells per layer per mouse from 4 mice per genotype; statistics: layer 2/3, Kruskal–Wallis test with Dunn's multiple comparisons ($p < 0.0001$, Kruskal–Wallis statistic = 154.3); layer 5, Kruskal–Wallis test with Dunn's multiple comparisons ($p < 0.0001$, Kruskal–Wallis statistic = 219.8); layer 6, Kruskal–Wallis test with Dunn's multiple comparisons ($p < 0.0001$, Kruskal–Wallis statistic = 198.3)]. ***f***, Single confocal *z*-plane images of parvalbumin labeled neurons (arrow in white box) of the motor cortex of 2-month-old mice shows increased NACC1 staining intensity in $Nacc1^{+/R284W}$ and $Nacc1^{R284W/R284W}$ mice. NACC1 is labeled with rhodamine red and parvalbumin with AlexaFluor488. ***g***, A cresyl violet-stained representative image adapted from the Allen Mouse Brain Atlas (http://mouse.brain-map.org) representing the areas of caudate–putamen and nucleus accumbens (boxed regions 1 and 2, respectively) where images in ***h–m*** were taken. ***h–j***, NACC1 immunoreactivity in the caudate–putamen colocalizes with neuronal marker NeuN and appears increased in the $Nacc1^{+/R284W}$ and $Nacc1^{R284W/R284W}$ genotypes compared with that in $Nacc1^{+/+}$ genotypes. Insets show only the NACC1 channel. ***k–m***, NACC1 immunoreactivity in neurons of the nucleus accumbens are colocalized with NeuN. NACC1 immunoreactivity is increased in the $Nacc1^{+/R284W}$ and $Nacc1^{R284W/R284W}$ genotypes compared with that in $Nacc1^{+/+}$ genotypes. Insets show only the NACC1 channel. For all images shown, a single *z*-plane of the middle section of the tissue was used. Scale bars in the bottom left of ***h*** and ***k*** are 50 µm and apply to all images. NeuN was labeled with AlexaFluor488 and identifies differentiated neurons (green). NACC1 was labeled with rhodamine red (red). For all panels, $*p < 0.05$, $**p < 0.01$, $***p < 0.001$, $****p < 0.0001$.

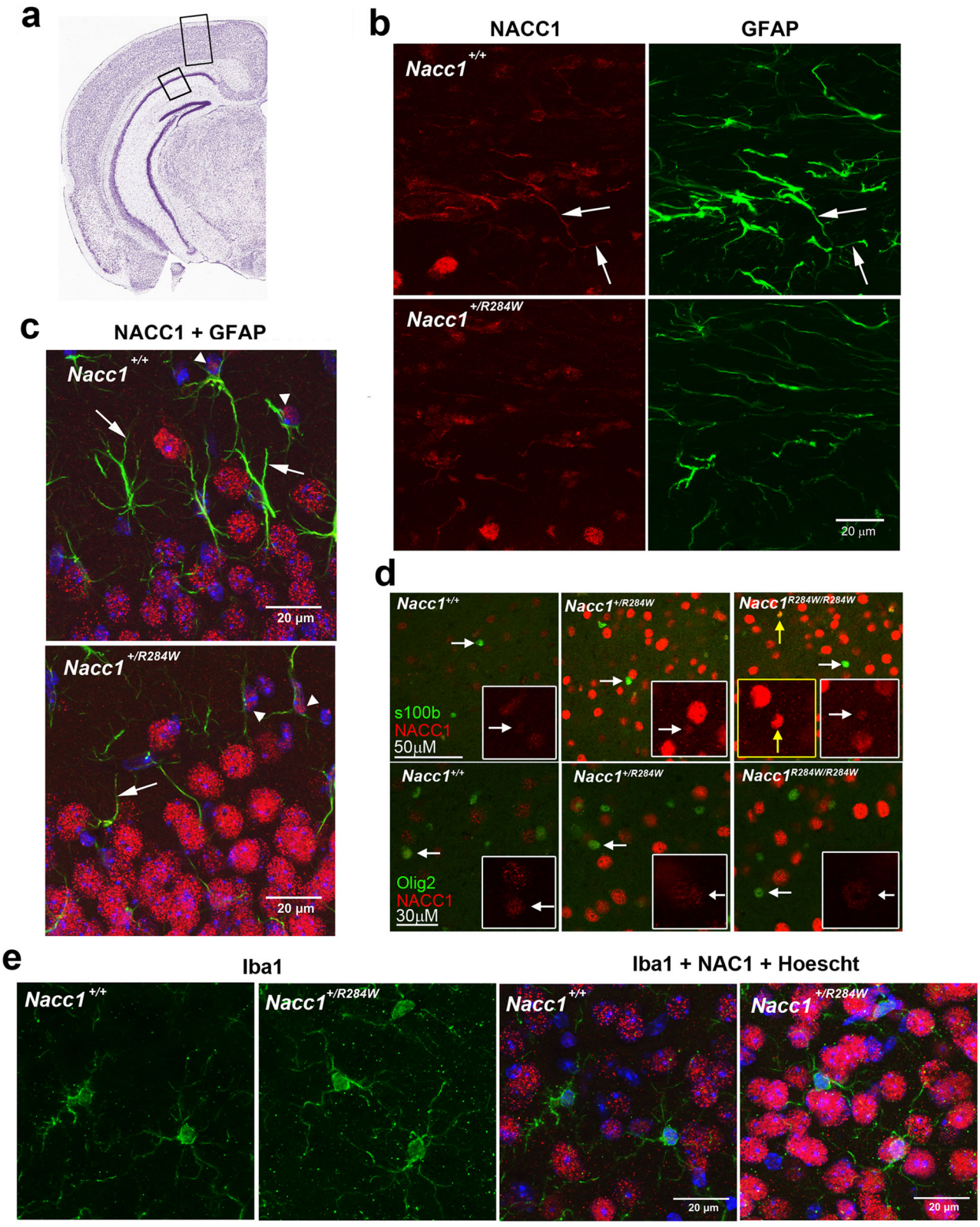

Figure 10. NACC1 immunoreactivity is detected in glial nuclei and some processes. ***a***, Cresyl violet-stained image of brain coronal section at level of the visual cortex adapted from the Allen Mouse Brain Atlas (http://mouse.brain-map.org). Boxed regions are where images were taken. Images in panels ***b*** and ***c*** are from the corpus callosum and hippocampus (CA1 region), respectively, of 3-month-old mice. Images in ***b*** and ***c*** were captured as maximum *z*-plane projections of 30 µm sections. NACC1 is labeled with rhodamine red and NeuN and GFAP with Bodipy (green). ***b***, In the corpus callosum, NACC1 and GFAP immunoreactivities are colocalized in astrocytic processes which are reduced in *Nacc1*$^{+/R284W}$ mice. ***c***, In the hippocampus CA1 region, GFAP-labeled astrocytic processes (arrows) that have NACC1 immunoreactive nuclei (arrowheads) are reduced in *Nacc1*$^{+/R284W}$ mice. ***d***, Immunofluorescent single *z*-plane confocal labeling of NACC1 in nuclei of glia, identified by the presence of S100b (mature astrocytes) or olig2 (mature oligodendrocytes) in *Nacc1*$^{+/+}$, *Nacc1*$^{+/R284W}$, and *Nacc1*$^{R284W/R284W}$ mice. Images were taken from 2-month-old mice from the motor cortex (s100b) or corpus callosum (Olig2) analogous to the brain region shown in Figure 9*c*. White arrowheads in boxes identify corresponding cells within the larger 40× image and the inset where only the NACC1 channel is visible in red. Immunofluorescent staining intensity for NACC1 is generally low. It should be noted in *Nacc1*$^{R284W/R284W}$ mice that there is a s100b-labeled cell (yellow box) that has more nuclear NACC1 immunofluorescence than in *Nacc1*$^{+/+}$. ***e***, NACC1 is not detected in Iba1-labeled microglia of *Nacc1*$^{+/+}$ and *Nacc1*$^{+/R284W}$ mice

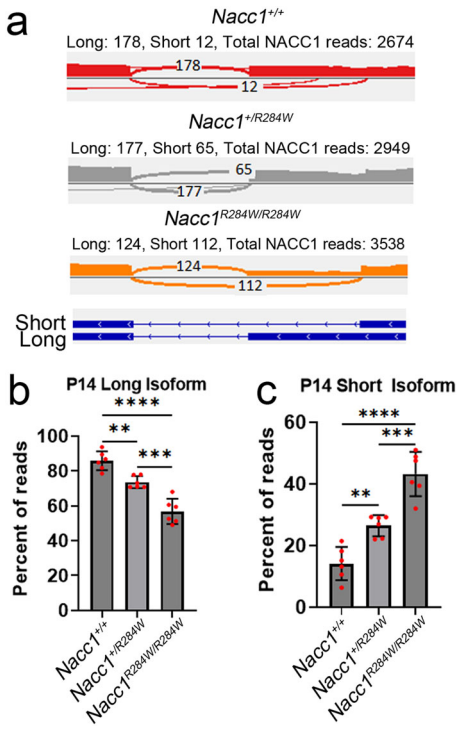

Figure 11. RNA-sequencing reads in P14 mice depict percent change in *Nacc1* isoform expression in a mutation dose response. ***a***, Representative female *Nacc1*$^{+/+}$ (red), *Nacc1*$^{+/R284W}$ (gray), and *Nacc1*$^{R284W/R284W}$ (orange) sashimi plots from P14 RNA-sequencing data. Below the plots is a map (blue) showing the corresponding splice sites in the *Nacc1* gene of the short and the long isoforms. Each sashimi plot shows the number of reads spanning both the long and the short isoform exon–exon junctions. On top of each plot are the long and short exon–exon reads as well as the total *Nacc1* reads for the gene. ***b***, ***c***, Percent of reads for long and short *Nacc1* isoforms in the cortex of P14 and 6-month-old *Nacc1*$^{+/+}$, *Nacc1*$^{+/R284W}$, and *Nacc1*$^{R284W/R284W}$ mice. Data shown as mean ± SDs as percentage of reads obtained from RNA-seq data for the isoform indicated compared with the total number of short and long isoform reads from the same mouse sample. ***b***, The long isoform for P14 mice shows a significant reduction in the percent of reads in a gene mutation dose-dependent manner (one-way ANOVA, $p < 0.0001$, $F = 41.39$, with Tukey's multiple comparison). ***c***, The short isoform shows an increase in the isoform's expression (one-way ANOVA, $p < 0.0001$, $F = 41.39$, with Tukey's multiple comparison). p values are represented as follows: *$p < 0.05$, **$p < 0.01$, ***$p < 0.001$, ****$p < 0.0001$.

males for upregulated transcripts (157 vs 6 in *Nacc1*$^{+/R284W}$ mice and 157 vs 120 in *Nacc1*$^{R284W/R284W}$ mice) and downregulated transcripts (82 vs 17 in *Nacc1*$^{+/R284W}$ mice and 182 vs 69 in *Nacc1*$^{R284W/R284W}$ mice). Although the top 3 DEGs for each sex and genotype group were different, three of the transcripts in *Nacc1*$^{+/R284W}$ mice encoded ribosomal proteins and included upregulated *Rps27* in males and downregulated *Rps27rt* in males and *Rps28* in females. Also noteworthy in *Nacc1*$^{R284W/R284W}$ females among the top 3 downregulated DEGs were *Mag* and *Mobp*, which encode proteins that are enriched in oligodendrocytes and are important in white matter formation.

GO term analysis revealed hundreds of enriched terms: upregulated genes in *Nacc1*$^{+/R284W}$ mice compared with those in *Nacc1*$^{+/+}$ mice enriched for 470 total terms [314 biological processes (BP), 68 cellular components (CC), and 88 molecular functions (MF)], while downregulated genes enriched for 136 total terms (85 BP, 43 CC, and 8 MF). Upregulated genes from *Nacc1*$^{R284W/R284W}$ mice compared with *Nacc1*$^{+/+}$ mice enriched for 406 total GO terms (295 BP, 46 CC, 65 MF), while downregulated genes enriched for 221 total terms (173 BP, 29 CC, and 19 MF). To determine high-confidence GO terms changed in both mutant genotypes, we compared the upregulated and downregulated GO terms between *Nacc1*$^{+/R284W}$ and *Nacc1*$^{R284W/R284W}$ mice (Fig. 12*e–h*). The top upregulated GO terms common to *Nacc1*$^{+/R284W}$ and *Nacc1*$^{R284W/R284W}$ mice were related to dendrite development, synaptic organization including the postsynaptic membrane and ion channel activity (Fig. 12*e*,*f*, respectively, black box). Common downregulated GO terms between *Nacc1*$^{+/R284W}$ and *Nacc1*$^{R284W/R284W}$ mice enrich for various metabolic functions, mitochondrial function, and structural constituents of the ribosome (Fig. 12*g*,*h*, respectively, black box). When all DEGs were included for the GO analysis (up and down), there was still enrichment for postsynaptic terms for *Nacc1*$^{+/R284W}$ and *Nacc1*$^{R284W/R284W}$ mice. GO analysis also highlighted DEGs encoding multiple types of potassium, calcium, and sodium channels, among them transcripts linked to seizure phenotypes (Table 7).

Sex-specific GO terms were compared for each genotype (n = 3 mice per sex for each genotype). In *Nacc1*$^{+/R284W}$ mice the top 3 unique terms enriched for upregulated genes in females were muscle tissue development (BP), presynaptic active zone (CC), and delayed rectifier potassium channel activity (MF) and in males were cell recognition (BP), adherens junctions (CC), and PDZ domain binding (MF). The top GO terms enriched for downregulated transcripts in *Nacc1*$^{+/R284W}$ females included mitochondrial ATP synthesis coupled electron transport chain (BP), inner mitochondrial membrane protein complex (CC), and rRNA binding (MF) whereas those in males were angiogenesis (BP), extracellular matrix (CC), and integrin binding (MF). In *Nacc1*$^{R284W/R284W}$ mice, unique GO terms with the most upregulated DEGs in females were positive regulation of synapse assembly (BP), filopodium (CC), and receptor binding (MF) and in males were positive regulation of catabolic process (BP), nuclear matrix (CC), and proximal promotor sequence specific DNA binding (MF). Unique GO terms with the most downregulated DEGs in females were ensheathment of neurons (BP), cell to cell junction (CC), and heparin binding (MF) whereas in males they were energy derivation by oxidation of organic compounds (BP), mitochondrial inner membrane (CC), and cell adhesion mediator activity (MF). These top GO term results suggested that both sexes of mutant mice had transcript changes that reflected diverse areas of dysfunction with females showing more synapse-related changes and males more adhesion and extracellular matrix alterations.

Remarkably, most DEGs encoding transcripts enriched in glia were downregulated in P14 *Nacc1*$^{+/R284W}$ mice and *Nacc1*$^{R284W/R284W}$ mice (Table 8). These included DEGs *Mfge8* and *Lcat* as noted above as well as *Gfap* and *Aldh1l1*. The latter two normally have their highest levels in mice at P14 when synapse formation and maturation are most active and glia play an important role (Farhy-Tselnicker and Allen, 2018). *Aldh1l1* also exhibited a gene mutation dose effect (Table 8) as did its protein product ALDH1L1, and both

←

at 3 months of age. Images show localization of immunoreactive Iba1, a marker for microglia in *Nacc1*$^{+/+}$ and *Nacc1*$^{+/R284W}$ mice in the primary visual cortex (V1). The first two images from the left show Iba1 alone (green) and the third and fourth images are from sections that were costained for Iba1 (green), NACC1 (red), and Hoechst dye (blue). No colocalization of Iba1 and NACC1 is evident.

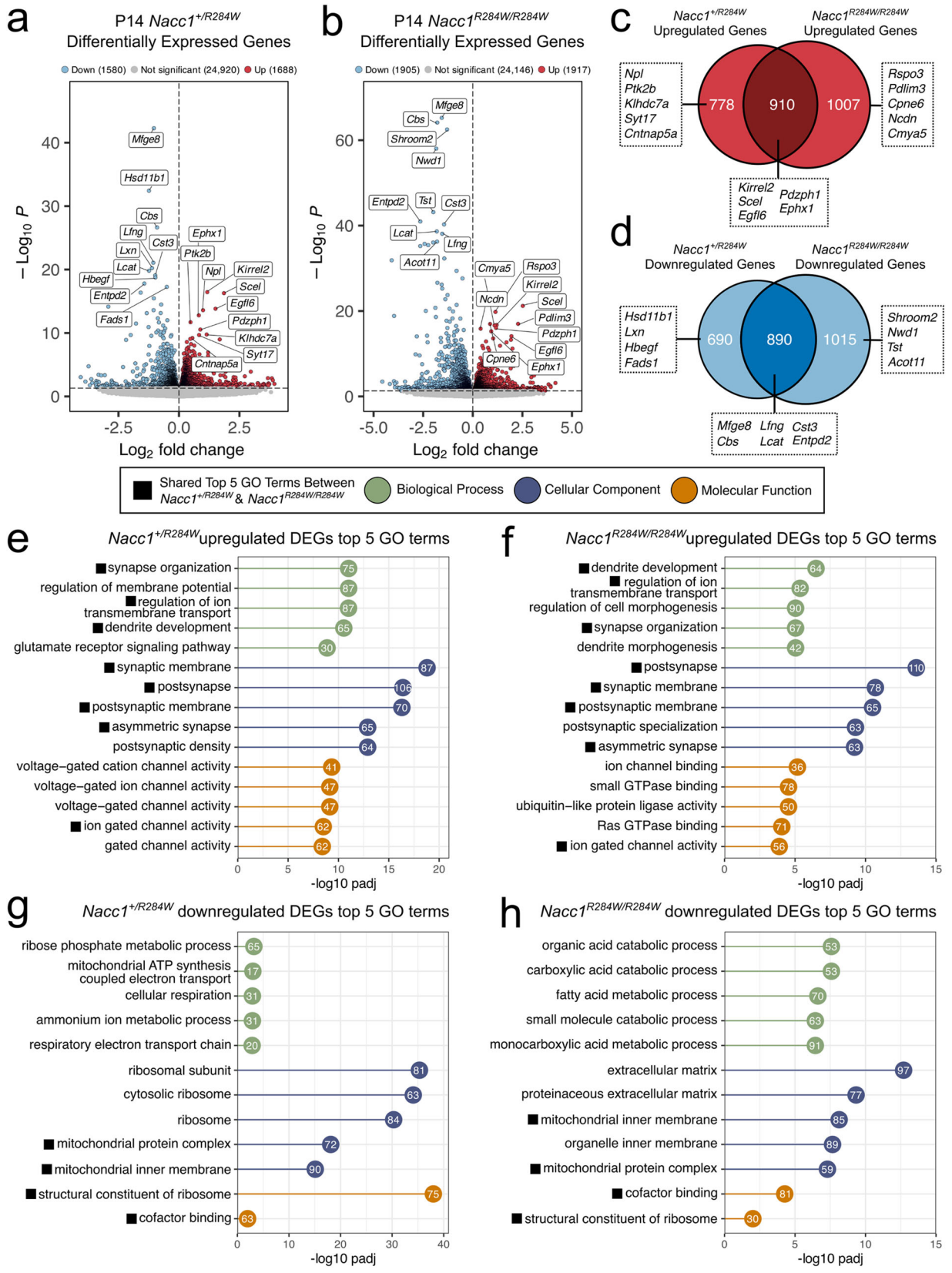

Figure 12. RNA-sequencing results show widespread changes in transcripts of P14 *Nacc1*$^{+/R284W}$ and *Nacc1*$^{R284W/R284W}$ mice. ***a***, ***b***, Punches from the motor cortex of 6 *Nacc1*$^{+/+}$, 6 *Nacc1*$^{+/R284W}$, and 6 *Nacc1*$^{R284W/R284W}$ (3 males and 3 females from each genotype) underwent RNA sequencing. Volcano plots of DEGs found in *Nacc1*$^{+/R284W}$ (***a***) and *Nacc1*$^{R284W/R284W}$ (***b***) mice compared with wild-type at the nominal *p* value cutoff of <0.05 are plotted. Blue indicates downregulated genes and red indicates upregulated genes. Nonsignificant genes are gray and the top 10 up- and downregulated genes are labeled. All DEGs can be found in Extended Data Fig. 12-1. ***c***, ***d***, Venn diagrams showing overlap between *Nacc1*$^{+/R284W}$ and *Nacc1*$^{R284W/R284W}$ DEGs at the nominal *p* value cutoff for upregulated genes, ***c***, and downregulated genes, ***d***. Top 10 genes identified from the volcano plot are depicted for each group they belong to. ***e–h***, GO terms derived from upregulated and downregulated nominal *p* value cutoff DEGs from *Nacc1*$^{+/R284W}$ and *Nacc1*$^{R284W/R284W}$ were compared and common GO terms extracted. The top 5 GO terms are shown from the biological process (BP, green), cellular component (CC, blue), and molecular function (MF, orange) categories which are

Table 5. RNA-seq at age P14: DEGs with a *Nacc1* gene mutation dose effect

Direction	Gene	Het vs WT Log2FC	Hz vs WT Log2FC
Up	Cpne6	0.3779	0.8712
Up	Cmya5	0.4794	1.0976
Up	Rspo3	0.6349	1.1417
Down	Mfge8	−1.0334	−1.5627
Down	Hsd11b1	−1.2384	−2.4300
Down	Cbs	−0.9055	−1.7908
Down	Lfng	−1.0613	−1.5423
Down	Cst3	−0.9780	−1.4459
Down	Entpd2	−1.4302	−2.6448
Down	Fads1	−0.5013	−0.8191
Down	Tst	−1.0365	−1.9885
Down	Mlc1	−0.7330	−1.2706
Down	Glul	−0.7559	−1.3829
Down	Slc14a1	−1.3306	−2.6458
Down	Gpld1	−0.8731	−1.5663
Down	Shroom2	−0.4797	−1.2961
Down	Slc25a34	−1.7742	−4.0872
Down	Nwd1	−0.7489	−1.8433
Down	Papss2	−0.9330	−2.2467
Down	Slc13a5	−0.7714	−1.8231
Down	Mmd2	−0.3374	−0.6274
Down	Slc6a11	−0.6697	−1.3223
Down	Daam2	−0.4393	−0.8164
Down	Emp2	−0.5326	−1.0213
Down	Acot11	−0.7435	−1.8007
Down	Btbd17	−0.6330	−1.7850
Down	Aldh1l1	−0.3839	−0.8264
Down	Ntsr1	−1.4318	−2.8215
Down	Plau	−0.7321	−1.8596
Down	Fgfr3	−0.4411	−0.8437
Down	Ntsr2	−0.3564	−1.1753
Down	Ncan	−0.2388	−0.5202
Down	Acss2	−0.2557	−0.4995
Down	Eva1a	−0.5703	−1.2577
Down	Pla2g7	−0.3304	−1.1589
Down	Slc27a1	−0.3039	−0.7036
Down	Kcnj16	−0.3431	−0.9310
Down	Gm11627	−0.7307	−2.2775
Down	Plpp3	−0.2378	−0.5741
Down	Ndrg2	−0.2792	−0.7184
Down	Luzp2	−0.1892	−0.5089

All genes shown in a are differentially expressed between *Nacc1*$^{+/R284W}$ and *Nacc1*$^{R284W/R284W}$ at a *p*-adjusted value smaller than 0.05.

Table 6. RNA-seq at age P14: percentage of total gene number with gene dose effect

	pAdj DEGs		Mutation dose DEGs		Percentage of pAdj DEGs	
	Up	Down			Up	Down
Nacc1$^{+/R284W}$	607	502	3	*Nacc1*$^{+/R284W}$	0.49%	0.60%
Nacc1$^{R284W/R284W}$	596	759	38	*Nacc1*$^{R284W/R284W}$	6.38%	5.01%

declined progressively in the cortex of P14 *Nacc1*$^{+/R284W}$ mice and *Nacc1*$^{R284W/R284W}$ mice (Fig. 13*a*,*b*).

Many transcripts encoding neuropeptides were also downregulated. These included the genes encoding cortistatin (*Cort*), somatostatin receptor 2 (*Sstr2*), neurotensin (*Nts*), neurotensin receptor 1 and 2 (*Ntsr1* and *Ntsr2*, respectively), and substance P (*Tac1*). In addition to their roles in synaptic function in the brain, some of these peptides play an important role in GI tract gut motility including cortistatin, neurotensin (and its receptor), and substance P (Yau, 1978; Gonzalez-Rey et al., 2006; Steinhoff et al., 2014; Ratner et al., 2016). GI dysfunction is a significant problem in patients with *NACC1*$^{+/R298W}$ (Schoch et al., 2017). NACC1 is localized to the epithelium of the GI tract (Yap et al., 2012) and could directly influence the action of these peptides.

To validate the results of the RNA-seq, qPCR was performed for four transcripts of interest that had a high fold change (*Gfap*, *Cort*, *Hsd1b11*, and *Kcne1l1*). Results showed that the four genes tested had reductions in fold change expression that correlated with those obtained by RNA-seq (Fig. 13*c*–*f*).

In summary, results of RNA-seq transcript and pathway analysis in *Nacc1*$^{+/R284W}$ and *Nacc1*$^{R284W/R284W}$ mice uncovered

Table 7. RNA-seq at age P14: DEGs that encode potassium, sodium, and calcium channels

	P14 *Nacc1*$^{+/R284W}$			P14 *Nacc1*$^{R284W/R284W}$		
Gene	log2FoldChange	*p* value	*p* adj	log2FoldChange	*p* value	*p* adj
Kcnj6	0.4443	0.0000	0.0016	0.2345	0.0963	0.3426
Kcnb1	0.3029	0.0002	0.0058	0.3124	0.0081	0.0803
Kcnb2	0.4295	0.0000	0.0010	0.2529	0.0198	0.1392
Kcnd2	0.2024	0.0015	0.0281	0.1487	0.0141	0.1146
Kcnf1	0.1612	0.0071	0.0769	0.2757	0.0007	0.0141
Kcng3[d]	0.8650	0.0014	0.0275	1.1024	0.0000	0.0003
Kcnh3	0.2028	0.0056	0.0653	0.2120	0.0020	0.0319
Kcnh5[d]	0.7981	0.0001	0.0036	0.6504	0.0004	0.0091
Kcnh7	0.3641	0.0002	0.0059	0.2179	0.0879	0.3286
Kcnip2	0.3030	0.0028	0.0420	0.2463	0.0341	0.1921
Kcnj12	0.3746	0.0003	0.0108	0.2179	0.0512	0.2428
Kcnj4[e]	0.1246	0.0493	0.2453	0.3230	0.0003	0.0082
Kcnj9	0.2015	0.0025	0.0388	0.1560	0.0093	0.0884
kcnk13	0.3962	0.0655	0.2835	0.7819	0.0024	0.0360
Kcnma1	0.2313	0.0001	0.0028	0.1772	0.0210	0.1447
Kcnq3[c,e]	0.3140	0.0000	0.0000	0.2189	0.0061	0.0677
kcnv1[d]	0.2678	0.0014	0.0275	0.1870	0.0011	0.0207
Kctd1[d]	0.3037	0.0017	0.0304	0.3898	0.0001	0.0021
Kctd16[a]	0.5523	0.0000	0.0008	0.3347	0.0168	0.1267
Kcne1l[d]	−1.1406	0.0000	0.0000	−1.4718	0.0000	0.0000
Kcnj16[b,d,e]	−0.3431	0.0020	0.0343	−0.9310	0.0000	0.0000
Kcnj5	−1.4522	0.0105	1.0000	−2.5535	0.0000	0.0000
Kcnq4	−0.2589	0.0221	0.1548	−0.3833	0.0003	0.0085
Kctd5[d,e]	−0.2880	0.0005	0.0140	−0.4083	0.0005	0.0111
SCN8A[e]	0.2002	0.0010	0.0219	0.1528	0.0710	0.2912
Cacna2d3[d,e]	0.3006	0.0000	0.0012	0.3381	0.0000	0.0001
Cacna2d1	0.3184	0.0000	0.0018	0.2301	0.0152	0.1197
Cacna1c	0.3039	0.0001	0.0041	0.2715	0.0144	0.1160
Cacna1i	0.2386	0.0003	0.0106	0.1275	0.1389	0.4168
Cacna1d	0.1835	0.0012	0.0250	0.1493	0.0445	0.2252

[a]Kctd gene family proteins lack transmembrane domains; Kctd16 may regulate membrane channel activity through modulation of specific GTPase; some are implicated in neurodevelopmental disorders (Teng et al., 2019).
[b]Kcnj16 encodes Kir5.1.
[c]Kcnq (Kv7) channels or M channels control excitability of pyramidal neurons for muscarinic receptors at perisomatic regions (Hu et al., 2007).
[d]Indicated genes where they are significantly dysregulated in both *Nacc1*$^{+/R284W}$ and *Nacc1*$^{R284W/R284W}$ mice.
[e]Associated with epilepsy/seizure disorders as described in results.

←

common to both mutant genotypes. Black boxes highlight common terms found in the top 5 common GO terms in both *Nacc1*$^{+/R284W}$ and *Nacc1*$^{R284W/R284W}$ results. Numbers found in the bubbles represent the number of DEG genes enriched in that pathway. All enriched GO terms, KEGG pathway, and Reactome pathways results can be found in Extended Data Figs.12-2, 12-3, and 12-4 respectively.

Table 8. RNA-seq at age P14: DEGs in glia of *Nacc1*$^{+/R284W}$ and *Nacc1*$^{R284W/R284W}$ mice

		P14 *Nacc1*$^{+/R284W}$			P14 *Nacc1*$^{R284W/R284W}$		
Gene dose response analysis[b]	Gene list	log2FoldChange	*p* value	*p* adj	log2FoldChange	*p* value	*p* adj
Astrocyte marker	GFAP[a]	−1.25537	2.45×10^{-7}	3.87×10^{-5}	−1.99449	8.89×10^{-37}	1.38×10^{-33}
Astrocyte marker	Aqp4	−0.01379	0.877687	0.954465	−0.31384	0.000469	0.010693
Astrocyte marker	Aldh1l1[a]	−0.38392	1.31×10^{-6}	0.000167	−0.82644	6.04×10^{-16}	2.15×10^{-13}
Commonly expressed astrocyte genes	Cst3[a]	−0.97802	8.21×10^{-20}	1.7×10^{-16}	−1.4459	5.18×10^{-41}	1.27×10^{-37}
Commonly expressed astrocyte genes	Cpe	0.08618	0.230878	0.53931	0.297343	0.002382	0.035805
Commonly expressed astrocyte genes	Dbi[a]	−0.6531	6.65×10^{-12}	3.45×10^{-9}	−0.78549	2.41×10^{-9}	2.94×10^{-7}
Commonly expressed astrocyte genes	Glul[a]	−0.75591	7.23×10^{-14}	5.15×10^{-11}	−1.38292	1.68×10^{-23}	1.25×10^{-20}
Commonly expressed astrocyte genes	Sparcl1[a]	−0.19677	0.000417	0.012203	−0.36885	5.74×10^{-9}	6.33×10^{-7}
Commonly expressed astrocyte genes	Scd2[a]	−0.24468	0.002513	0.039154	−0.34271	1.95×10^{-5}	0.000833
Commonly expressed astrocyte genes	Ndrg2[a]	−0.27916	0.002673	0.040316	−0.71841	1.6×10^{-10}	2.53×10^{-8}
Commonly expressed astrocyte genes	Clu[a]	−0.48136	1.73×10^{-6}	0.000214	−0.86054	1.94×10^{-10}	2.93×10^{-8}
Commonly expressed astrocyte genes	Slc1a2	−0.10088	0.148886	0.433144	−0.46958	4.01×10^{-6}	0.000211
Commonly expressed astrocyte genes	Mt3[a]	−0.24241	0.002636	0.040086	−0.40527	1.17×10^{-9}	1.54×10^{-7}
Transporters	Slc1a2	−0.10088	0.148886	0.433144	−0.46958	4.01×10^{-6}	0.000211
Transporters	slc6a11[a]	−0.66965	3.71×10^{-10}	1.22×10^{-7}	−1.32228	1.86×10^{-18}	9.08×10^{-16}
Transporters	slc16a1	−0.2946	0.000281	0.009367	−0.47471	0.027169	0.167925
Receptors	Itpr2	−0.14882	0.203788	0.50617	−0.4521	0.00034	0.00838
Receptors	Grm3	−0.05867	0.323467	0.632896	−0.41313	1.19×10^{-10}	1.94×10^{-8}
Receptors	Gabbr2	−0.06861	0.078965	0.313329	−0.1259	0.00234	0.035297
Synaptic structure	Sparcl1[a]	−0.19677	0.000417	0.012203	−0.36885	5.74×10^{-9}	6.33×10^{-7}
Synaptic structure	Thbs4	−2.12172	0.009343	0.091212	−2.70717	0.000268	0.006928
Synaptic function	Chrdl1	−0.2375	0.133602	0.410823	−0.63778	1.87×10^{-5}	0.000807
Synaptic function	Gpc4	0.163945	0.082357	0.320425	0.506663	2.44×10^{-7}	1.85×10^{-5}
Synaptic function	Sparc	0.197041	0.042718	0.228511	0.482951	1.3×10^{-5}	0.00059
Synaptic elimination	Mertk	−0.42661	0.00615	0.069604	−0.95236	5.75×10^{-15}	1.93×10^{-12}
Synaptic elimination	Tgfb2[a]	−0.5071	1.19×10^{-6}	0.000155	−0.47822	3.65×10^{-5}	0.001429
Synaptic elimination	Tgfb3	0.267168	0.001434	0.027658	0.248237	0.00676	0.072179
Synaptic elimination	C4b[a]	−0.72983	0.00055	0.014859	−1.72403	3.49×10^{-9}	4.09×10^{-7}
Synaptic elimination	Il33	−0.01925	0.878491	0.954982	−0.54202	0.000207	0.005675
Unique to P7	Itm2c	0.179772	0.051514	0.251763	0.381341	0.000188	0.005293
Unique to P7	Trim9[a]	0.157443	7.2×10^{-5}	0.003591	0.222099	0.000324	0.008087
Unique to P14	Agpat3	−0.12992	0.006296	0.070815	−0.25914	9×10^{-6}	0.000432
Unique to P14	abcd3	−0.10248	0.061803	0.27583	−0.21818	0.003188	0.043561
Unique to P28	gpm6b	−0.06972	0.075466	0.305567	−0.18778	0.002031	0.031731
Unique to P28	Igfbp5	−0.31802	0.015683	0.125118	−0.64801	6.89×10^{-12}	1.39×10^{-9}
P7 enriched	Cst3[a]	−0.97802	8.21×10^{-20}	1.7×10^{-16}	−1.4459	5.18×10^{-41}	1.27×10^{-37}
P7 enriched	Cpe	0.08618	0.230878	0.53931	0.297343	0.002382	0.035805
P7 enriched	Dbi[a]	−0.6531	6.65×10^{-12}	3.45×10^{-9}	−0.78549	2.41×10^{-9}	2.94 × 10
P7 enriched	Glul[a]	−0.75591	7.23×10^{-14}	5.15×10^{-11}	−1.38292	1.68×10^{-23}	1.25×10^{-20}
P7 enriched	Sparcl1[a]	−0.19677	0.000417	0.012203	−0.36885	5.74×10^{-9}	6.33×10^{-7}
P7 enriched	Scd2[a]	−0.24468	0.002513	0.039154	−0.34271	1.95×10^{-5}	0.000833
P7 enriched	Ndrg2[a]	−0.27916	0.002673	0.040316	−0.71841	1.6×10^{-10}	2.53×10^{-8}
P7 enriched	Clu[a]	−0.48136	1.73×10^{-6}	0.000214	−0.86054	1.94×10^{-10}	2.93×10^{-8}
P7 enriched	Mfge8[a]	−1.03339	5.19×10^{-43}	7.53×10^{-39}	−1.56265	5.7×10^{-66}	9.74×10^{-62}
P7 enriched	Fads2[a]	−0.48629	2.96×10^{-8}	6.81×10^{-6}	−0.83817	3.22×10^{-17}	1.34×10^{-14}
P7 enriched	Slc1a2	−0.10088	0.148886	0.433144	−0.46958	4.01×10^{-6}	0.000211
P7 enriched	Mt3[a]	−0.24241	0.002636	0.040086	−0.40527	1.17×10^{-9}	1.54×10^{-7}
P14 enriched	Cst3[a]	−0.97802	8.21×10^{-20}	1.7×10^{-16}	−1.4459	5.18×10^{-41}	1.27×10^{-37}
P14 enriched	Cpe	0.08618	0.230878	0.53931	0.297343	0.002382	0.035805
P14 enriched	Glul[a]	−0.75591	7.23×10^{-14}	5.15×10^{-11}	−1.38292	1.68×10^{-23}	1.25×10^{-20}
P14 enriched	Sparcl1[a]	−0.19677	0.000417	0.012203	−0.36885	5.74×10^{-9}	6.33×10^{-7}
P14 enriched	Ndrg2[a]	−0.27916	0.002673	0.040316	−0.71841	1.6×10^{-10}	2.53×10^{-8}
P14 enriched	Slc1a2	−0.10088	0.148886	0.433144	−0.46958	4.01×10^{-6}	0.000211
P14 enriched	Clu[a]	−0.48136	1.73×10^{-6}	0.000214	−0.86054	1.94×10^{-10}	2.93×10^{-8}
P14 enriched	Dbi[a]	−0.6531	6.65×10^{-12}	3.45×10^{-9}	−0.78549	2.41×10^{-9}	2.94×10^{-7}
P14 enriched	Scd2[a]	−0.24468	0.002513	0.039154	−0.34271	1.95×10^{-5}	0.000833
P14 enriched	Mt3[a]	−0.24241	0.002636	0.040086	−0.40527	1.17×10^{-9}	1.54×10^{-7}
P14 enriched	Ttyh1[a]	−0.20614	0.000833	0.019806	−0.48695	1.37×10^{-9}	1.75×10^{-7}
P14 enriched	Scg3	−0.18338	0.000431	0.012459	−0.17593	0.012611	0.106565
P28 enriched	Cst3[a]	−0.97802	8.21×10^{-20}	1.7×10^{-16}	−1.4459	5.18×10^{-41}	1.27×10^{-37}
P28 enriched	Cpe	0.08618	0.230878	0.53931	0.297343	0.002382	0.035805
P28 enriched	Glul[a]	−0.75591	7.23×10^{-14}	5.15×10^{-11}	−1.38292	1.68×10^{-23}	1.25×10^{-20}
P28 enriched	Clu[a]	−0.48136	1.73×10^{-6}	0.000214	−0.86054	1.94×10^{-10}	2.93×10^{-8}

(*Table continues.*)

Table 8. Continued

		P14 $Nacc1^{+/R284W}$			P14 $Nacc1^{R284W/R284W}$		
Gene dose response analysis[b]	Gene list	log2FoldChange	*p* value	*p* adj	log2FoldChange	*p* value	*p* adj
P28 enriched	Sparcl1[a]	−0.19677	0.000417	0.012203	−0.36885	5.74×10^{-9}	6.33×10^{-7}
P28 enriched	Ndrg2[a]	−0.27916	0.002673	0.040316	−0.71841	1.6×10^{-10}	2.53×10^{-8}
P28 enriched	Slc1a2	−0.10088	0.148886	0.433144	−0.46958	4.01×10^{-6}	0.000211
P28 enriched	Mt3[a]	−0.24241	0.002636	0.040086	−0.40527	1.17×10^{-9}	1.54×10^{-7}
P28 enriched	Scd2[a]	−0.24468	0.002513	0.039154	−0.34271	1.95×10^{-5}	0.000833
P28 enriched	Dbi[a]	−0.6531	6.65×10^{-12}	3.45×10^{-9}	−0.78549	2.41×10^{-9}	2.94×10^{-7}
P28 enriched	Gstm5[a]	−0.39802	3.01×10^{-6}	0.000334	−0.56164	7.16×10^{-10}	9.95×10^{-8}
P28 enriched	Mfge8[a]	−1.03339	5.19×10^{-43}	7.53×10^{-39}	−1.56265	5.7×10^{-66}	9.74×10^{-62}

[a]Indicated genes where they are significantly dysregulated in both $Nacc1^{+/R284W}$ and $Nacc1^{R284W/R284W}$ mice.
[b]Glia enriched genes at P14 reported in Farhy-Tselnicker et al. (2021), their Fig. 1*F*.

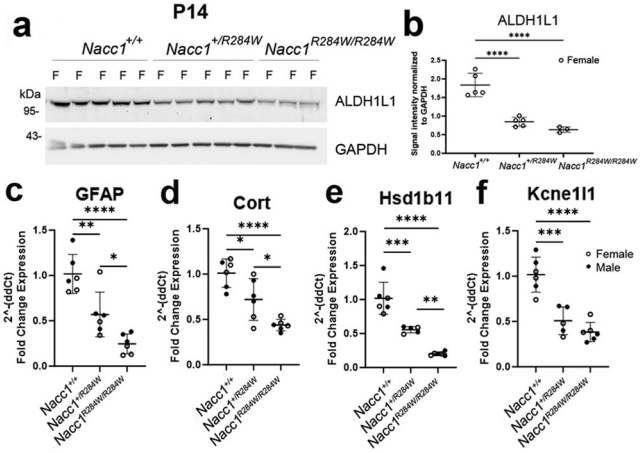

Figure 13. Levels of ALDH1L1 are reduced in the cortex of P14 $Nacc1^{+/R284W}$ mice. Western blots in ***a*** and quantitative data in ***b*** for ALDH1L1 levels in the motor cortex of P14 mice. The lysates are from the same brains of female mice used for RNA-seq analysis shown in Figure 12. Graphs in ***b*** depict mean ± SD, $n = 5$ $Nacc1^{+/+}$, 5 $Nacc1^{+/R284W}$, 3 $Nacc1^{R284W/R284W}$, one-way ANOVA ($p < 0.0001$, $F = 38.52$) with Tukey's multiple-comparisons test. ***c–f***, Reverse transcriptase quantitative PCR confirmation of RNA-sequencing DEGs. ***c***, *Gfap* expression was reduced in $Nacc1^{+/R284W}$ and $Nacc1^{R284W/R284W}$ mice (one-way ANOVA, $p < 0.0001$, $F = 22.59$ with Tukey's multiple-comparisons test). ***d***, *Cort* expression was down in $Nacc1^{+/R284W}$ and $Nacc1^{R284W/R284W}$ mice (one-way ANOVA, $p < 0.0001$, $F = 18.18$ with Tukey's multiple-comparisons test). ***e***, *Hsd11b1* expression was reduced in $Nacc1^{+/R284W}$ and $Nacc1^{R284W/R284W}$ mice (one-way ANOVA, $p < 0.0001$, $F = 48.23$ with Tukey's multiple-comparisons test). One female $Nacc1^{+/R284W}$ mouse was removed due to being an outlier (ROUT $Q = 1\%$). ***f***, *Kcne1l1* was down in $Nacc1^{+/R284W}$ and $Nacc1^{R284W/R284W}$ mice (one-way ANOVA, $p < 0.0001$, $F = 27.55$ with Tukey's multiple-comparisons test). One female $Nacc1^{+/R284W}$ mouse was removed due to being an outlier (ROUT $Q = 1\%$). All graphs show mean ± SD. Females are represented as open circles and males closed circles. *p* values are represented as follows: *$p < 0.05$, **$p < 0.01$, ***$p < 0.001$, ****$p < 0.0001$.

altered transcriptomes that implicate dysregulation of distinct cellular functions including neurotransmission. These molecular changes likely contribute to phenotypes displayed in $Nacc1^{+/R284W}$ mice including behavioral and motor deficits, behavioral seizures, and aberrant cortical EEG activity.

The cortex of $Nacc1^{+/R284W}$ mice have altered levels of proteins that function at synapses but no change in synaptic density

RNA-seq and pathway analysis described above suggested the *Nacc1* R>W mutation altered synaptic connectivity. In support of this idea, Western blots of crude homogenates from the cortex of $Nacc1^{+/R284W}$ showed significant changes in levels of synaptic proteins examined at P14, 3 months, and 6 months. At P14, where only lysates from females were examined, altered levels were detected in the vesicle membrane proteins synaptophysin and VAMP2, the presynaptic protein SNAP25, and in homozygotes the receptor GABRb1 (GABA type A receptor subunit; Fig. 14*a*). The transcripts encoding two of these proteins, VAMP2 and synaptophysin, were not differentially expressed based on results from RNA-seq performed in the same mice indicating the protein changes were post-translational. Older mice also had synaptic protein changes. Males at 3 months and females at 6 months had a reduction in Prosapip1 (Fig. 14*b*,*c*), a scaffold protein enriched in the postsynaptic density of dendritic spines (Wendholt et al., 2006; Reim et al., 2016). Also in 6-month-old mutant mice presynaptic SNAP25 was significantly changed in males and the postsynaptic protein Homer in females (Fig. 14*c*). These findings support the idea that protein changes exist pre- and postsynaptically in $Nacc1^{+/R284W}$ mice and depend on age and gender.

Finally, we looked at the density of synapses in cortex neuropil of 3-month-old $Nacc1^{+/+}$ and $Nacc1^{+/R284W}$ mice and observed axospinous and axodendritic synapses in both genotypes (Fig. 14*d*,*e*) and no significant difference in the number of synapses or total or average length of synaptic contacts between genotypes (Fig. 14*f–h*). Thus, despite evidence for changes in transcripts and proteins that implicate synaptic impairment in $Nacc1^{+/R284W}$, synaptic architecture at the ultrastructural level in 3-month-old mice was intact.

Summary of results

In all, the comprehensive description provided above shows that $Nacc1^{+/R284W}$ mice exhibit multiple phenotypes in postnatal and adult life at the behavioral, electrophysiological, and molecular level. Some phenotypes were affected by age, sex, and mutant gene dose. There are robust readouts such as hindlimb clasping, epileptiform discharges, and changes in brain levels of Nacc1 transcript, protein, and localization, as well as other transcripts and proteins, that will be useful as quantifiable endpoints for evaluating underlying mechanisms of neurodevelopmental disease and therapeutic interventions.

Discussion

Individuals with the $NACC1^{+/R298W}$ mutation have profound neurodevelopmental impairment usually identified in the first year of life. They suffer cortical seizures, GI distress, a failure to thrive, motor and behavioral deficits, and bouts of intense agitation (Schoch et al., 2017, 2023). How this de novo point mutation causes disease is unknown. The first model of $Nacc1^{+/R284W}$ in mice described here exhibit altered motor, behavioral, and electrophysiological changes, along with an array of transcriptional

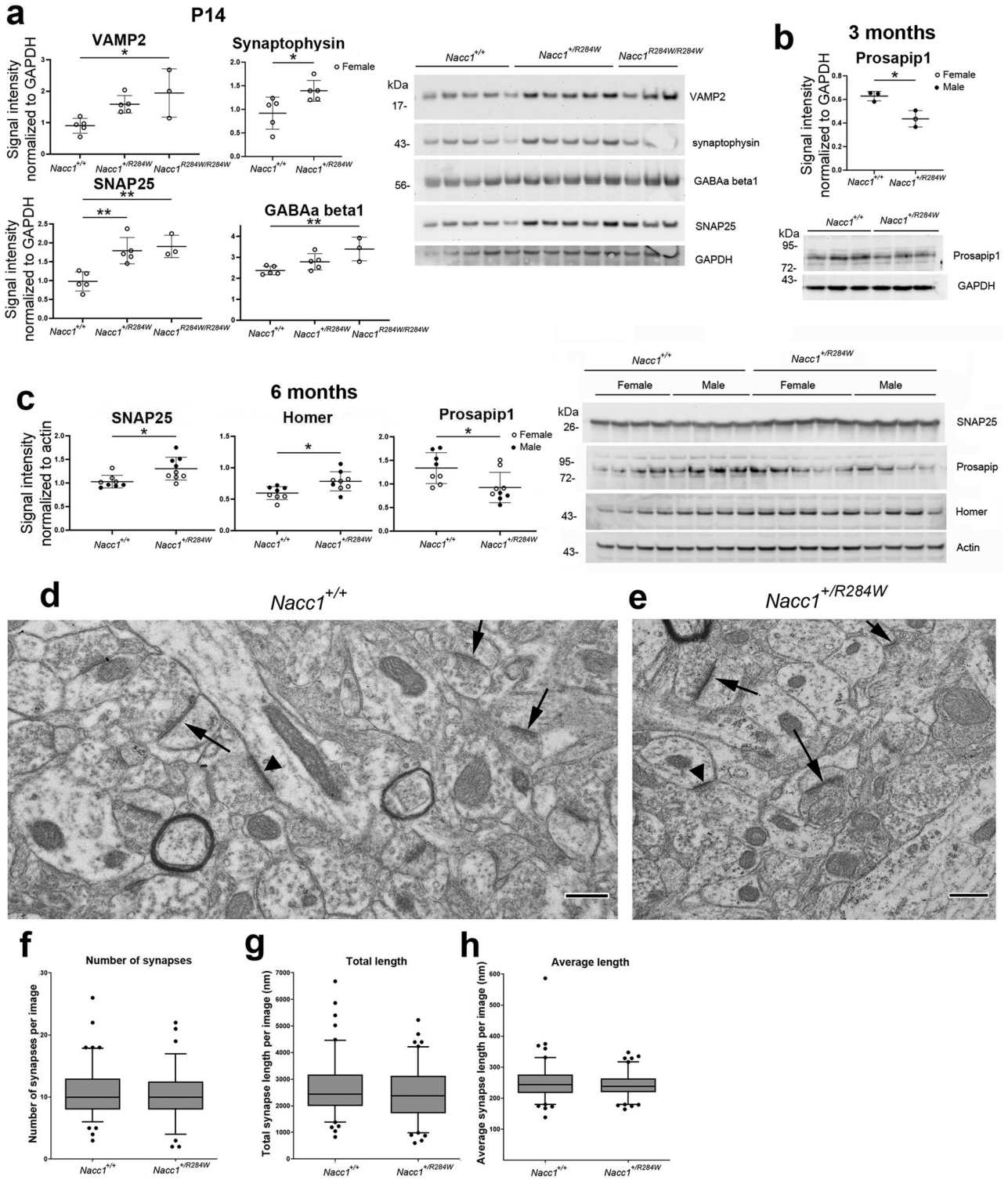

Figure 14. *Nacc1*$^{+/R284W}$ mice have changes in levels of synaptic proteins but normal neuropil ultrastructure. ***a–c***, Western blots of synaptic proteins detected in the cortex of crude homogenates from P14 mice [*Nacc1*$^{+/+}$ ($n = 5$ females), *Nacc1*$^{+/R284W}$ ($n = 5$ females), and *Nacc1*$^{R284W/R284W}$ ($n = 3$ females)], 3-month-old mice [*Nacc1*$^{+/+}$ ($n = 3$ males) and *Nacc1*$^{+/R284W}$ ($n = 2$ males, 1 female)], and 6-month-old mice [*Nacc1*$^{+/+}$ ($n = 8$, 4 males, 4 females) and *Nacc1*$^{+/R284W}$ ($n = 9$, 4 males, 5 females)]. Graphs show means and SDs for signal intensity normalized to GAPDH in ***a*** and ***b*** and to actin in ***c***. Females are represented as open circles and males closed circles. In the P14 mice, there was a significant increase in VAMP1 (one-way ANOVA, $p = 0.0144$, $F = 6.683$ with Tukey's multiple-comparisons test $^*p = 0.0159$), synaptophysin (unpaired t test, $^*p = 0.0308$, $t = 2.617$, df = 8), SNAP25 (one-way ANOVA, $p = 0.002$, $F = 12.41$ with Tukey's multiple-comparisons test, *Nacc1*$^{+/+}$ vs *Nacc1*$^{+/R284W}$ $^{**}p = 0.0044$, *Nacc1*$^{+/+}$ vs *Nacc1*$^{R284W/R284W}$ $^{**}p = 0.0048$), and GABAa beta1 (one-way ANOVA, $p = 0.0127$, $F = 6.964$ with Tukey's multiple-comparisons test $^*p = 0.01$) in the *Nacc1*$^{+/R284W}$ or *Nacc1*$^{R284W/R284W}$ mice compared with that in *Nacc1*$^{+/+}$ mice. In the 3-month-old mice (***b***), there was a significant decrease in Prosapip1 in the *Nacc1*$^{+/R284W}$ compared with that in *Nacc1*$^{+/+}$ mice (unpaired t test, $^*p = 0.0144$, $t = 4.137$, df = 4). In the 6-month-old mice (***c***), there was a significant increase in Homer (unpaired t test, $^*p = 0.0106$, $t = 2.919$, df = 15; males: $p = 0.2898$, $t = 1.161$, df = 6; females: $p = 0.001$, $t = 5.407$, df = 7) and SNAP25 (unpaired t test, $^*p = 0.0117$, $t = 2.868$, df = 15; males: $p = 0.0004$, $t = 6.952$, df = 6; females: $p = 0.8844$, $t = 0.1508$, df = 7) and a significant decrease in Prosapip1 (unpaired t test, $^*p = 0.0195$, $t = 2.615$, df = 15; males: $p < 0.0001$, $t = 9.172$, df = 6; females: $p = 0.8042$, $t = 0.2575$, df = 7) in the *Nacc1*$^{+/R284W}$ compared with that in *Nacc1*$^{+/+}$ mice. ***d***, ***e***, Electron microscopic images of motor cortex neuropil from 3-month-old *Nacc1*$^{+/+}$ and *Nacc1*$^{+/R284W}$ mice that are examples of those used for analysis of synaptic density. Arrows and arrowheads point to postsynaptic sites at spines and dendrites,

Table 9. Summary of behavioral and molecular phenotypes in *Nacc1*$^{+/R284W}$ mice: comparison of males and females

Phenotypes	Females	Males
Anxiety: Less time in center of open field	+	–
Memory		
Long term: Less time with novel object	–	–
Working: Alternation percentage	–	–
Clasping		
P14	–	–
4 months	+	+
6 months	+*	–*
Delayed weight gain		
P7, P14	+	–
P21	+	+
4 months	–	+
6 months	+*	+*
Grip strength deficit	–	–
Gait impairment	+	–
Nest building deficit	+	–
EEG—epileptiform discharges	+	+
EEG—δ power increased during SWS	–	+
NACC1 protein increase at P14, 3 months, 6 months, and 13 months	+	+
Changes in levels of synaptic proteins	+	+

*Tests done at UMass Chan.

and protein changes that implicate disturbances in multiple cellular pathways including those involved with synaptic functions. The phenotypes mimic those in patients and provide critically needed readouts to unravel disease mechanisms and test potential therapeutics.

Some deficits in *Nacc1*$^{+/R284W}$ mice were sex dependent and mostly in females (Table 9). The relevance of the sex disparity is unclear. Of note, of seven patients with *NACC1*$^{+/R298W}$ described, two were females (Schoch et al., 2017). This trend of fewer females has continued as more affected individuals have been identified (census reported to manuscript authors from Facebook parent group) and may indicate that females with the mutation are less viable and die in utero.

Both sexes of *Nacc1*$^{+/R284W}$ mice had behavioral seizures which were unpredictable and not captured during cortical EEG recordings in freely moving mice, similar to mice with a mutation in the methyl-CpG binding protein (MECP2) gene that causes Rett syndrome (Fallah and Eubanks, 2020). *NACC1*$^{+/R298W}$ patients typically exhibit seizures within the first year and present with myoclonic jerks and a disorganized EEG pattern containing intermittent large spikes called hypsarrhythmia [Schoch et al. (2017), their supplemental data and case reports].

Epileptiform discharges in EEG recording accompanied by momentary freezing observed in all *Nacc1*$^{+/R284W}$ mice resemble a human condition known as absence epilepsy (Crunelli and Leresche, 2002; Guerrini et al., 2019), a childhood disorder in which spike and slow wave discharges overlap with loss of awareness. Similar phenotypes have been observed in both neurodevelopmental and neurodegenerative disease models. One to 3 s bursts were observed in mice with the MECP2 gene mutation (Mandel-Brehm et al., 2015; Wither et al., 2018; review by Fallah and Eubanks, 2020). Interestingly, loss of EMG and spontaneous "epileptiform discharges" lasting 1–5 s were also seen in a mouse model of Alzheimer's disease (APdE9; Ziyatdinova et al., 2011). In both models, seizures were attenuated by treatment with the drug valproate, an FDA-approved drug to treat seizures, which has been proposed to enhance GABA transmission and stimulate GABA receptors and is an HDAC inhibitor (Gottlicher et al., 2001). Additionally, in the Rett mouse model, acetazolamide, an inhibitor of carbonic anhydrase, which raises CO_2 levels, significantly reduced the rate of bursting activity (Wither et al., 2018). In humans, absence epilepsy may involve disturbances in brain circuits forming cortico-thalamo-cortical loops, imbalance in glutamatergic excitatory and GABAergic inhibitory activities, and dysfunction of astrocytes and membrane channels (Villa and Combi, 2016; Gobbo et al., 2021). Epileptiform discharges, aka spike wave discharges, have been recorded in some inbred strains of wild-type mice but are not observed in wild-type C57BL/6J mice which was the strain used in our study (Letts et al., 2014).

P14 is a pivotal age in cortical development for maturation of synaptic connections (Semple et al., 2013; Gonzalez-Lozano et al., 2016). *Nacc1*$^{+/R284W}$ mice at this age had changes in transcripts encoding receptors such as AMPA2 and Gabarb3 and ion channels including T-type Ca^{2+} channel, which have been linked with epilepsy and seizures (listed in Fig. 12; Tables 5, 7) and likely contribute to the epileptiform discharges and behavioral seizures seen in older mice. Missense and null mutations in *Gria2*, which encodes the AMPA2 receptor, cause spontaneous seizures in mice (Brusa et al., 1995). Mutations in *Cacna1i* which encodes a T-type Ca^{2+} channel (Cav3.3) and *Gabrb3* which encodes a GABA receptor are associated with absence seizures in humans and animal models (Tanaka et al., 2008; Chen et al., 2014). Loss of function mutations in some transcripts also result in epilepsy phenotypes. For example, seizure disorder has been linked to mutations in Kcnj16 (Kohling and Wolfart, 2016). *Scn8a* which encodes the sodium channel SCN8A is increased in P14 *Nacc1*$^{+/R284W}$ mice. De novo gain of function mutation in the *Scn8A* gene causes seizure disorder, while other *Scn8A* mutations cause loss of function and result in intellectual disability (Blanchard et al., 2015). Kctd channels, one of which was increased in P14 *Nacc1*$^{R284W/R284W}$ mice (Table 7, Kctd5), also cause neurodevelopmental disorders (Teng et al., 2019). Other transcripts changed in *Nacc1*$^{+/R284W}$ mice, namely, *Syngap1* and *Kcnq3*, are known to cause epilepsy in mice from null mutations [review by Marshall et al. (2021), their Table 1]. Of note, mouse *Nacc1* interacts with Syngap1, a Ras Gap GTPase, and the presence of the R284W mutation in *Nacc1* reduced its interaction (Daniel et al., 2023). Seizures occur in some individuals with fragile X syndrome (FXS), a more common neurodevelopmental disorder resulting from a loss of function of the fragile X mental retardation protein (FMRP). In mouse models of FXS, there is altered activity at voltage-gated ion channels in layer 5 neurons of the prefrontal cortex including increased excitability through D-type K^+ channels (Kalmbach and Brager, 2020) and enhanced long-term depression in the hippocampus mediated through increased activation of metabotropic glutamate receptors (Huber et al., 2002).

←

respectively. Scale bar, 500 nm. ***f–h***, Number of synaptic contacts and total and average lengths of synapses in *Nacc1*$^{+/+}$ and *Nacc1*$^{+/R284W}$ mice. Box and whisker plots are results from Mann–Whitney *U* nonparametric test. The bar in the box represents the median and the whiskers represent the 5–95% percentile, ***f***, $p = 0.6738$, ***g***, $p = 0.2895$, ***h***, $p = 0.5931$, $n = 102$ images from 2 *Nacc1*$^{+/+}$ mice and $n = 101$ images from 2 *Nacc1*$^{+/R284W}$ mice.

The increase in NACC1 protein levels in mutant mice, especially in the short isoform which lacks the mutation, raises a question about the impact of this phenotype on neurodevelopment. Levels of NACC1 isoforms rise in rodent brain in response to the following: cocaine withdrawal, differentiation of neuroblastoma cells (N2a) with forskolin, and by activation at an intronic AP1 site by the immediate early genes c-*fos* and c-*jun* (Cha et al., 1997; Mackler et al., 2000, 2003; Korutla et al., 2002). It is conceivable that chronic epileptiform discharges in the cortex of *Nacc1*$^{+/R284W}$ mice drive aberrant neuronal activity to stimulate change in levels of *Nacc1* mRNA and protein. Both isoforms encode critical domains required for protein interactions, nuclear entry, and transcriptional repression, but the long isoform is a more potent transcriptional repressor in vitro than the short isoform (Korutla et al., 2002, 2005; Mackler et al., 2003). The preferential upturn in the short isoform seen in *Nacc1*$^{+/R284W}$ mice may compete to dampen transcriptional repression in response to stressful stimuli. Other splicing factors have self-regulating mechanisms. For example, SC35 mRNA in Hela cells reduces its levels by generating an alternative isoform that is a more unstable species (Sureau et al., 2001). It is worth emphasizing that unlike rodents, humans have one *NACC1* transcript in the brain and suffer more severe deficits from the heterozygous R298W mutation than the mice described here.

Patients with the *NACC1*$^{+/R298W}$ mutation have delayed to mild or moderate demyelination in the subcortical regions [Schoch et al. (2017), their supplementary case reports]. Consistent with these clinical findings, RNA-seq in *Nacc1*$^{+/R284W}$ mice revealed downregulation of *Gfap* and numerous other transcripts present in glia (Table 8), as well as fewer GFAP-labeled astrocytic processes in the corpus callosum (Fig. 10). Mice null for GFAP exhibit changes in myelin formation, blood–brain barrier dysfunction, and diminished astrocytic processes (Liedtke et al., 1996). In addition, primary cortical cells devoid of GFAP have impaired recycling of transporters that take up glutamate into astrocytes and neurons (Hughes et al., 2004). More extracellular glutamate from deficient astrocyte function in *Nacc1*$^{+/R284W}$ mice could drive abnormal epileptiform discharges seen during wakefulness and REM sleep. Thus, potential disturbances in glia in *Nacc1*$^{+/R284W}$ mice are likely to affect a multitude of functions involved with white matter development and neuronal activity.

In humans, most duplication/deletions of chromosome 19p13.13 which include *NACC1* (23 of 28, Deciphergenomics.org), or a loss of one *NACC1* allele with termination at amino acid 67, do not cause intellectual or motor disabilities or global developmental delay. Of the five de novo point mutations in *NACC1*, the heterozygous one at c892C>T (R298W) results in profound disability (Deciphergenomics.org). In contrast, mice with deletion of one *Nacc1* allele or complete knock-out display anatomical changes of in lumbar–sacral vertebrae (Yap et al., 2013; da Silva-Buttkus et al., 2023), which was not evident by x ray examination in an 8-year-old patient (reported to us by the parents of patient 1 described in Schoch et al., 2017). Our findings demonstrate that one mutant allele in *Nacc1*$^{+/R284W}$ mice is sufficient for a dominant active phenotype that mimics the human disorder, although two mutant alleles magnified some transcript and protein changes. Altogether, results show a gain of abnormal function by *NACC1* c892C>T (R298W). Selectively targeting and lowering the mutant allele should be tested in mice as a future therapy for patients.

References

Ammanuel S, Chan WC, Adler DA, Lakshamanan BM, Gupta SS, Ewen JB, Johnston MV, Marcus CL, Naidu S, Kadam SD (2015) Heightened delta power during slow-wave-sleep in patients with Rett syndrome associated with poor sleep efficiency. PLoS One 10:e0138113.

Anaclet C, Ferrari L, Arrigoni E, Bass CE, Saper CB, Lu J, Fuller PM (2014) The GABAergic parafacial zone is a medullary slow wave sleep-promoting center. Nat Neurosci 17:1217–1224.

Anaclet C, Pedersen NP, Ferrari LL, Venner A, Bass CE, Arrigoni E, Fuller PM (2015) Basal forebrain control of wakefulness and cortical rhythms. Nat Commun 6:8744.

Blanchard MG, et al. (2015) De novo gain-of-function and loss-of-function mutations of SCN8A in patients with intellectual disabilities and epilepsy. J Med Genet 52:330–337.

Boddaert J, et al. (2007) Evidence of a role for lactadherin in Alzheimer's disease. Am J Pathol 170:921–929.

Brusa R, Zimmermann F, Koh DS, Feldmeyer D, Gass P, Seeburg PH, Sprengel R (1995) Early-onset epilepsy and postnatal lethality associated with an editing-deficient GluR-B allele in mice. Science 270: 1677–1680.

Buzsaki G (2002) Theta oscillations in the hippocampus. Neuron 33:325–340.

Cha XY, Pierce RC, Kalivas PW, Mackler SA (1997) NAC-1, a rat brain mRNA, is increased in the nucleus accumbens three weeks after chronic cocaine self-administration. J Neurosci 17:6864–6871.

Chen Y, Parker WD, Wang K (2014) The role of T-type calcium channel genes in absence seizures. Front Neurol 5:45.

Crunelli V, Leresche N (2002) Childhood absence epilepsy: genes, channels, neurons and networks. Nat Rev Neurosci 3:371–382.

Cruz E, Descalzi G, Steinmetz A, Scharfman HE, Katzman A, Alberini CM (2021) CIM6P/IGF-2 receptor ligands reverse deficits in Angelman syndrome model mice. Autism Res 14:29–45.

Daniel JA, Elizarova S, Shaib AH, Chouaib AA, Magnussen HM, Wang J, Brose N, Rhee J, Tirard M (2023) An intellectual-disability-associated mutation of the transcriptional regulator NACC1 impairs glutamatergic neurotransmission. Front Mol Neurosci 16:1115880.

Da Silva-Buttkus P, et al. (2023) Knockout mouse models as a resource for the study of rare diseases. Mamm Genome 34:244–261.

Dorninger F, Zeitler G, Berger J (2020) Nestlet shredding and nest building tests to assess features of psychiatric disorders in mice. Bio Protoc 10: e3863.

Fallah MS, Eubanks JH (2020) Seizures in mouse models of rare neurodevelopmental disorders. Neuroscience 445:50–68.

Farhy-Tselnicker I, Allen NJ (2018) Astrocytes, neurons, synapses: a tripartite view on cortical circuit development. Neural Dev 13:7.

Farhy-Tselnicker I, Boisvert MM, Liu H, Dowling C, Erikson GA, Blanco-Suarez E, Farhy C, Shokhirev MN, Ecker JR, Allen NJ (2021) Activity-dependent modulation of synapse-regulating genes in astrocytes. Elife 10:e70514.

Fernagut PO, Diguet E, Labattu B, Tison F (2002) A simple method to measure stride length as an index of nigrostriatal dysfunction in mice. J Neurosci Methods 113:123–130.

Girirajan S, Patel N, Slager RE, Tokarz ME, Bucan M, Wiley JL, Elsea SH (2008) How much is too much? Phenotypic consequences of Rai1 overexpression in mice. Eur J Hum Genet 16:941–954.

Gobbo D, Scheller A, Kirchhoff F (2021) From physiology to pathology of cortico-thalamo-cortical oscillations: astroglia as a target for further research. Front Neurol 12:661408.

Gonzalez-Lozano MA, Klemmer P, Gebuis T, Hassan C, Van Nierop P, Van Kesteren RE, Smit AB, Li KW (2016) Dynamics of the mouse brain cortical synaptic proteome during postnatal brain development. Sci Rep 6: 35456.

Gonzalez-Rey E, Varela N, Sheibanie AF, Chorny A, Ganea D, Delgado M (2006) Cortistatin, an antiinflammatory peptide with therapeutic action in inflammatory bowel disease. Proc Natl Acad Sci U S A 103:4228–4233.

Gottlicher M, et al. (2001) Valproic acid defines a novel class of HDAC inhibitors inducing differentiation of transformed cells. EMBO J 20:6969–6978.

Guerrini R, Marini C, Barba C (2019) Generalized epilepsies. Handb Clin Neurol 161:3–15.

Hall LL, Smith KP, Byron M, Lawrence JB (2006) Molecular anatomy of a speckle. Anat Rec A Discov Mol Cell Evol Biol 288:664–675.

He Q, Gao Y, Wang T, Zhou L, Zhou W, Yuan Z (2019) Deficiency of yes-associated protein induces cataract in mice. Aging Dis 10:293–306.

Hirsch-Reinshagen V, et al. (2009) LCAT synthesized by primary astrocytes esterifies cholesterol on glia-derived lipoproteins. J Lipid Res 50:885–893.
Hu H, Vervaeke K, Storm JF (2007) M-channels (Kv7/KCNQ channels) that regulate synaptic integration, excitability, and spike pattern of CA1 pyramidal cells are located in the perisomatic region. J Neurosci 27:1853–1867.
Huber KM, Gallagher SM, Warren ST, Bear MF (2002) Altered synaptic plasticity in a mouse model of fragile X mental retardation. Proc Natl Acad Sci U S A 99:7746–7750.
Hughes EG, Maguire JL, Mcminn MT, Scholz RE, Sutherland ML (2004) Loss of glial fibrillary acidic protein results in decreased glutamate transport and inhibition of PKA-induced EAAT2 cell surface trafficking. Brain Res Mol Brain Res 124:114–123.
Jin N, Lipponen A, Koivisto H, Gurevicius K, Tanila H (2018) Increased cortical beta power and spike-wave discharges in middle-aged APP/PS1 mice. Neurobiol Aging 71:127–141.
Kalivas PW, Duffy P, Mackler SA (1999) Interrupted expression of NAC-1 augments the behavioral responses to cocaine. Synapse 33:153–159.
Kalmbach BE, Brager DH (2020) Fragile X mental retardation protein modulates somatic D-type K(+) channels and action potential threshold in the mouse prefrontal cortex. J Neurophysiol 124:1766–1773.
Ke Y, et al. (2020) Trappc9 deficiency in mice impairs learning and memory by causing imbalance of dopamine D1 and D2 neurons. Sci Adv 6: eabb7781.
Kegel KB, et al. (2002) Huntingtin is present in the nucleus, interacts with the transcriptional corepressor C-terminal binding protein, and represses transcription. J Biol Chem 277:7466–7476.
Kohling R, Wolfart J (2016) Potassium channels in epilepsy. Cold Spring Harb Perspect Med 6:a022871.
Korutla L, Wang P, Jackson TG, Mackler SA (2009) NAC1, a POZ/BTB protein that functions as a corepressor. Neurochem Int 54:245–252.
Korutla L, Wang PJ, Lewis DM, Neustadter JH, Stromberg MF, Mackler SA (2002) Differences in expression, actions and cocaine regulation of two isoforms for the brain transcriptional regulator NAC1. Neuroscience 110:421–429.
Korutla L, Wang PJ, Mackler SA (2005) The POZ/BTB protein NAC1 interacts with two different histone deacetylases in neuronal-like cultures. J Neurochem 94:786–793.
Kraeuter AK, Guest PC, Sarnyai Z (2019) The Y-maze for assessment of spatial working and reference memory in mice. Methods Mol Biol 1916:105–111.
Lalonde R, Strazielle C (2011) Brain regions and genes affecting limb-clasping responses. Brain Res Rev 67:252–259.
Letts VA, Beyer BJ, Frankel WN (2014) Hidden in plain sight: spike-wave discharges in mouse inbred strains. Genes Brain Behav 13:519–526.
Liedtke W, Edelmann W, Bieri PL, Chiu FC, Cowan NJ, Kucherlapati R, Raine CS (1996) GFAP is necessary for the integrity of CNS white matter architecture and long-term maintenance of myelination. Neuron 17:607–615.
Liu ET, Bolcun-Filas E, Grass DS, Lutz C, Murray S, Shultz L, Rosenthal N (2017) Of mice and CRISPR: the post-CRISPR future of the mouse as a model system for the human condition. EMBO Rep 18:187–193.
Livak KJ, Schmittgen TD (2001) Analysis of relative gene expression data using real-time quantitative PCR and the 2(-delta delta C(T)) method. Methods 25:402–408.
Lueptow LM (2017) Novel object recognition test for the investigation of learning and memory in mice. J Vis Exp 126:e55718.
Lyu B, Dong Y, Kang J (2021) A new case of de novo variant c.892C>T (p.Arg298Trp) in NACC1: a first case report from China. Front Pediatr 9:754261.
Mackler SA, Homan YX, Korutla L, Conti AC, Blendy JA (2003) The mouse nac1 gene, encoding a cocaine-regulated bric-a-brac tramtrac broad complex/Pox virus and zinc finger protein, is regulated by AP1. Neuroscience 121:355–361.
Mackler SA, Korutla L, Cha XY, Koebbe MJ, Fournier KM, Bowers MS, Kalivas PW (2000) NAC-1 is a brain POZ/BTB protein that can prevent cocaine-induced sensitization in the rat. J Neurosci 20:6210–6217.
Malkani RG, Zee PC (2022) Brain stimulation for improving sleep and memory. Sleep Med Clin 17:505–521.
Mandel-Brehm C, Salogiannis J, Dhamne SC, Rotenberg A, Greenberg ME (2015) Seizure-like activity in a juvenile Angelman syndrome mouse model is attenuated by reducing Arc expression. Proc Natl Acad Sci U S A 112:5129–5134.
Marshall GF, Gonzalez-Sulser A, Abbott CM (2021) Modelling epilepsy in the mouse: challenges and solutions. Dis Model Mech 14:dmm047449.
Miano JM, Zhu QM, Lowenstein CJ (2016) A CRISPR path to engineering new genetic mouse models for cardiovascular research. Arterioscler Thromb Vasc Biol 36:1058–1075.
Nakayama N, et al. (2020) Nucleus accumbens-associated protein 1 binds DNA directly through the BEN domain in a sequence-specific manner. Biomedicines 8:608.
Ostrowski LM, Spencer ER, Bird LM, Thibert R, Komorowski RW, Kramer MA, Chu CJ (2021) Delta power robustly predicts cognitive function in Angelman syndrome. Ann Clin Transl Neurol 8:1433–1445.
Ratner C, et al. (2016) Effects of peripheral neurotensin on appetite regulation and its role in gastric bypass surgery. Endocrinology 157:3482–3492.
Reim D, Weis TM, Halbedl S, Delling JP, Grabrucker AM, Boeckers TM, Schmeisser MJ (2016) The Shank3 interaction partner ProSAPiP1 regulates postsynaptic SPAR levels and the maturation of dendritic spines in hippocampal neurons. Front Synaptic Neurosci 8:13.
Rexach J, Lee H, Martinez-Agosto JA, Nemeth AH, Fogel BL (2019) Clinical application of next-generation sequencing to the practice of neurology. Lancet Neurol 18:492–503.
Roche KJ, Leblanc JJ, Levin AR, O'leary HM, Baczewski LM, Nelson CA (2019) Electroencephalographic spectral power as a marker of cortical function and disease severity in girls with Rett syndrome. J Neurodev Disord 11:15.
Ruan Y, et al. (2017) Nac1 promotes self-renewal of embryonic stem cells through direct transcriptional regulation of c-Myc. Oncotarget 8:47607–47618.
Sapp E, Seeley C, Iuliano M, Weisman E, Vodicka P, Difiglia M, Kegel-Gleason KB (2020) Protein changes in synaptosomes of Huntington's disease knock-in mice are dependent on age and brain region. Neurobiol Dis 141:104950.
Schoch K, et al. (2017) A recurrent de novo variant in NACC1 causes a syndrome characterized by infantile epilepsy, cataracts, and profound developmental delay. Am J Hum Genet 100:343–351.
Schoch K, Mcconkie-Rosell A, Walley N, Bhambhani V, Feyma T, Undiagnosed Diseases N, Pizoli CE, Smith EC, Tan QK, Shashi V (2023) Parental perspectives of episodic irritability in an ultra-rare genetic disorder associated with NACC1. Orphanet J Rare Dis 18:269.
Scofield MD, Korutla L, Jackson TG, Kalivas PW, Mackler SA (2012) Nucleus accumbens 1, a pox virus and zinc finger/bric-a-brac tramtrack broad protein binds to TAR DNA-binding protein 43 and has a potential role in amyotrophic lateral sclerosis. Neuroscience 227:44–54.
Seibenhener ML, Wooten MC (2015) Use of the open field maze to measure locomotor and anxiety-like behavior in mice. J Vis Exp 96:e52434.
Semple BD, Blomgren K, Gimlin K, Ferriero DM, Noble-Haeusslein LJ (2013) Brain development in rodents and humans: identifying benchmarks of maturation and vulnerability to injury across species. Prog Neurobiol 106–107:1–16.
Shen H, Korutla L, Champtiaux N, Toda S, Lalumiere R, Vallone J, Klugmann M, Blendy JA, Mackler SA, Kalivas PW (2007) NAC1 regulates the recruitment of the proteasome complex into dendritic spines. J Neurosci 27:8903–8913.
Sidorov MS, Deck GM, Dolatshahi M, Thibert RL, Bird LM, Chu CJ, Philpot BD (2017) Delta rhythmicity is a reliable EEG biomarker in Angelman syndrome: a parallel mouse and human analysis. J Neurodev Disord 9:17.
Simon P, Dupuis R, Costentin J (1994) Thigmotaxis as an index of anxiety in mice. Influence of dopaminergic transmissions. Behav Brain Res 61:59–64.
Steinhoff MS, Von Mentzer B, Geppetti P, Pothoulakis C, Bunnett NW (2014) Tachykinins and their receptors: contributions to physiological control and the mechanisms of disease. Physiol Rev 94:265–301.
Sureau A, Gattoni R, Dooghe Y, Stevenin J, Soret J (2001) SC35 autoregulates its expression by promoting splicing events that destabilize its mRNAs. EMBO J 20:1785–1796.
Taglialatela G, Hogan D, Zhang WR, Dineley KT (2009) Intermediate- and long-term recognition memory deficits in Tg2576 mice are reversed with acute calcineurin inhibition. Behav Brain Res 200:95–99.
Tanaka M, et al. (2008) Hyperglycosylation and reduced GABA currents of mutated GABRB3 polypeptide in remitting childhood absence epilepsy. Am J Hum Genet 82:1249–1261.
Tatemichi Y, Shibazaki M, Yasuhira S, Kasai S, Tada H, Oikawa H, Suzuki Y, Takikawa Y, Masuda T, Maesawa C (2015) Nucleus accumbens associated 1 is recruited within the promyelocytic leukemia nuclear body through SUMO modification. Cancer Sci 106:848–856.
Teng X, Aouacheria A, Lionnard L, Metz KA, Soane L, Kamiya A, Hardwick JM (2019) KCTD: a new gene family involved in neurodevelopmental and neuropsychiatric disorders. CNS Neurosci Ther 25:887–902.

Vaddadi N, Iversen K, Raja R, Phen A, Brignall A, Dumontier E, Cloutier JF (2019) Kirrel2 is differentially required in populations of olfactory sensory neurons for the targeting of axons in the olfactory bulb. Development 146: dev173310.

Valencia A, et al. (2013) Striatal synaptosomes from Hdh140Q/140Q knock-in mice have altered protein levels, novel sites of methionine oxidation, and excess glutamate release after stimulation. J Huntingtons Dis 2:459–475.

Van Erum J, Van Dam D, De Deyn PP (2019) PTZ-induced seizures in mice require a revised Racine scale. Epilepsy Behav 95:51–55.

Villa C, Combi R (2016) Potassium channels and human epileptic phenotypes: an updated overview. Front Cell Neurosci 10:81.

Wendholt D, et al. (2006) ProSAP-interacting protein 1 (ProSAPiP1), a novel protein of the postsynaptic density that links the spine-associated Rap-Gap (SPAR) to the scaffolding protein ProSAP2/Shank3. J Biol Chem 281:13805–13816.

Wertman V, Gromova A, La Spada AR, Cortes CJ (2019) Low-cost gait analysis for behavioral phenotyping of mouse models of neuromuscular disease. J Vis Exp 149:e59878.

Wither RG, Colic S, Bardakjian BL, Snead OC 3rd, Zhang L, Eubanks JH (2018) Electrographic and pharmacological characterization of a progressive epilepsy phenotype in female MeCP2-deficient mice. Epilepsy Res 140:177–183.

Yap KL, et al. (2013) Loss of NAC1 expression is associated with defective bony patterning in the murine vertebral axis. PLoS One 8:e69099.

Yap KL, Fraley SI, Thiaville MM, Jinawath N, Nakayama K, Wang J, Wang TL, Wirtz D, Shih Ie M (2012) NAC1 is an actin-binding protein that is essential for effective cytokinesis in cancer cells. Cancer Res 72:4085–4096.

Yau WM (1978) Effect of substance P on intestinal muscle. Gastroenterology 74:228–231.

Zheng L, et al. (2022) Distinct structural bases for sequence-specific DNA binding by mammalian BEN domain proteins. Genes Dev 36: 225–240.

Ziyatdinova S, Gurevicius K, Kutchiashvili N, Bolkvadze T, Nissinen J, Tanila H, Pitkanen A (2011) Spontaneous epileptiform discharges in a mouse model of Alzheimer's disease are suppressed by antiepileptic drugs that block sodium channels. Epilepsy Res 94:75–85.